High Speed Linear Induction Motor Efficiency Optimization

by

Andrew P. Johnson

B.S. Electrical Engineering
SUNY Buffalo, 1994

Submitted to the Department of Ocean Engineering and the Department of Electrical Engineering and Computer Science in Partial Fulfillment of the Requirements for the Degree of

Naval Engineer

and

Master of Science in Electrical Engineering and Computer Science

at the
Massachusetts Institute of Technology
June 2005

Signature of Author.....
Department of Ocean Engineering
May 7, 2005

Certified by.....
James L. Kirtley, Jr.
Professor of Electrical Engineering
Thesis Supervisor

Certified by.....
Timothy J. McCoy
Associate Professor of Naval Construction and Engineering
Thesis Reader

Accepted by.....
Michael S. Triantafyllou
Chairman, Committee on Graduate Students
Department of Ocean Engineering

Accepted by.....
Arthur C. Smith
Chairman, Committee on Graduate Students
Department of Electrical Engineering and Computer Science

High Speed Linear Induction Motor Efficiency Optimization

by

Andrew P. Johnson

Submitted to the Department of Ocean Engineering and
the Department of Electrical Engineering and Computer Science
on May 4, 2005 in Partial Fulfillment of
the Requirements for the Degrees of Naval Engineer and
Master of Science in Electrical
Engineering and Computer Science

ABSTRACT

One of the reasons linear motors, a technology nearly a century old, have not been adopted for a large number of linear motion applications is that they have historically had poor efficiencies. This has restricted the progress of linear motor development. The concept of a linear motor as a rotary motor cut and laid out flat with a conventional rotary motor control scheme as a design basis may not be the best way to design and control a high-speed linear motor. End effects and other geometry subtleties of a linear motor make it unique, and a means of optimizing efficiency with both the motor geometry and the motor control scheme will be analyzed to create a High-Speed Linear Induction Motor (LIM) with a higher efficiency than what is possible with conventional motors and controls.

This thesis pursues the modeling of a short secondary type Double-Sided Linear Induction Motor (DSLIM) that is proposed for use as an Electromagnetic Aircraft Launch System (EMALS) aboard the CVN-21. Mathematical models for the prediction of effects that are peculiar to DSLIM are formulated, and their overall effects on the performance of the proposed machine are analyzed. These effects are used to generate a transient motor model, which is then driven by a motor controller that is specifically designed to the characteristics of the proposed DSLIM.

Due to this DSLIM's role as a linear accelerator, the overall efficiency of the DSLIM will be judged by the kinetic energy of the launched projectile versus the total electric energy that the machine consumes. This thesis is meant to propose a maximum possible efficiency for a DSLIM in this type of role.

Thesis Supervisor: James L. Kirtley Jr.
Title: Professor of Electrical Engineering

THIS PAGE INTENTIONALLY BLANK

Acknowledgements

The author would like to thank the following individuals for their assistance. Without them, this work would not have been possible.

- Professor James Kirtley, whose help and patience with me regarding linear motors is greatly appreciated.
- CDR Timothy McCoy for his insights into Naval power systems and for being a great thesis reader.
- LCDR Jon Rucker for his excellent research on high-power semiconductors.
- My wife and children (Jen, Elizabeth, and Samantha) for their understanding of the time commitment that I have made to this work.

THIS PAGE INTENTIONALLY BLANK

Contents

List of Figures

List of Tables

THIS PAGE INTENTIONALLY BLANK

Chapter 1

1.0 Introduction

1.1 Motivation for Research

The U.S. Navy has relied on steam-driven catapult systems to launch aircraft from aircraft carriers for 50 years [1]. The first steam catapults used to launch aircraft from a ship were developed by the British, with the first installation going on the HMS Perseus (Figure 1). This system was subsequently tested by the US Navy to launch US Naval

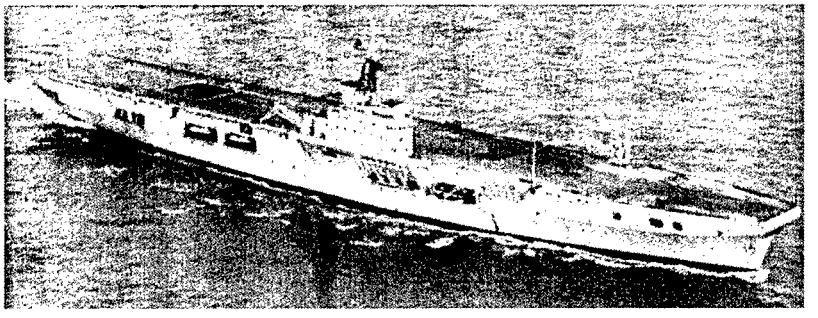

Figure 1 HMS Perseus, First Steam Catapult Aircraft Carrier

aircraft, and the design was approved for installation in the USS Hancock, making the USS Hancock the first steam catapult equipped aircraft carrier (Figure 2). These catapult

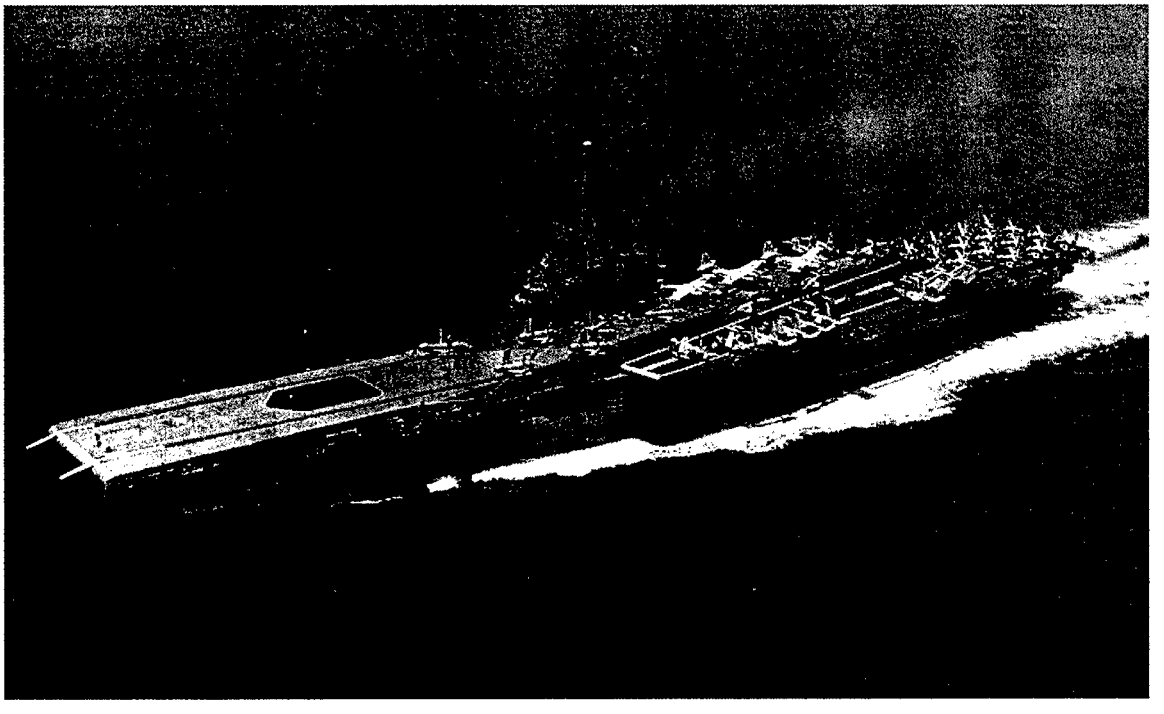

Figure 2 USS Hancock, First US Navy Steam Catapult Aircraft Carrier

systems have changed little since their introduction by the Royal Navy in the 1950s, with the only real innovations being in the method of controlling the steam pressure to the piston. With the next generation aircraft carrier, CVN-21, the catapult system will no

longer be steam operated but rather electromagnetically operated. This Electromagnetic Aircraft Launch System (EMALS) will utilize a linear motor to effect aircraft launches. The research presented in this thesis is meant to guide the design of future EMALS by proposing a means of optimizing a linear motor design for the purpose of launching aircraft.

1.1.1 Current U.S. Navy Aircraft Launch Systems

The basic catapult system of the U.S. Navy today uses steam-driven pistons located in the flight deck, which connect to a shuttle that in turn is connected to the aircraft. Prior to launch, flight deck personnel are instructed by aircraft flightcrew as to the approximate weight of the aircraft for a particular launch, and that information, coupled with the airframe type and Wind Over Deck (WOD) are input to the catapult system computer. This catapult system computer in turn sets the required pressure for the steam regulator to maintain to effect a launch. There is no feedback in the system to determine aircraft position or velocity, and the launch is a very violent process because of the non-constant jerk rate of the catapult [2].

Airframes subjected to catapult launches are inherently shorter-lived than those airframes that fly from conventional airfields because of the steam catapult's uneven acceleration. A comparison of airframe stresses between the U.S. Navy's premier tactical aircraft, the F -14 Tomcat, and the U.S. Air Force's premier tactical aircraft, the F-15 Eagle, shows that the F-14's catapult drag brace must be capable of withstanding 414,000 pounds of force while taking off in a distance of 245 feet. The F-15 has no drag brace, and has a required runway length of 2000 feet to take off at maximum gross weight. Not surprisingly, the F-15 has a longer airframe lifetime than the F-14 due to the fact that it always operates from conventional airfields [2], [3], [4], [5]. It is true that a lot of the airframe stress on F-14s comes from arrested landings, but a good deal of the stress is attributable to the catapult launch.

1.1.2 Electromagnetic Aircraft Launch Systems

Electromagnetic Aircraft Launch Systems (EMALS) use linear motors to accelerate aircraft to launch speed. Linear motors are, in simple terms, conventional rotating motors that are cut and laid out flat. Linear motors come in a variety of types, including Linear Induction Motors (LIM) and Linear Permanent Magnet Motors (LPMM), and each has its own advantages. LIM and LPMM are the types that are frequently considered for use in EMALS because they require no sliding contacts, and

hence these types of linear motors are better from a reliability and maintainability standpoint.

One advantage that EMALS has over traditional steam catapult systems is its ability to control the acceleration of an aircraft through feedback. With a dynamic energy storage system such as a flywheel, robust variable frequency drive power electronics, and a position sensing system installed along the motor track, a control system with feedback could easily be used to maintain an even acceleration. This would have the benefit of reduced airframe and aircrew stresses and could increase airframe lifetime by 31% [2].

Another advantage of EMALS is the fact that it is not a highly maintenance intensive system. Steam catapults frequently break due to steam regulator valve problems, catapult trough fires, steam accumulator problems, and a number of other problematic areas. The primary (field-producing) component of EMALS, in normal operation, will never touch the shuttle (reaction-field-producing) component, and thus there will be much less mechanical wear in the system. Mechanical wear will only be as a result of bearing wear from the track that the shuttle rides in. Because there will be much less mechanical wear under these circumstances, the linear motor will require much less preventive maintenance and should not have the mechanical problems that plague conventional steam catapult systems [2], [3].

The final advantage that EMALS has over conventional steam catapults is the possibility for larger loads. The current steam catapult system, C-13-2, is at the limit of its capability for launching the aircraft of a typical U.S. Navy Airwing [2], [3], [4]. EMALS will give the U.S. Navy a boost in capability to launch larger aircraft from aircraft carriers, and as linear motor power densities improve in the future, this capability will improve as well.

1.2 Linear Motors

Linear motors have been around for nearly a century, and yet are still in their early stages of development. Because of their large airgaps, low efficiencies and low power factor they have not been considered viable design options for many high-speed linear motion applications [6]. Recently, linear motors have been getting a second look by a variety of users that require a traction force by means of something other than friction. High speed trains and monorails as well as EMALS are just a few of the recent designs using linear motors [7].

In high-speed applications, there is no easy way to reduce the airgap size of a linear motor. The speed of motion between the primary and the secondary means that the airgap cannot be made too small because of the likelihood they will come into contact. At the advertised speeds of some high-speed linear motors (>200 m/s), this could cause significant wear and even damage of the motor. If this airgap is large compared to the pole pitch of the motor, a significant amount of flux will bypass the secondary of the motor entirely, thus creating flux leakage and generating no useful power. Aircraft carriers are subject to the additional issues of thermal expansion and torsion in the deck from sea-induced loading, which requires that the airgap be sized to allow for these issues and still permit safe operation of the motor.

As a result of the relatively large airgap of the linear motor, and various other linear motor specific problems such as end effect and transverse edge effects, the efficiency of the linear motor is not as good as a conventional rotary motor. As an example, conventional rotary induction motors are capable of efficiencies greater than 90% [8], while high-speed linear induction motors only have efficiencies around 50% [9]. In addition to the flux linkage lost due to the air gap leakage flux, the flux within the airgap is also distorted and reduced by the end effect due to the finite length of the secondary of the linear motor. These effects combine to produce a poor power factor and a correspondingly low efficiency.

1.2.1 The Double-Sided Linear Induction Motor (DSLIM)

The DSLIM is a LIM with a primary on both sides of a conducting secondary. A DSLIM is illustrated below in both Figure 3 and Figure 4. DSLIM are the usual choice for high-speed linear motor applications where no levitation is required.

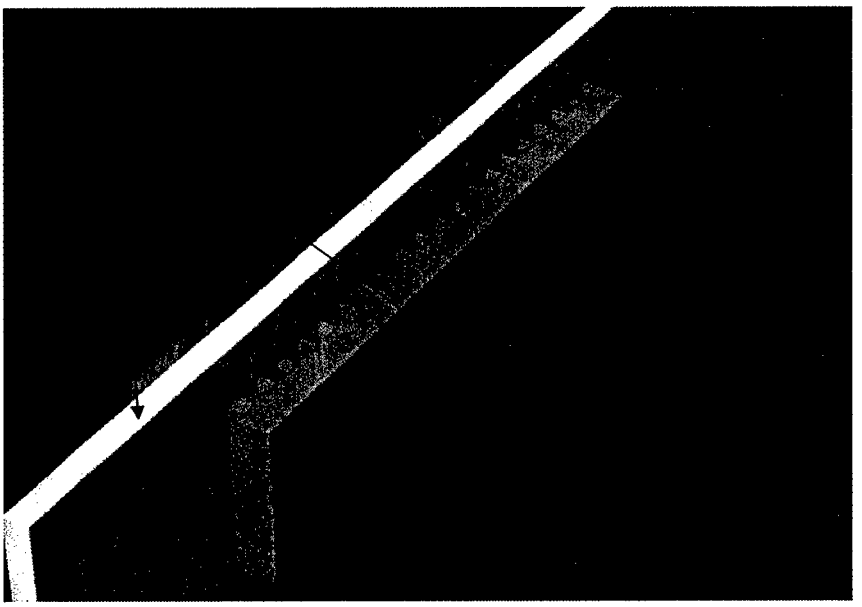

Figure 3 Short Primary Double Sided Linear Induction Motor

The DSLIM pictured in Figure 3 is known as a short primary DSLIM because the secondary extends beyond the active (field-producing) portion of the primary. The DSLIM pictured in Figure 4 is known as a short secondary DSLIM because the primary extends beyond the secondary.

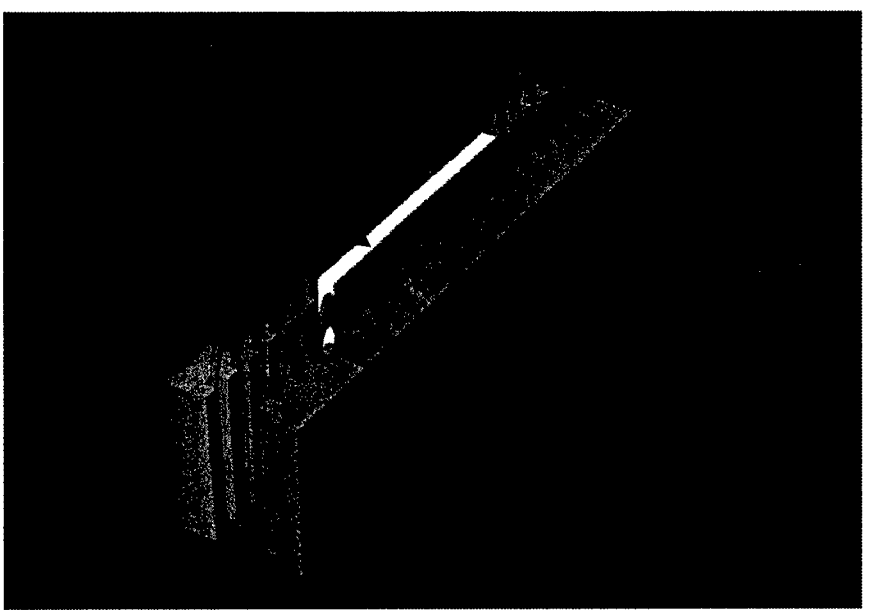

Figure 4 Short Secondary Double Sided Linear Induction Motor

The pictured DSLIMs can be thought of as rotary induction motors cut at two places 180 degrees apart and then laid flat. DSLIM are usually used for high-speed linear motor applications because of the benefit of having the field produced on both sides of the secondary, thus linking more flux and balancing the transverse forces that would be

present in a SLIM. In an application such as EMALS, there is no need for such a transverse force, and therefore a DSLIM is the obvious choice.

In the course of this discussion, the stator will refer to the field-producing (non-moving) portion of the motor. The terms rotor and shuttle will be used interchangeably, and will refer to the moving part of the motor to which the aircraft is attached. This is because the two types of motor can be viewed in the same reference frame by simply converting pole pitch from an angle to a distance, and vice-versa.

1.3 EMALS and DSLIM: The Design Challenge

DSLIM of the design of Figure 3 are advertised to be capable of speeds in excess of 200 meters per second. This makes them ideally suited for EMALS applications. However, DSLIM, and linear motors in general, are inherently inefficient because of their aforementioned qualities. In a terrestrial environment in which power is relatively easy to draw from the grid, efficiency may not be a major issue. But on a warship such as an aircraft carrier, in which there is a finite generating capacity, efficiency can be a huge issue and impact the total number of launches per minute as well as the number of energy storage devices that must be used. These energy storage devices, when combined with the weight of the motor itself, can also produce a heavier system, which could cause ship stability problems. Past linear motor designs have not delved into the issue of increasing the efficiency of a LIM by looking at the entire system, but rather have looked at single components [9], [10], [11]. Clearly, the DSLIM should be looked at as a total system consisting of a motor controller and the motor itself. Some of the particular design challenges of a DSLIM include:

- End effects
- Transverse edge effects
- Spatial harmonics of the magnetic field
- Time harmonics of the supply current
- Phase unbalances within the primary coils

1.4 Objectives and Outline of Thesis

The research and design effort of this thesis was to produce a method of synthesizing a DSLIM in such a way as to optimize its overall efficiency and power factor. Chapter 2 outlines the various phenomenon that DSLIM experience which contribute to their loss of efficiency, and shows how these phenomenon are modeled. Chapter 3 discusses the modeling of the structure of the DSLIM, and what parameters are

varied to control the phenomena that cause inefficiency of the DSLIM. Chapter 4 discusses the modeling of various control schemes for a DSLIM and shows how they are implemented on a DSLIM. Chapter 5 synthesizes a design for a complete DSLIM aircraft launch system, and chapter 6 models the DSLIM and control scheme chosen in chapters 4 and 5 respectively to analyze the system's efficiency as an aircraft launch system. Finally, chapter 7 presents conclusions and recommendations for future work.

THIS PAGE INTENTIONALLY BLANK

Chapter 2

2.0 Background

2.1 Linear Induction Motor Peculiarities

2.1.1 End Effects

End effects are described as one of the biggest negative factors in high-speed LIM efficiency [6]. The fact that the LIM has an entry and an exit end, as opposed to a closed airgap common to a rotary induction motor, is the reason that LIM have this phenomenon. This causes discontinuities in the magnetic field producing part of the LIM or the conducting part of the LIM when using a short primary or short secondary LIM respectively. Laithwaite proposed the use of a short primary DSLIM for aircraft launch operations due to the costs associated with producing a primary for a short secondary DSLIM long enough to launch an aircraft. This logic would seem to be backed up by the fact that Westinghouse developed the 'Electropult' using a short primary SLIM with a wound secondary in the track to enable changes in the resistance of the secondary conducting sheet. Figure 5 shows the Electropult with an aircraft being readied for launch. Figure 6 shows a close up of the primary and secondary components.

Figure 5 Electropult with Aircraft Readying for Launch (1945) [9]

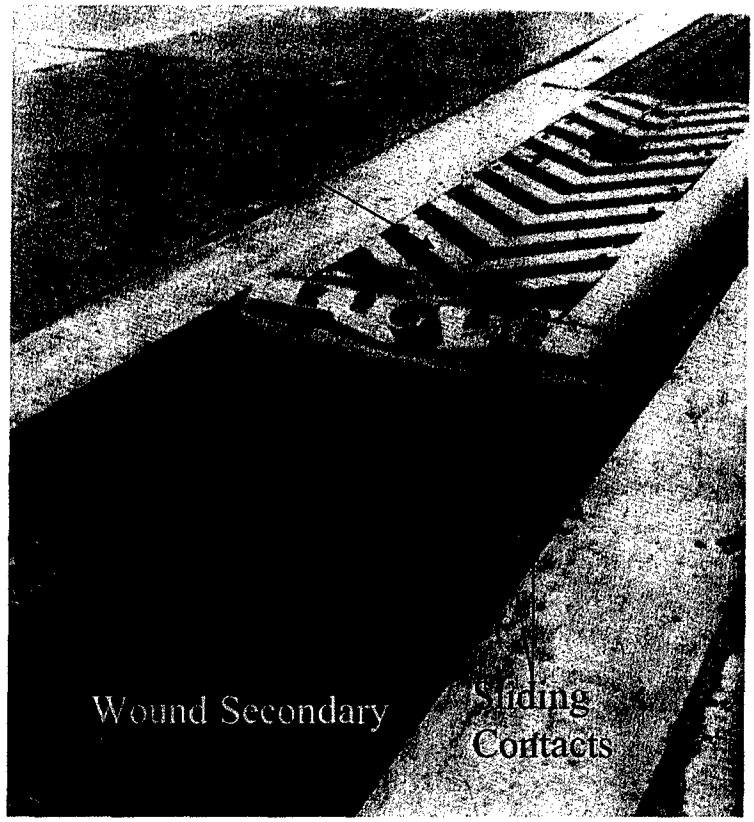

Figure 6 'Electropult' Close-Up [9]

The 'Electropult' showed that launching an aircraft using a linear motor was possible, but the machine was not very efficient, and ultimately it was cost that caused the abandonment of the idea. Having a wound secondary to control thrust made the machine controllable, but it negated the cost savings of only having the motor on a short piece of primary. For the purposes of a shipboard aircraft launch system, Kirtley [12] advocates a short secondary DSLIM because of its reduced end effects along with the associated problems of running sliding contacts to the moving primary on a flight deck that is routinely wet and greasy. The reasoning here is very logical in that the rewards reaped in efficiency and reliability outweigh the costs associated with a track that is going to be of a finite length to begin with. A lower efficiency on board a ship would mean that a larger generation and energy storage system would be required (assuming the same number of catapult shots per unit time would be required), thus driving up costs, weight, and taking up additional space on board. The DSLIM length for EMALS will be approximately 90m [13], while the Electropult ran for over 200 meters [9]. There is no question that as the motor length increases, the cost of a short secondary DSLIM goes up rapidly, but

with a motor that is a mere 90 meters long, the short secondary DSLIM is best suited for shipboard applications.

The end effects in a short secondary DSLIM are quite different from those experienced in a short primary DSLIM. Most research to date on the end effect has been with regard to the short primary DSLIM and its effect on rapid transit trains with respect to efficiency [6], [14]. As the primary field of the short primary DSLIM sweeps forward at some speed, it successively covers and uncovers sections of the secondary conducting sheet. Each successive section of the conducting sheet that is covered has to attain a magnetic equilibrium with the applied field. The secondary conducting sheet does this by generating its own currents in order to satisfy Ampere's Law. Since the conducting sheet has some finite resistivity and reluctance to the applied magnetic field, it takes some time for the aforementioned magnetic equilibrium to take place. Thus, in a short primary DSLIM, the field is travelling forward at the same speed as the vehicle, which in some high-speed transit applications is on the order of 200 miles per hour. At these high speeds, the magnetic field at the entry end of the primary shuttle is seriously degraded, and this degradation propagates backward into the primary shuttle as speed increases. If the primary is not long enough, the end effect can propagate through the entire primary shuttle, reducing the capacity for the vehicle to produce effective thrust.

In a short secondary DSLIM, the shuttle is now merely a conducting sheet of Aluminum or Copper, and the stationary primary produces a magnetic field that sweeps forward over the shuttle at a speed that is the difference between the speed of the applied field and the speed of the shuttle. This speed difference is known as the slip speed. Since it is desirable to operate any induction motor at low slip, it can be assumed that the slip speed of the short secondary DSLIM will be small compared to the actual shuttle speed at any point in time. Thus the short secondary DSLIM will have an end effect, but with proper selection of the secondary and proper attention to the slip that the machine is operating at, the end effect will have a much smaller effect than that in the short primary DSLIM.

2.1.2 Transverse Edge Effects

Transverse edge effects are the result of eddy currents produced as a consequence of the applied magnetic field (see Figure 7). These eddy currents are a natural result of the application

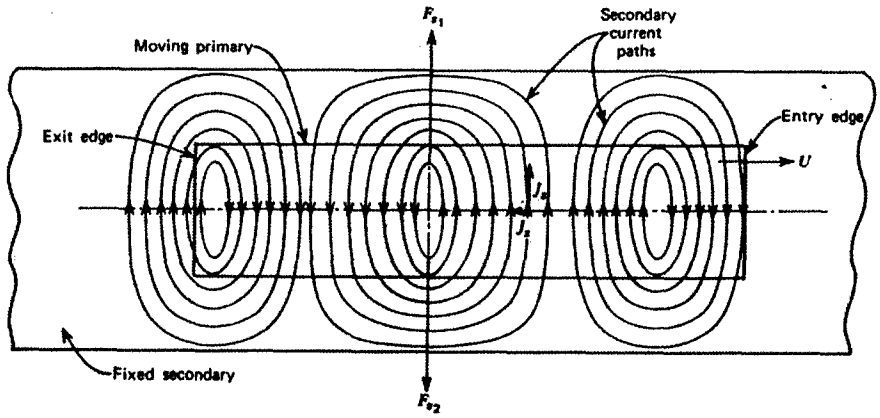

Figure 7 Transverse Edge Effects [10]

of the time-varying magnetic field across the secondary, which in turn generates a magnetic field to satisfy Faraday's Law. The components of the induced currents that flow in the x-direction serve to increase the effective resistance of the secondary [10]. An increase in the effective resistance of the secondary in turn increases the magnetic time constant, which exacerbates end effects, as well as increases resistive heating losses. Both of these serve to decrease the overall efficiency of the motor. As the amount of secondary overlap increases, the component of the current in the x-direction under the primary decreases, thus reducing the overall transverse edge effect. However, for many designs, this sort of overlap may not be possible, and the overlap itself can create other problems.

2.1.3 Leakage Flux

Linear induction motors generally have a larger airgap than conventional rotary induction motors. In high-speed applications, this is generally due to the fact that any mechanical interaction between the primary and the secondary can cause significant damage to the machine, and the track (secondary) bends for corners [14]. As a result, airgaps are deliberately larger in high-speed DSLIM. Many high-speed rail prototypes use guide-rails to guide the secondary through the primary to prevent interactions between the primary and the secondary. This has the result of increasing the relative reluctance of the of the airgap in the transverse direction (the direction that links flux with the pole on the opposite side, see Figure 8) and hence decreases the amount of flux

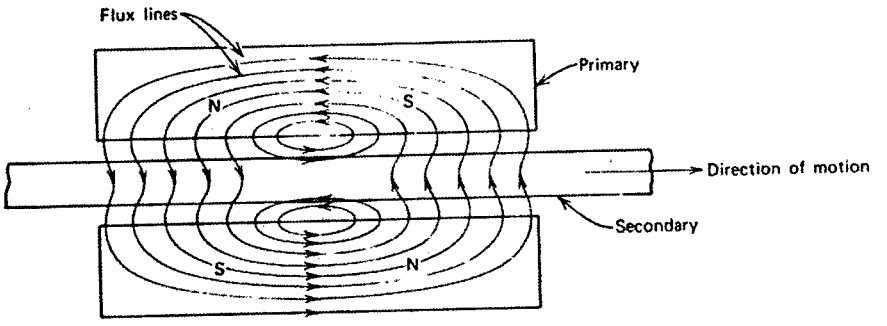

Figure 8 Leakage Flux [10]

that flows to produce thrust. This effect is more pronounced as the pole length becomes small with respect to the airgap. As this occurs, the relative reluctance of the transverse airgap becomes large with respect to the relative reluctance of the longitudinal airgap, and thus more flux is lost. This also has the effect of increasing the overall inductance of the motor, causing it to consume more reactive power and thus subjecting it to more resistive losses in the cabling and motor coils.

Short secondary DSLIMs have the additional leakage problem of having a secondary that is shorter than the primary. Any field that crosses the airgap and does not pass through the shuttle (secondary), is also leakage flux because it does not couple the primary with the secondary. A short secondary DSLIM that has a primary of 90 meters is likely to have a secondary that is on the order of 5 meters long. This means that, without track sectioning, the shuttle would couple with approximately 5% of the total flux, leaving approximately 95% of the flux to leakage.

2.1.4 Magnetic Field Spatial Harmonics

The eddy currents that the spatial harmonics create in accordance with Ampere's Law serve to cause resistive heating of the secondary and hence add to motor losses. In the ideal model of a LIM, the primary current sheet is modeled as a perfect, sinusoidally-distributed current source that serves to excite magnetic fields across the secondary. Because of the realities of motor winding, this is simply not possible. Instead, the coils that carry the primary current are usually located in slots cut into the primary ferromagnetic surface. This primary ferromagnetic surface tends to focus the flux through the top of the slots, thus creating step jumps in flux density as the secondary passes by each slot. The difference in magnetic field strength between one part of the secondary and an adjacent part creates a current in accordance with Faraday's Law, which circulates around the secondary and produces resistive losses due to the finite resistivity of the secondary. These step jumps in magnetic field strength can also serve to

create small steps in thrust, thus creating a less controllable, and possibly less comfortable, motor.

2.1.5 Time Harmonics

In an ideal world, the LIM would be driven by an ideal voltage or current source that had no output impedance and generated a perfectly sinusoidal output under all load conditions. Of course, this cannot possibly be true. The shipboard distribution system will be driven by fixed 60 Hertz sources, and this 60 Hertz service will have to be rectified and then inverted to create a variable frequency drive for the LIM. These variable frequency drives generate high frequency harmonics at the switching frequency of the controller, and also induce low frequency harmonics on the distribution system because of the non-linear current load that they represent. All of these current harmonics serve to distort the traveling wave that the primary current loops generate, and those current harmonics that have no requisite voltage harmonic are incapable of producing any real power in the motor. Instead, these current harmonics only serve to add resistive heating losses to the motor, and thus reduce efficiency.

2.1.6 Phase Unbalances

Due to minor differences in manufacturing and secondary flux linkage, the impedance for each coil of the motor is slightly different. Simply stated, when exactly the same voltage is applied across the terminals of two different coils of the LIM, a different current will flow through each. This is due to the different resistivities and inductances of each coil. Because of these minor differences, the magnetic field will distort to a certain degree depending on the degree of the phase unbalance, and this will in turn reduce the motor's overall efficiency through a number of different mechanisms. These mechanisms include magnetic field saturation in certain areas of the core due to excessive flux as well as eddy current generation in the secondary [6]. These eddy currents are generated by exactly the same phenomenon as spatial harmonics because of the step change in magnetic field that is experienced as the secondary traverses through two different adjacent magnetic field strengths.

Chapter 3

3.0 Modeling of the DSLIM

3.1 One Dimensional Model

It was established in the previous chapter that a short secondary DSLIM would be the design choice for an EMALS. A representation of a short-secondary DSLIM is shown below in Figure 9.

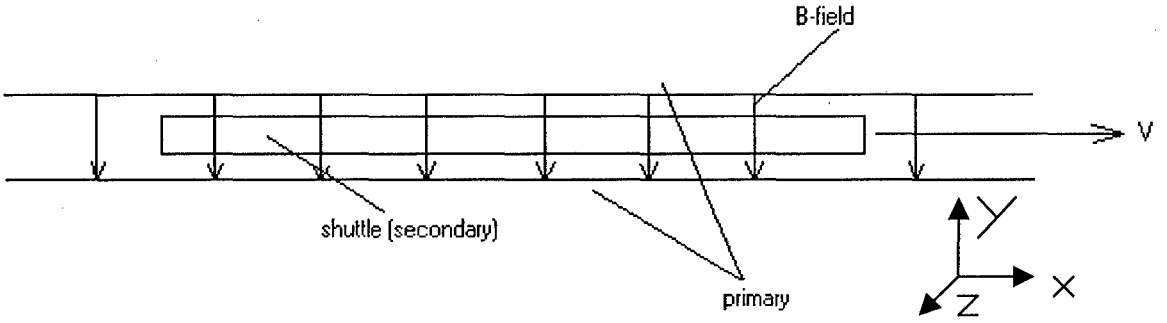

Figure 9 Long-Primary Short-Secondary DSLIM

The one-dimensional model assumes that the primary surface current on both sides of the shuttle is a perfect sinusoidal distribution in space and that it is driven by a perfect sinusoidal source (ie only the fundamental frequency). The surface currents on both the primary and secondary are coming directly out of the page (positive z-direction), the shuttle is moving in the positive x-direction, and the magnetic field is directed in the negative y-direction. Applying Ampere's Law, Faraday's Law, and Ohm's law to this system (a detailed derivation is located in Appendix A) gives:

$$g\cdot\frac{d^2B_y}{dx^2} = 2\cdot\mu_0\cdot\frac{dK_1}{dx} + \sigma_s\cdot\mu_0\cdot\left(\frac{dB_y}{dt} + v\cdot\frac{dB_y}{dx}\right)$$

Using this model for steady-state, one-dimensional analysis means that only the steady-state solution for thrust is used (end effect is neglected):

$$\text{Thrust} = \frac{D}{2}\cdot K_1\cdot B_y\cdot L\cdot\cos\left(-\delta_b\right)$$

L = length of secondary (shuttle)
D = depth of primary

$$\delta_b = \tan^{-1}\left[\frac{g\cdot\pi}{\sigma_s\cdot\mu_0\cdot\tau\cdot\left(V_s - V\right)}\right]$$

$$B_y = \frac{2\cdot\mu_0\cdot K_1}{g\cdot\frac{\pi}{\tau}\cdot\sin\left(\delta_b\right) + \sigma_s\cdot\mu_0\cdot\left(V_s - V\right)\cdot\cos\left(\delta_b\right)}$$

$K_1 = K_1 \cdot \sin(\omega \cdot t - k \cdot x)$ primary current

$k = \frac{\pi}{\tau}$ τ = pole pitch (meters)

$\omega = \frac{\pi}{\tau} \cdot V_s$ V_s = synchronous speed

g = airgap length

d = secondary thickness

V = shuttle speed

$\sigma_s = \sigma \cdot d$ (surface conductivity)

Thus thrust will equal zero at zero slip conditions, and thrust is directly proportional to the primary current magnitude. Using a sample motor (see Appendix A), the thrust versus slip profile is as seen below in Figure 10.

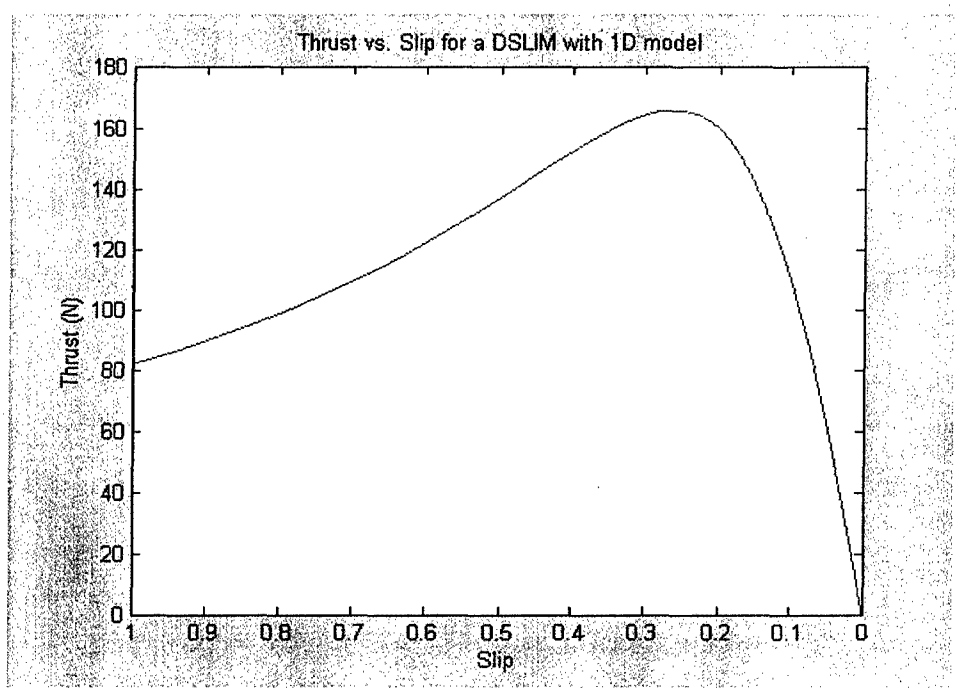

Figure 10 DSLIM with no end effect

As expected, this is a classic induction motor curve.

Because the short-secondary DSLIM has a secondary that is constantly immersed in a magnetic field, the end effects are not the same type of phenomenon in a short-secondary as they are in a short-primary DSLIM. This is largely due to the magnetic time constants of the secondary conducting sheet. In a short primary DSLIM, new parts of the secondary are constantly covered and uncovered by the primary. As this occurs, it takes time for the secondary to come to equilibrium with the applied field, and as this occurs, the field is weakened and distorted at the exit and entry ends of the primary. This distortion increases with speed because these time constants allow the distortion to

progress further into the primary, further reducing thrust. In a short secondary DSLIM, the primary field sweeps forward over the secondary at slip speed, which is much less than the actual shuttle (secondary) speed. This makes the end effect phenomenon in short secondary DSLIM a much more benign effect [12]. End effects in short secondary DSLIM will be discussed in the next section.

As a check of the model's usefulness, the airgap is decreased to see the effect of the average thrust. A smaller airgap should increase the average thrust.

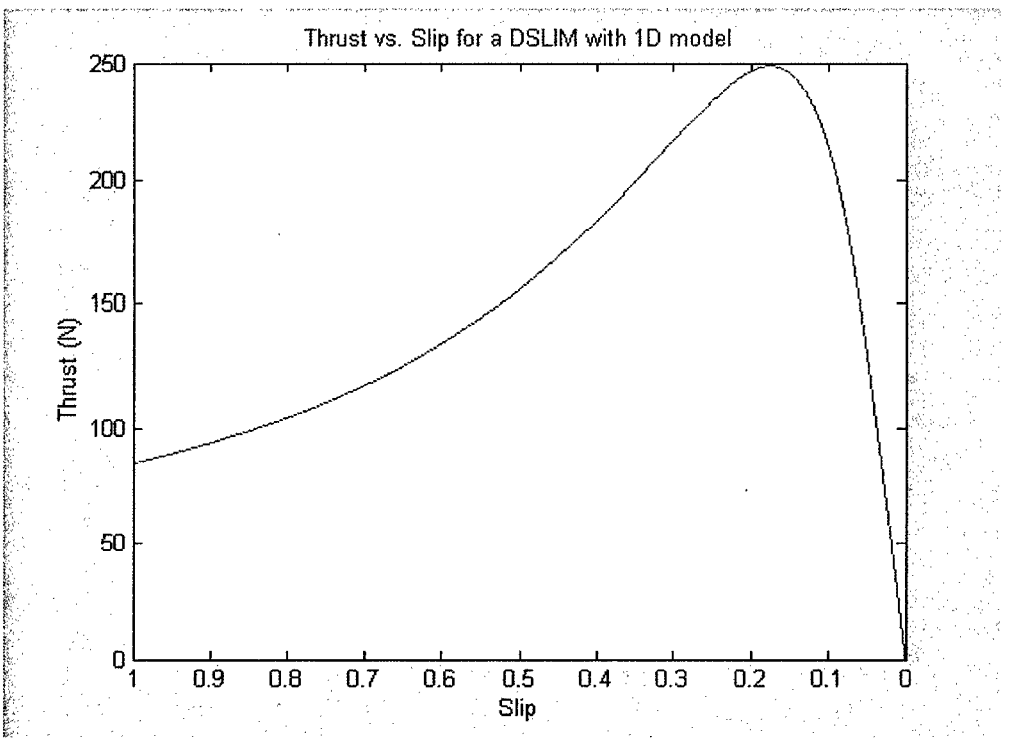

Figure 11 DSLIM with smaller airgap

As Figure 11 shows, decreasing the airgap by 5mm does in fact increase the thrust output from the DSLIM. In a further investigation of the model's usefulness, the airgap is increased 5mm (back to the original airgap of 15mm), and the secondary conducting sheet is increased by 5mm. This should have the effect of increasing surface conductivity and decreasing thrust.

As seen in Figure 12, the thrust at a zero speed is roughly one half of its value in Figure 10. This is typical of induction motors, and many rotary induction motors have a means of augmenting their secondary resistance to increase starting torque using rotor bar shaping, while keeping their secondary resistance low for efficient steady-state operation. This is not possible in a DSLIM.

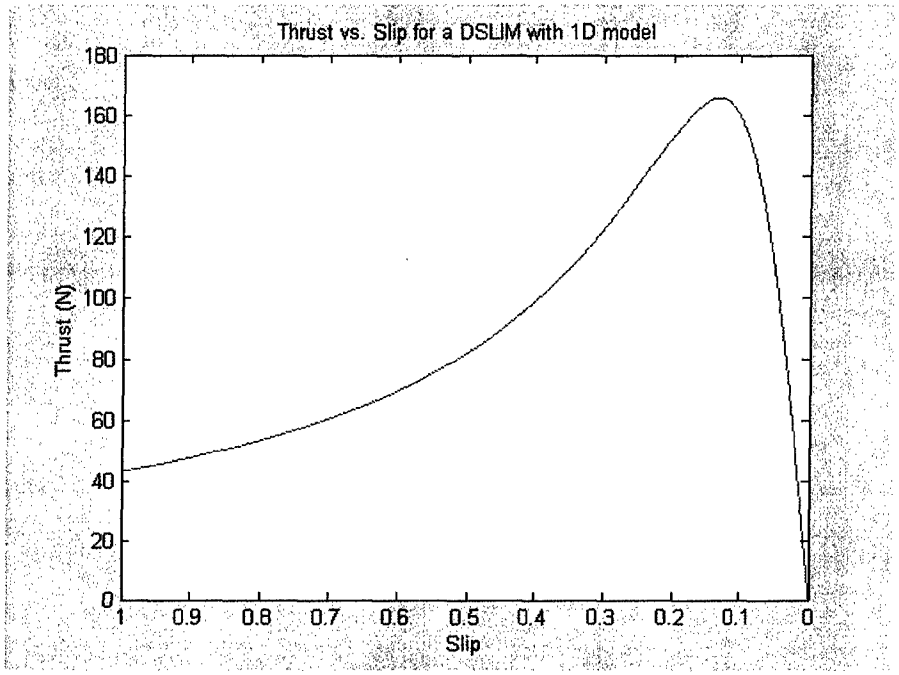

Figure 12 DSLIM with thicker secondary

3.2 Magnetic Diffusion and the End Effect in Short Secondary DSLIM

As stated in Section 3.1, the short secondary type of DSLIM is a unique type of high-speed LIM due to the fact that the secondary is shorter than the active (field-generating) portion of the primary. Magnetic diffusion and Ampere's Law are the primary mechanisms by which end effects occur in both types of LIM (short primary and short secondary), but the differences in geometries and inertial reference frames makes the end effect in short secondary DSLIM quite different.

A few assumptions must first be made with regard to the short secondary DSLIM:

- The primary applied field is perfectly sinusoidal
- The secondary is traveling at a constant speed and constant slip

The process of a pole peak passing over the rear end of the secondary at slip speed is shown graphically in Figure 13. Because the secondary is assumed to be several

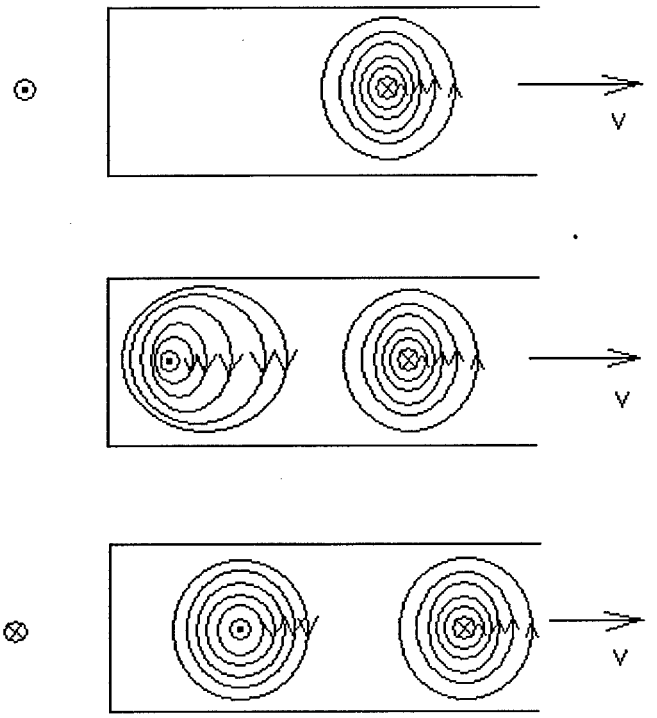

Figure 13 Magnetic Field Peaks and Induced Secondary Currents

primary pole pitches in length, it is assumed that the magnetic field will be nearly undistorted through the middle of the secondary, and will distort at the ends of the secondary only as pole peaks enter and exit the secondary. Figure 13 shows the shuttle moving to the right at velocity V that is just slightly less than the synchronous velocity. The pole peaks of the applied magnetic field sweep forward over the shuttle from front to back at slip speed, which is the difference between the synchronous velocity of the applied magnetic field traveling wave and the forward speed of the shuttle. This induces

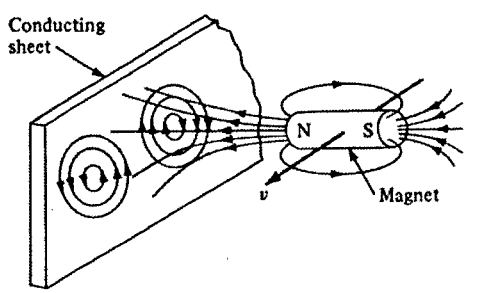

Figure 14 Induced Currents in the Shuttle [15]

currents in the shuttle which oppose the applied magnetic field according to Faraday's

Law. Thus a repulsive pole will be induced ahead of the applied pole and an attractive pole will be induced behind the applied pole (see Figure 3). These poles must satisfy Ampere's Law:

$$\nabla \times H = J$$

Thus due to the curl of current that a pole creates within the secondary, conservation of charge dictates that a full-pole must pass in order to complete a circuit. An illustration is provided in Figure 15 to show what would happen if a pole peak were to just hit the back surface of the shuttle (ie only half of a pole was to be present in the rear of the secondary). Conservation of charge dictates that the currents caused by the curl of the magnetic field must form a closed loop, but they are prevented from forming a closed loop by the back edge of the secondary. As the magnetic field continues to sweep forward, the field will deform to allow a current loop to form on the back edge of the shuttle (as illustrated in Figure 13). This process will continue to the forward edge of the shuttle and will eventually reach equilibrium as the magnetic field diffuses through the secondary and the resistance to the current on the back edge of the shuttle decreases.

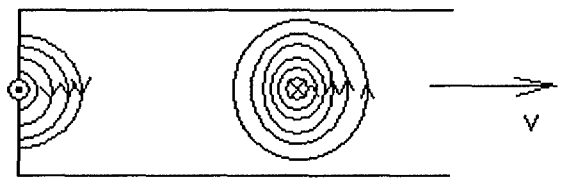

Figure 15 Half-Pole Current Pinch on Secondary

The previous model for the DSLIM assumed an infinitely long shuttle and paid no attention to closed current loops on the shuttle. The new model will look at a DSLIM in which the secondary is a finite length and will apply boundary conditions on the shuttle current to ensure charge conservation is maintained with closed current loops. The new DSLIM model is shown below in Figure 16.

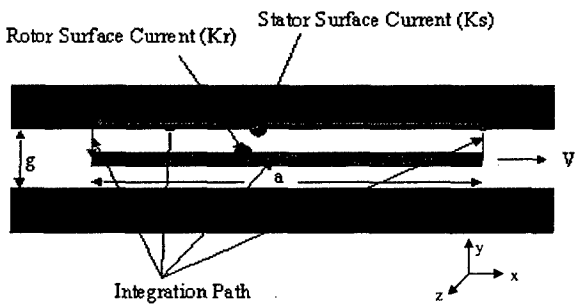

Figure 16 Short Shuttle DSLIM Model

It is assumed that the airgap magnetic field is y-directed only, and varies sinusoidally in time and space. Ampere's Law around the red loop gives:

$$\frac{1}{2}\cdot\frac{g}{\mu}\cdot\frac{dB_y}{dx} = K_S + K_I$$

Where the stator surface current density is of the form:

$$K_S = K_o\cdot e^{j\cdot\frac{\pi}{\tau}\cdot\left[x-\left(V_S-V\right)\cdot t\right]}$$

It is further known that the magnetic field will be of the form:

$$B_y = B_o\cdot e^{-j\cdot\frac{\pi}{\tau}\cdot\left(V_S-V\right)t}$$

And that the induced electric field in the shuttle will take the form:

$$\frac{dE_z}{dx} = \frac{dB_y}{dt}$$

Thus, after taking a second derivative and substitution of the above known variable forms, the airgap field equation becomes:

$$\frac{d^2B_o}{dx^2} = \frac{2\cdot\mu}{g}\cdot\left[j\cdot\frac{\pi}{\tau}\cdot K_o\cdot e^{j\cdot\frac{\pi}{\tau}\cdot x} - j\cdot\sigma_r\cdot\frac{\pi}{\tau}\cdot\left(V_S - V\right)\cdot B_o\right]$$

A detailed derivation of the solution to this differential equation is provided in Appendix B. In order to solve for the unknown constants of integration of the homogeneous solution, boundary conditions at the ends of the shuttle had to be established. Laithwaite suggests that the magnetic field must be a continuous function across the shuttle-airgap boundary [9]. Implicit in this statement is that the shuttle current must sum to zero across the full length of the shuttle, which is precisely the physical condition that must exist in order to preserve conservation of charge.

Thus, a second model had to be formulated in order to solve for the unknown constants of integration. This model solved for the magnetic field around the shuttle by assuming the shuttle was not there. Since Ampere's Law requires that the total sum of

current through the surface is accounted for in the magnetic field formulation, and since the total sum of the shuttle current over the entire surface of the shuttle must be exactly zero, the magnetic field must be a function of the stator current only. The new model is shown in Figure 17.

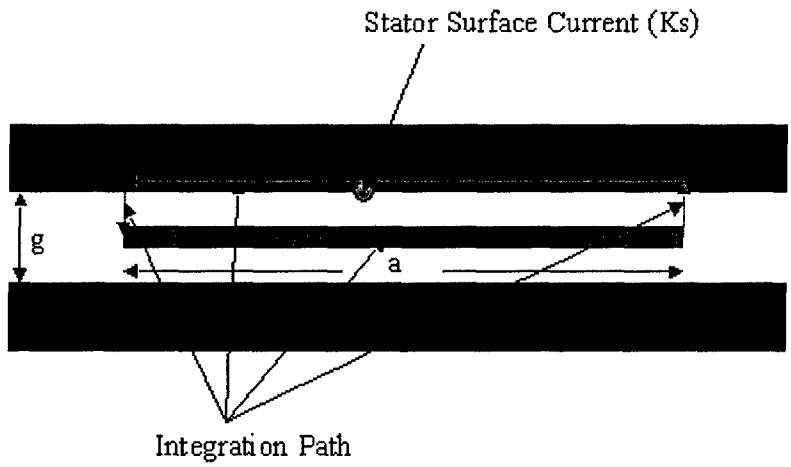

Figure 17 Model for Formulating Magnetic Field at Shuttle Ends

This model was then used to solve for the magnetic field at both ends of the shuttle. These solutions were then equated to the solutions just inside the ends of the shuttle from the model of Figure 16, and the unknown constants of integration were solved for.

Once the magnetic field was known over the entire surface of the shuttle, the magnetic field was used to derive the shuttle surface current function. A detailed derivation of the shuttle surface current density is located in Appendix B. The general solution is:

$$K_r = -j\cdot\sigma_r\cdot\left(\frac{\pi}{\tau}\right)\cdot(V_s - V)\cdot e^{-j\cdot\frac{\pi}{\tau}\cdot(V_s - V)\cdot t}\cdot\left(-j\left(\frac{\tau}{\pi}\right)\cdot C_o\cdot e^{j\cdot\frac{\pi}{\tau}\cdot x} - j\cdot\frac{1}{\alpha}\cdot C_1\cdot e^{j\cdot\alpha\cdot x} + j\cdot\frac{1}{\alpha}\cdot C_2\cdot e^{-j\cdot\alpha\cdot x}\right) + C_3$$

In order to find the constant of integration, the finite length shuttle surface current boundary condition dictates:

$$\int_0^a K_r\,dx = 0$$

Thus the magnetic field and shuttle surface current are now specified completely over the entire surface of the shuttle.

Figure 18 shows a plot of the magnetic field over the surface of the shuttle for various values of slip. The field sweeps from left to right at slip speed.

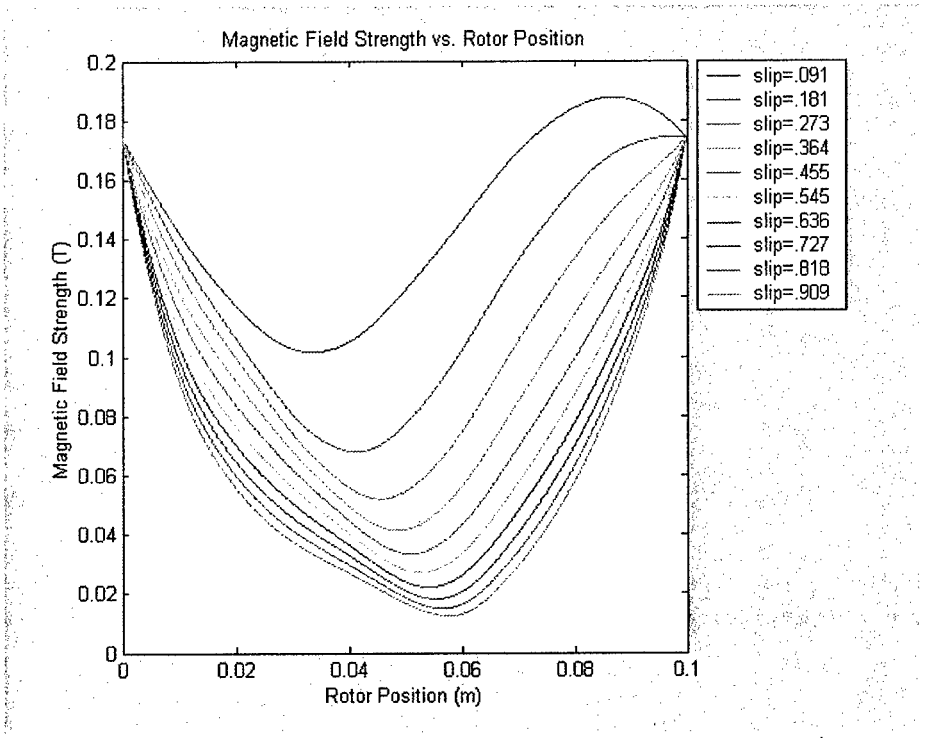

Figure 18 Magnetic Field versus Shuttle Position (shuttle length = tau)

As slip speed increases, the field strength in the airgap at the surface of the shuttle decreases due to the induced opposing field on the shuttle. In this example, the shuttle is exactly 1 pole long. Figure 19 shows the same type of plot, but this time the shuttle (shuttle) is exactly 2 poles long.

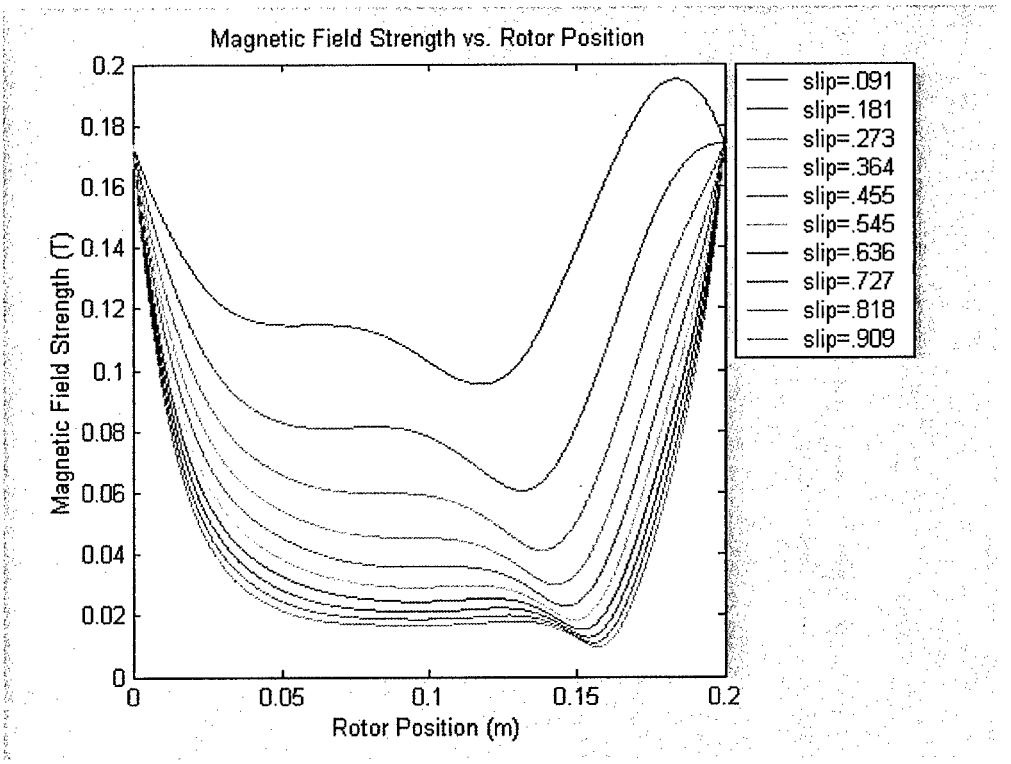

Figure 19 Magnetic Field versus Shuttle Position (shuttle length = 2*tau)

As might have been expected, a longer shuttle with a constant pole pitch produces a more even magnetic field along the length of the shuttle. This is because the magnetic field has had a chance to diffuse after approximately a pole length, and thus the interior portions of the shuttle almost seem as though they are part of an infinite shuttle. One final look with a shuttle 5 pole pitches in length is shown in Figure 20.

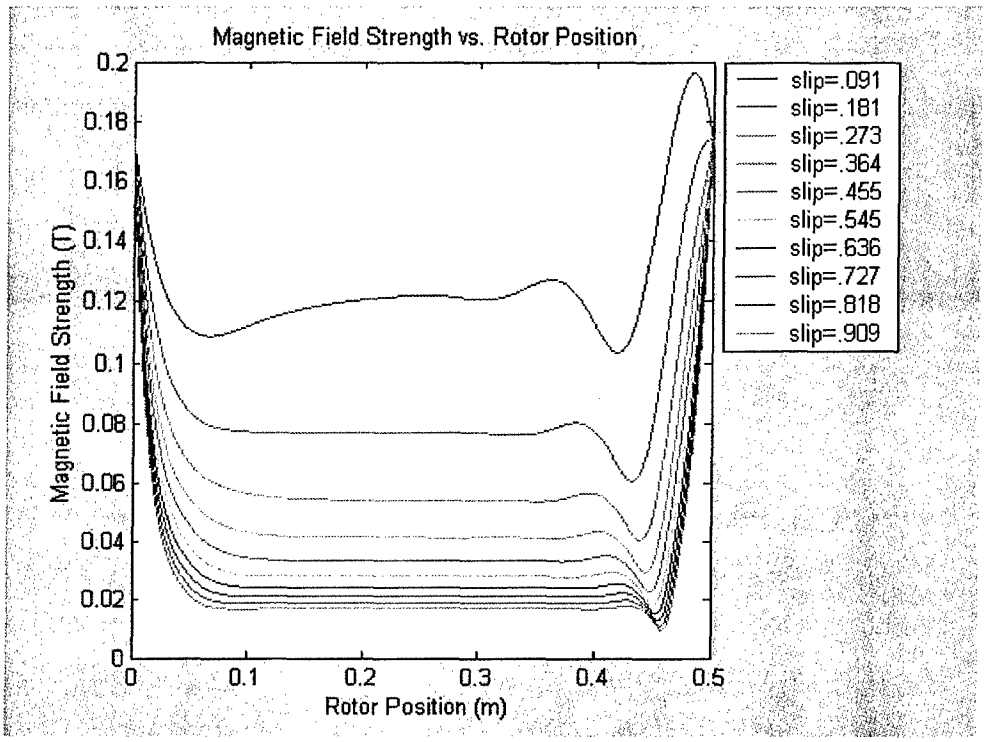

Figure 20 Magnetic Field versus Shuttle Position (shuttle length = 5*tau)

Clearly the magnetic field stabilizes across the surface of the shuttle with the end effect being confined to relatively small parts at the front and rear of the shuttle.

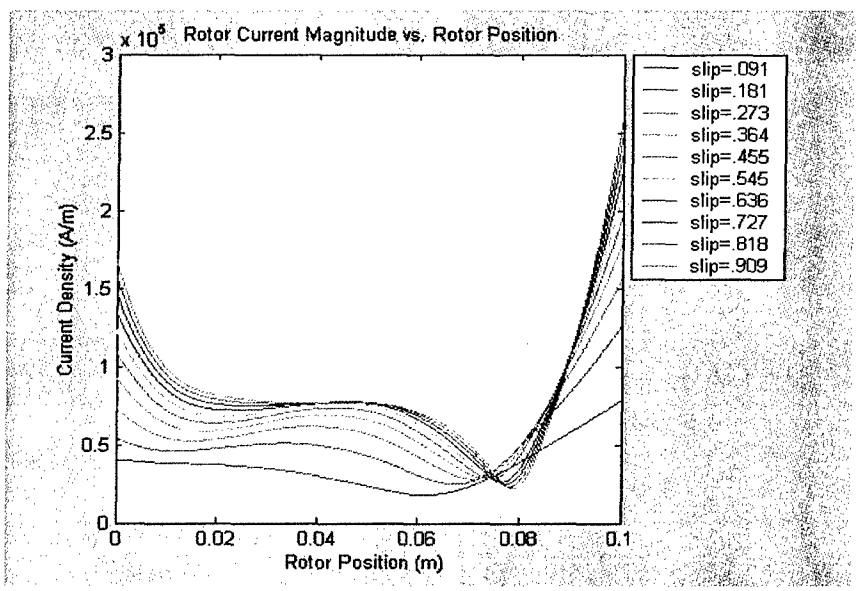

Figure 21 Shuttle Surface Current versus Shuttle Position (shuttle length = tau)

Turning attention to shuttle currents, the shuttle length is returned to 10cm (1 pole pitch) and the shuttle currents are plotted versus shuttle position for various slips in Figure 21. Not surprisingly, the shuttle surface current magnitude tends to peak at both ends of the shuttle, in unison with the airgap magnetic field at the ends. Also not surprising, the induced shuttle current magnitude decreases with decreasing slip.

Changing the shuttle length to 2 pole pitches produces Figure 22. Again, with an increase in shuttle length, the surface currents in the interior of the shuttle tend to stabilize to some spatially steady state value. The end effects are largely concentrated in front and back of the shuttle.

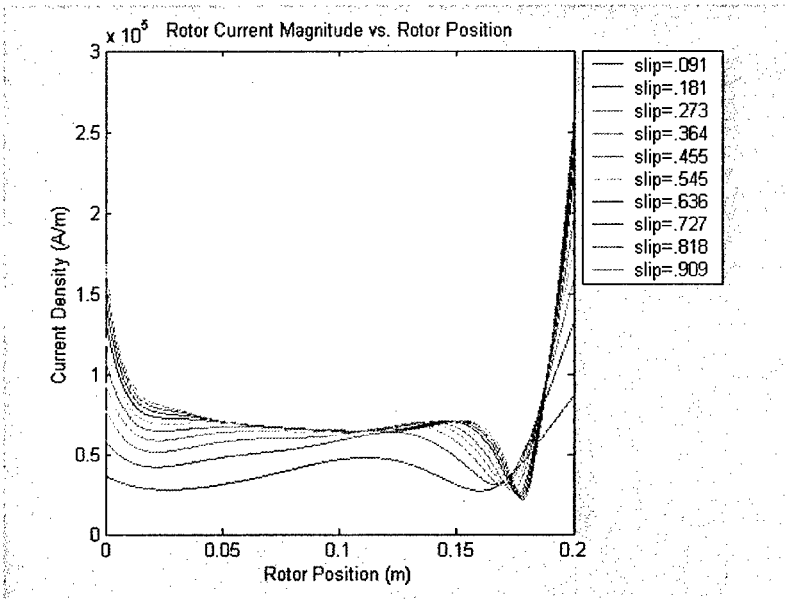

Figure 22 Shuttle Current Density versus Shuttle Position (shuttle length = 2*tau)

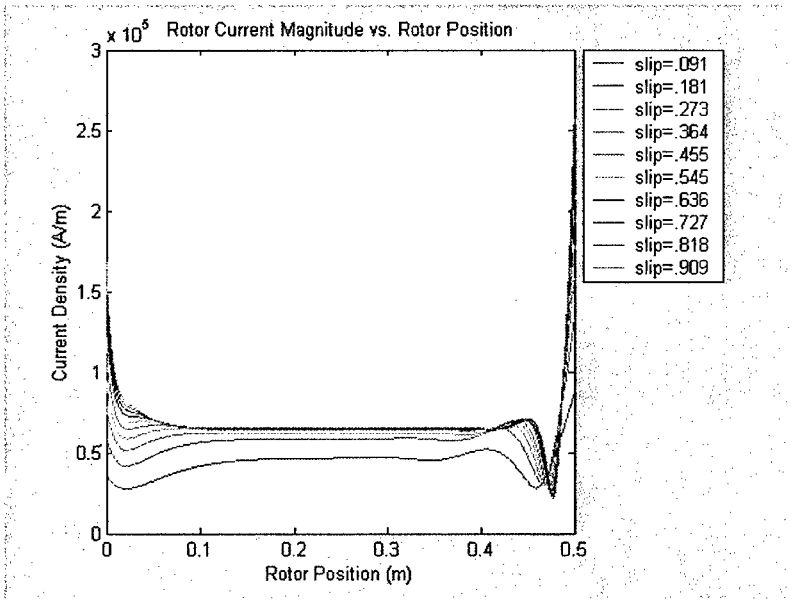

Figure 23 Shuttle Current Density versus Shuttle Position (shuttle length = 5*tau)

Figure 23 shows the effect on shuttle surface current of making the shuttle 5 pole pitches long. Thus, the shuttle will be 50 cm long. The progression here is that as shuttle (shuttle) length is increased, the deleterious consequences of the end effects will be marginalized. It is important to remember in this derivation of end effect that there is no limit applied to the current in the shuttle. A fairly significant peak of current is seen at the front of the shuttle, and depending on the material and geometry of the shuttle, this could create a heating problem. An increase in temperature will cause an increase in resistivity, and that could significantly impact the local current density profile.

The net result of end effects is now investigated. The time average value of thrust is given by Poynting's Theorem as:

$$F = \int_0^a .5 \cdot K_r \cdot B^X \, dx \qquad B^X = \text{conjugate of B}$$

Thus the product of the shuttle surface current density multiplied with the local magnetic field strength and integrated over the length of the shuttle will yield the time average thrust per unit depth of shuttle. Figure 24 plots normalized force versus slip for a shuttle with end effect and a shuttle without end effect. Both shuttles are 10 cm, or one pole pitch long.

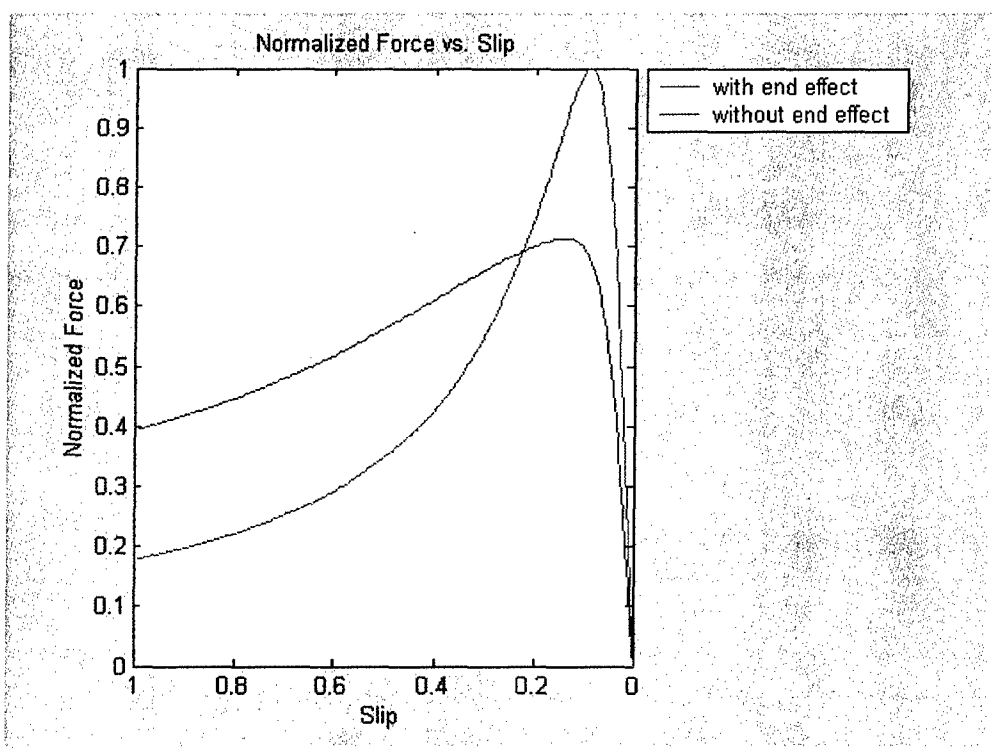

Figure 24 Normalized Force versus slip (shuttle length = tau)

Clearly the end effect has a deleterious effect on the peak force, but an interesting result is that the DSLIM with end effect seems to have a higher force in the high slip region than the DSLIM without end effect. The starting torque of the machine with end effect appears to be approximately twice the value of the starting torque of the machine without end effect. This result is consistent with Laithwaite [9]. This would seem to indicate an increase in shuttle resistance.

Recognizing that increasing the length of the shuttle (shuttle) had the effect of marginalizing the end effect, the shuttle length was increased to 5 pole pitches to see how the torque speed curve of the motor with end effect compared to that of the motor without end effect. The result is shown in Figure 25.

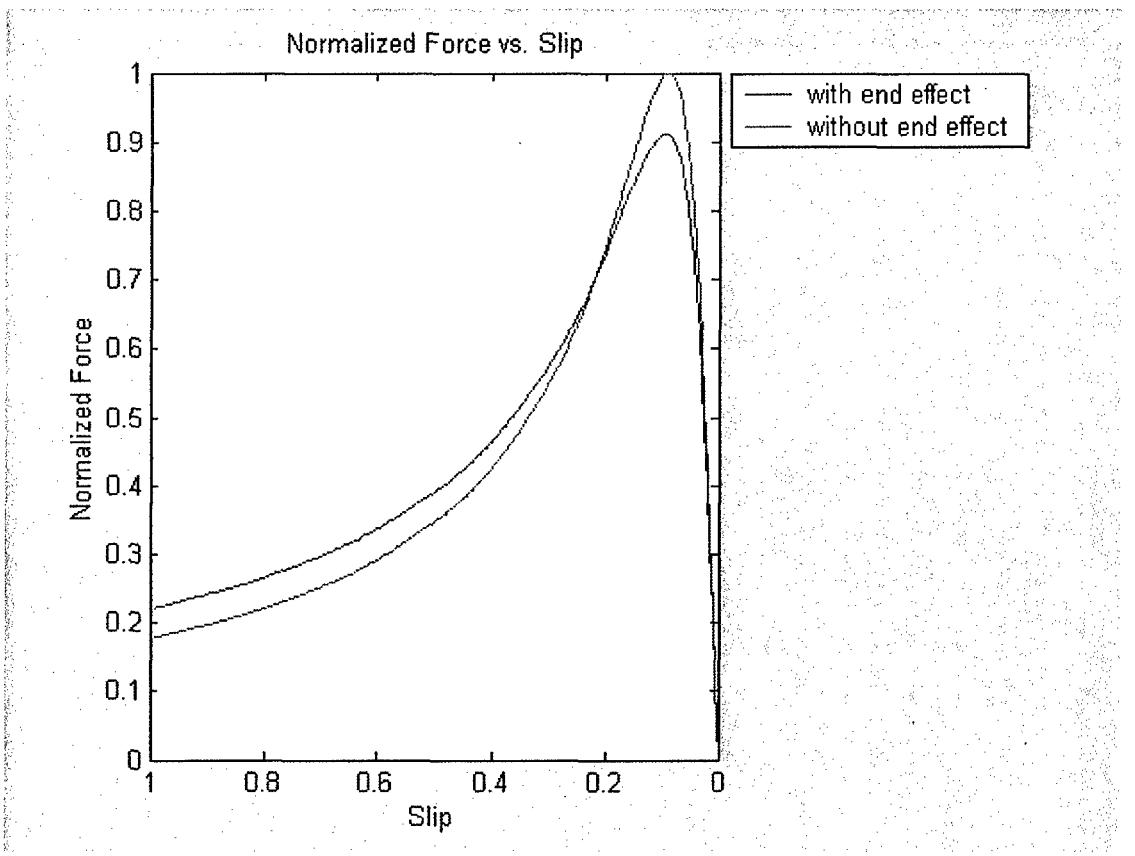

Figure 25 Normalized Force versus slip (shuttle length = 5*tau)

Clearly the graph of the motor with end effect is now approaching the graph of the motor without end effect. As the number of pole pitches that the shuttle spans increases, the two graphs will end up being coincidental. This is an entirely expected result since the original one-dimensional model assumed an infinitely long shuttle.

There are still end effects that are present even when the shuttle is long compared to pole pitch. These end effects are a result of two dimensional field effects at the ends of

the shuttle due to the discontinuity in the airgap conductivity caused by the shuttle. These effects will not be simulated here.

These results will be used in later sections to develop a transient model of the DSLIM. The above models were developed based on the assumption that there was no bending of the magnetic field within the airgap, and that the applied current was perfectly spatially distributed in a sinusoidal fashion with only the fundamental component of the current present. It is thought that the above models are good representations of the end effect in a time average sense, and give a good indication as to how the end effect can adversely affect the operation of a DSLIM.

3.3 Magnetic Field Spatial Harmonics

As discussed earlier in Section 2, magnetic field spatial harmonics are the result of concentrating magnetic flux lines into the teeth of the back iron before the flux lines cross the air gap [9]. This is due to the low reluctance path that the teeth present compared to the high reluctance path that the slot and conductor present. Thus, the flux preferentially concentrates in the teeth and presents a discontinuity in the field across the airgap. When this field discontinuity interacts with the secondary (shuttle), eddy currents are produced causing additional resistive heating losses in the shuttle. This adversely affects performance and contributes to an overall reduction in efficiency. Additionally, this step jump in the field can produce a jerk in force, known as cogging. This cogging is also undesirable in the pursuit of a controllable, smoothly accelerating DSLIM that is capable of launching valuable aircraft.

Spatial harmonics are modeled with Fourier Analysis. It is known that the magnetic field is periodic over the length of two pole pitches. It is also known that every slot in the back iron will hold a conductor that will contribute to the magnetic field. Therefore, every tooth of the primary back iron will cause a step jump in the magnetic field of the airgap. With this information, and assuming a multi-phase, balanced current source, the Fourier coefficients and functions were derived (see Appendix C).

Given the Fourier series that described these spatial harmonics, attention was placed on determining what was required to minimize the harmonics that were present. The ultimate goal was to produce something that was very close to an actual sine wave. Short-pitching, shuttle skewing and multiple phases have been the traditional methods used to reduce spatial harmonics and cogging in conventional rotary machines. This analysis will concentrate on short-pitching and multiple phases as a means of reducing

spatial harmonics. To start the analysis, a 3-phase, 5/6-pitched DSLIM is analyzed for spatial harmonics (see Figure 26).

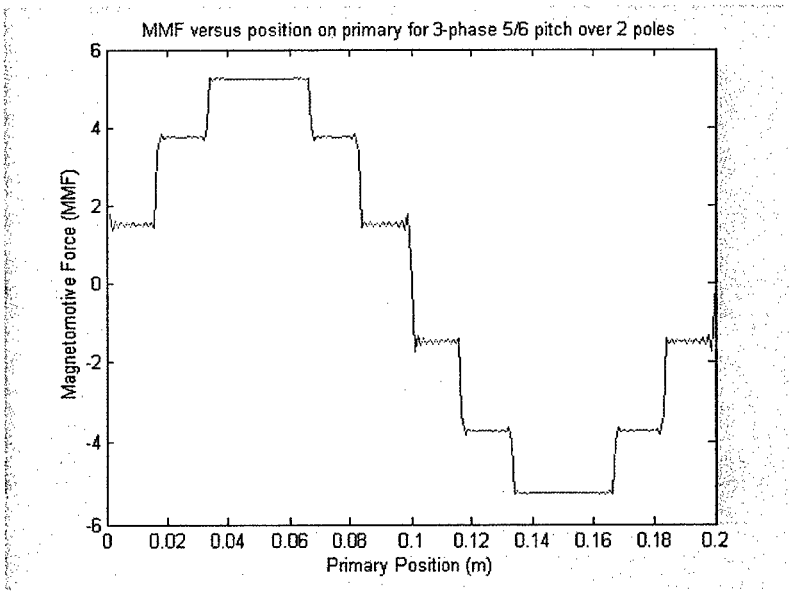

Figure 26 MMF as a function of primary position over 2 poles (3-phase)

Over 2 poles, or a full wavelength of the primary field, there are distinct discontinuities. There is also a distinct fundamental component to this mmf wave, but the harmonics create substantial distortion. Figure 27 shows the result with 6 phases

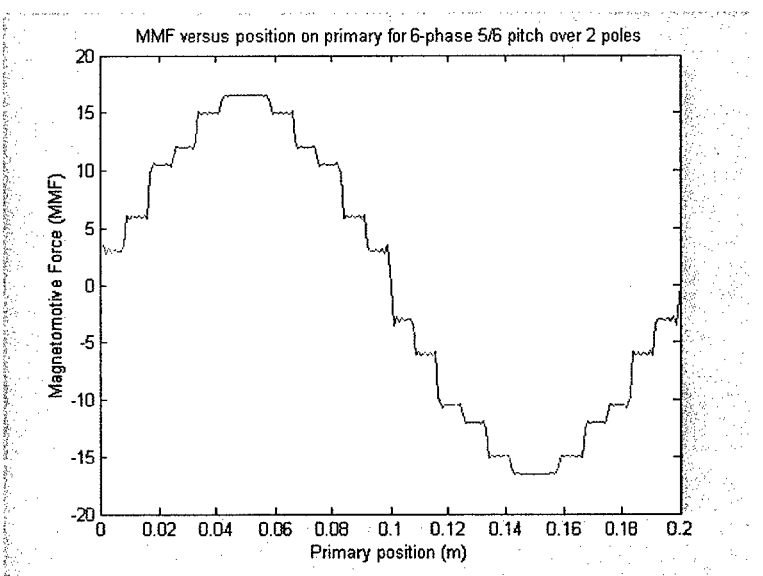

Figure 27 MMF as a function of primary position over 2 poles (6-phase)

This is clearly a better result, with the fundamental now dominating the shape of the curve. However, since the pole pitch is only 10cm, having six phases at 2 slots per pole per phase is probably the maximum phase density that can be achieved (equates to 1.2 slots per cm).

On a side note, these pole pitches are also not likely to be used on a DSLIM capable of launching an aircraft. However, this data is only meant to get a feel for the effect of varying the number of phases on the spatial harmonics. These pole pitches are used because research has been done in the past on DSLIM of this size range, and it is helpful to compare results with existing data from previous research.

Continuing with the discussion of reducing spatial harmonics, previous research has indicated that a 15-phase system gives an extremely good mmf sine wave in the airgap. The simulation is run once again with a 15-phase system and a new pole pitch of 30cm with $5/6^{th}$ pitching (see Figure 28).

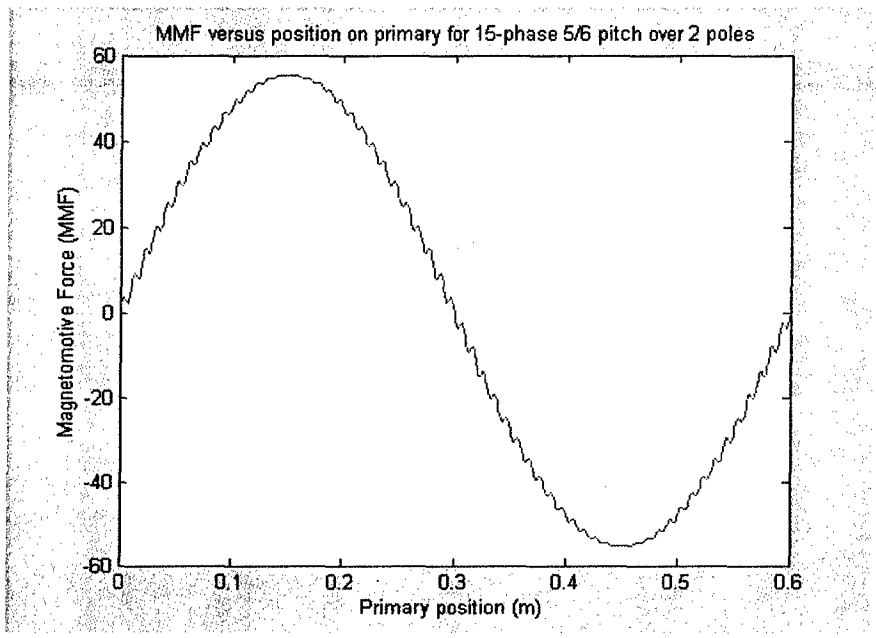

Figure 28 MMF as a function of primary position over 2 poles (15-phase)

This is an excellent result, and effectively neutralizes low order harmonics. The fundamental is the dominant component, and only small high-frequency perturbations can be seen. This makes a pretty convincing argument to build a 15-phase motor, especially when 15 phase motor controllers are available and easily built with modern power electronics. The drawback here is that the pole pitch had to be increased to fit the extra phases in. With the same flux density across the airgap, this causes the back iron to saturate unless thicker piece back iron is used. Obviously, thicker back iron will be used to prevent saturation, but this increases the overall weight of the system. Given the nature (both structure and stability-wise) of where the EMALS DSLIM will be mounted, adding a lot of extra weight in the form of back iron can have a detrimental effect on the greater ship. This effect will be considered as part of an overall design synthesis.

The foregoing discussions have focused on reducing spatial harmonics created as a result of the back iron teeth. Noting that the back iron teeth create spatial harmonics, and that the end turns on linear motors make for a lot of wasted wire, Laithwaite proposed a novel solution. Laithwaite proposed that the teeth be removed altogether, and that the wire coils be laid in diamond shapes directly on the flat face of the back iron [14]. This is shown pictorially in Figure 29.

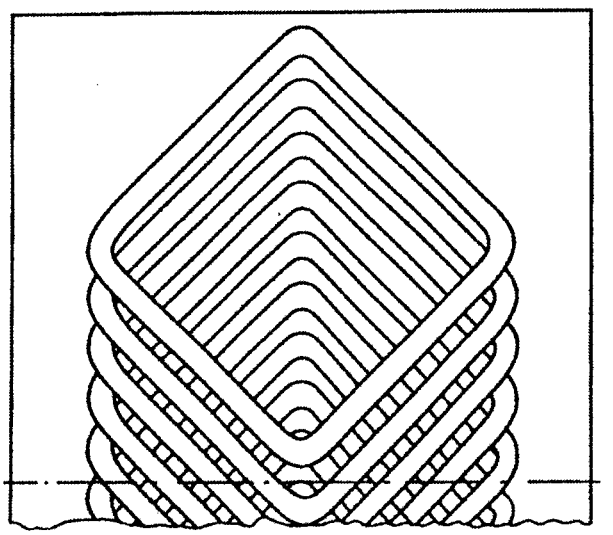

Figure 29 Winding Layout with no back iron teeth [14]

Clearly, this is an innovative way to get rid of the problems of spatial harmonics and wasted end windings. This creates two problems, however, in that no conductor length is completely orthogonal to the direction of the shuttle motion and that the magnetizing current for the motor will be larger.

The issue of orthogonality between the current carrying conductor and the shuttle results in an overall reduction in the force produced in each length of the conductor. However, now each conductor contributes to the thrust, and an overall net gain in thrust is expected.

The magnetizing current is an important issue here in that it can adversely affect the motor's power factor. Laithwaite never actually built a motor in this fashion, and therefore it is not known whether it is a viable option. Reactive power draw due to the magnetizing current might be compensated for by the use of capacitors.

Another novel approach in the effort to reduce magnetic field spatial harmonics is the use of a Gramme Ring Winding. The Gramme Ring Winding uses a straight piece of back iron with a square or rectangular cross-section for the stator, and winds the phases around the back iron as shown in Figure 30.

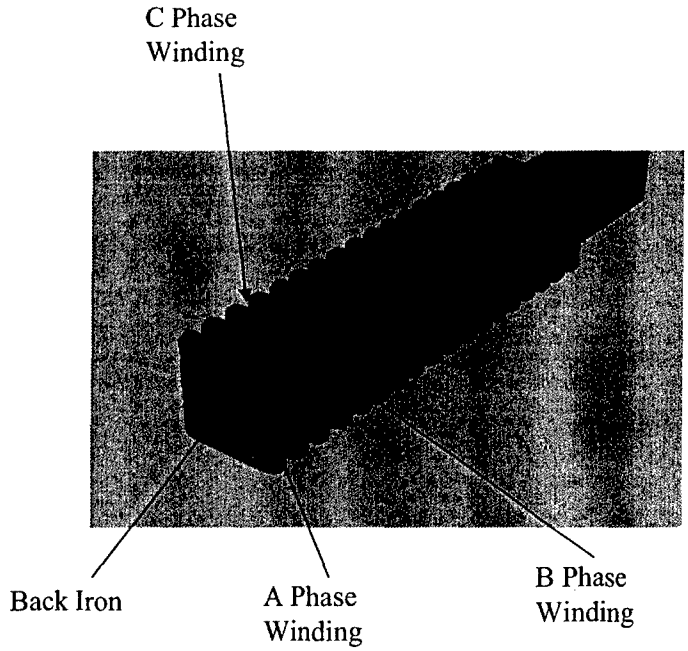

Figure 30 Gramme Ring Winding

Both Kirtley and Laithwaite advocate this method for the reduction of spatial harmonics because it uses no slots in the back iron and it effectively eliminates the tooth modulation of magnetic field spatial harmonics into the airgap [12], [14]. This is a more effective method than the diamond layout of Figure 29 because the windings are wrapped around the back iron, and hence the magnetizing current is lower.

3.4 Leakage Flux

Leakage flux is defined here as flux that does not cross the airgap to produce useful work. This process is shown graphically below in Figure 31 for a DSLIM.

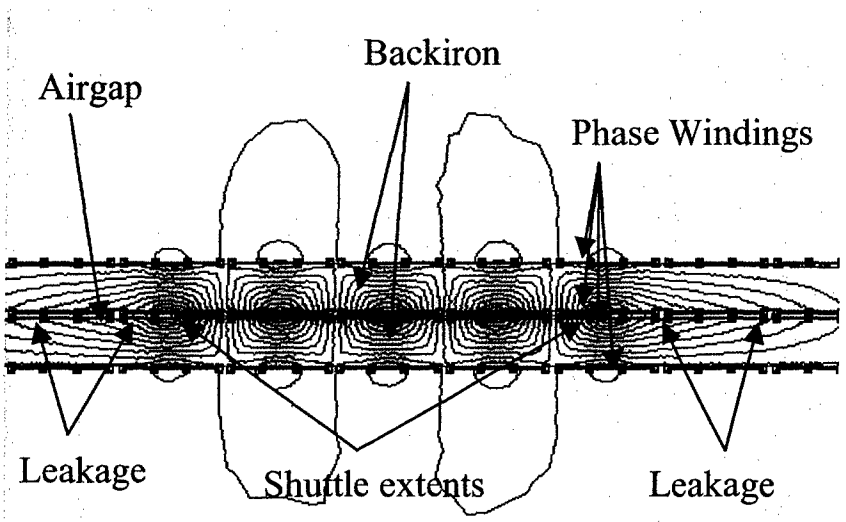

Figure 31 Leakage Flux (View from Above)

It is difficult to see, but there are two mechanisms by which flux is lost. Some of the leakage is caused by the pole changes. This is because the reluctance through the airgap (longitudinally) is less than the reluctance required to traverse the airgap transversely (and produce thrust). Thus the flux takes the path of least reluctance, and produces no work. However, a large portion is also lost because it crosses the airgap but fails to couple with the shuttle. Thus, this also produces no useful work.

The obvious answers to the first leakage mechanism are to increase pole pitch and decrease airgap. As with any well-designed machine, the airgap would be expected to be minimized to the maximum safe extent. Therefore, the pole pitch should be focused on, and increased to prevent leakage flux to the maximum extent possible. Of course,

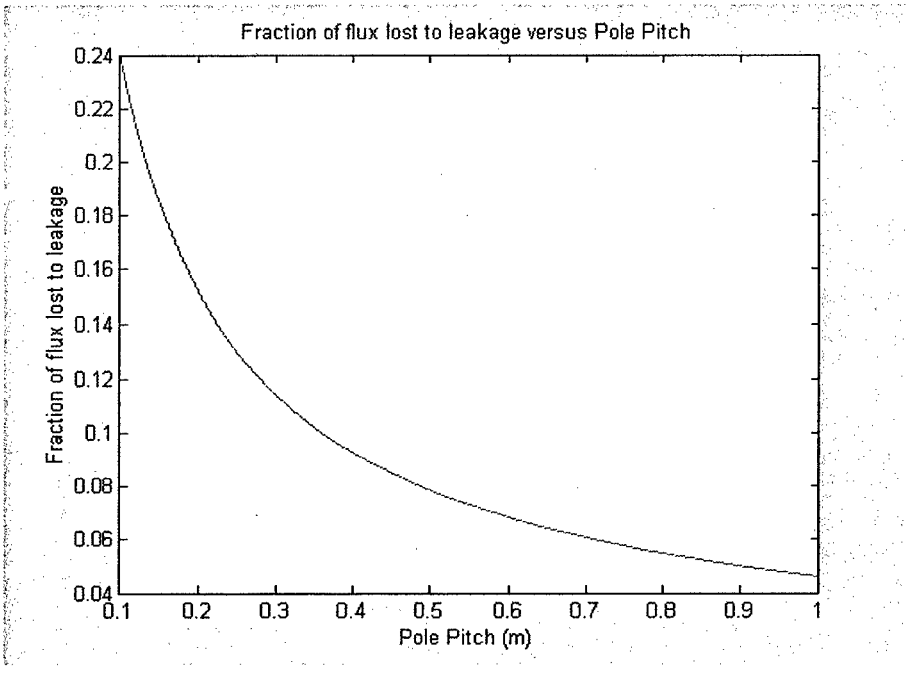

Figure 32 Flux Leakage versus Pole Pitch

increasing pole pitch will add to the weight of the back iron (assuming the flux density remains constant), and could become prohibitively heavy for shipboard applications. With an increased pole pitch, more flux is linked by virtue of the fact that the distance the flux has to travel to reach the opposite pole is relatively larger and also by the fact that there is simply more flux (assuming the flux density remains constant). Even with a larger pole pitch, the flux nearest to the opposite pole will continue to be lost as a function of the ratio of the distance to the opposite pole to the airgap distance. This ratio of distances represents the relative reluctance of the leakage path to the airgap path because the relative permeability of Copper or Aluminum is equivalent to that of free space. Figure 32 shows the relation of the percent of flux lost to leakage versus pole

pitch for a DSLIM with a constant 1 Tesla of flux density. Starting with a 10cm pole pitch and ending at 1m (with a constant airgap of 1cm), there is a clear exponential drop-off in the percentage of flux lost to leakage. At 60cm, almost all of the reward for the pole pitch length has been reaped with the percentage of flux lost being reduced by nearly a factor of 4 from that which was lost with a pole pitch of 10cm. Boldea and Nasar specify a correction factor to be used for this leakage flux which effectively increases the airgap [10]:

$$k_J = \frac{\sinh\left(\frac{\pi}{\tau}\cdot g\right)}{\frac{\pi}{\tau}\cdot g}$$

τ = pole pitch (m)
g = mechanical airgap (m)

This correction factor is multiplied times the mechanical airgap to produce the effective airgap. This correction factor is plotted in Figure 33 for the same motor of Figure 32.

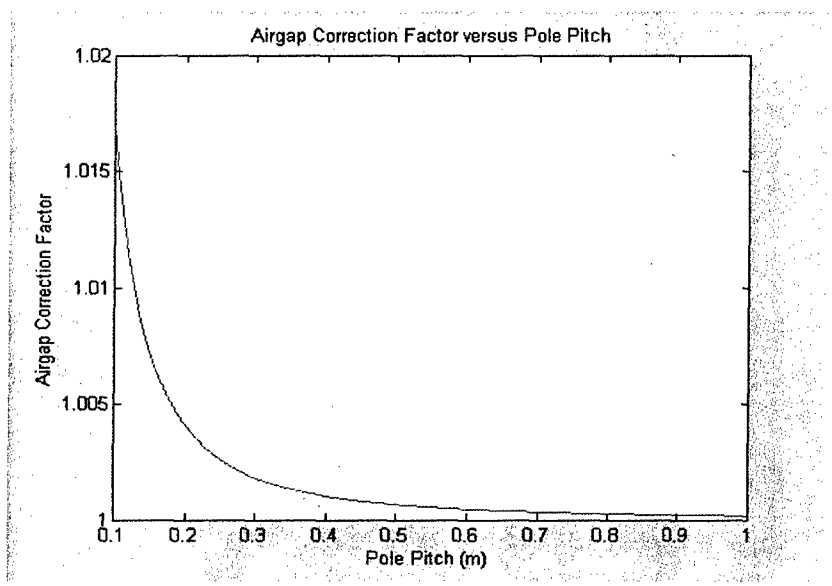

Figure 33 Airgap Correction Factor versus Pole Pitch

In order to address the second leakage mechanism, the track must be assembled and operated in sections. These sections must be activated whenever the shuttle (shuttle) is in the track adjacent to the applicable stator section. Thus, the flux is applied to those sections that can best produce useful work. Each track section represents a pole pitch, and each section is separated from adjacent track sections by an airgap. This airgap presents a reluctance to the magnetic flux, and forces more flux into the airgap where the shuttle is located, thereby coupling more flux and producing more net work. This is represented by Figure 34.

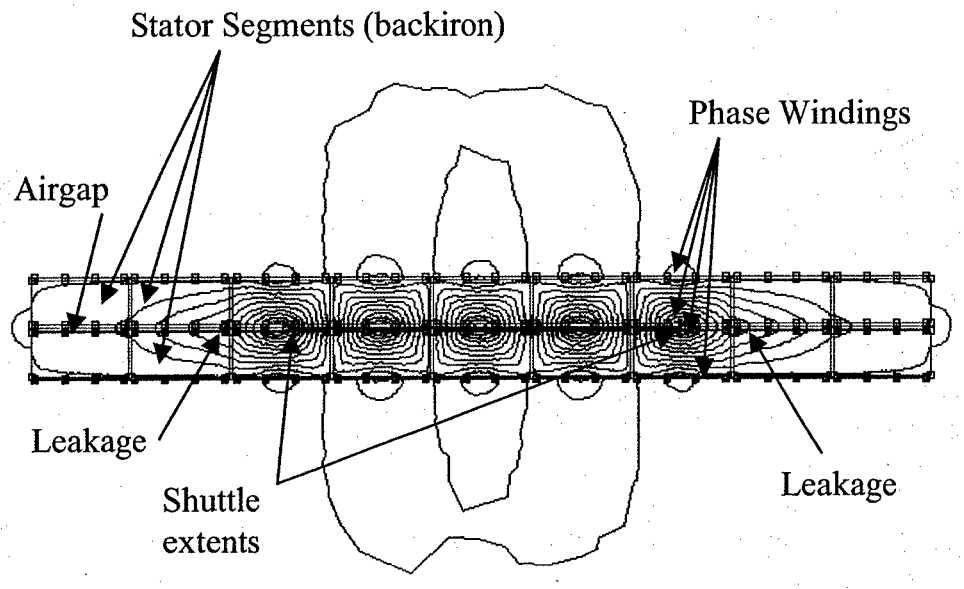

Figure 34 Leakage Flux With Track Segmentation (View from Above)

With 5 active poles and 4 inactive poles, and the shuttle completely under 3 poles while halfway under 2 poles, and airgaps between each stator section, the flux coupling between the stator and the shuttle has been drastically improved. The problem still remains that the shuttle will not couple all of the applied flux, but it is a better arrangement.

3.5 Phase Unbalance

Due to the nature of the long primary, short secondary DSLIM, portions of the primary will be uncovered (ie the shuttle will not be over them) while others will be covered. Because of this, the relative flux linkages of different coils in the active zones of the primary will produce different reactances as seen by the applied electromotive force. These reactances will in turn create a mix of real and reactive impedances along the entire active length of the primary, which will in turn cause a variety of currents to be drawn at a variety of phase angles. This is entirely undesirable because this will force the creation of a current return path due to the simple fact that these currents are no longer balanced (ie sum to zero at the motor star point).

The foregoing discussion has been predicated on the fact that the motor would be parallel wound. In a parallel wound DSLIM, each phase coil is separately connected to the source, thus allowing it to draw whatever current is necessary from the source depending on the amount of flux that the coil happens to be linking. Yamamura suggests a series wound motor in which all of the coils in each phase that are located in the active

part of the primary be connected in series [6]. Thus, the impedance in each phase is somewhat normalized over the length of the active portion of the primary. This does not completely eradicate the phase unbalance, however, because the non-uniformity of the flux over the shuttle will create slightly different flux linkages between each individual phase. This is especially true in those primary coils that are near the ends of the shuttle and subject to the end effect. The end effect can create a different flux linkage between two adjacent primary phases, thus causing a difference in impedance and creating an unbalanced three-phase load. This unbalanced three-phase current will need to return to the source through the motor's star connection. If there is no return connection at the motor's star, then the current will return through ground, creating a common-mode voltage on the star point, and possibly severely affecting the motor's operation.

3.6 Transverse Edge Effects

Because the secondary must provide a return path for current at its top and bottom, this produces a transverse component (in the direction of motion) to the current in the secondary. These transverse components of current generate their own magnetic fields. Figure 35 gives a representation of how these currents interact with the applied field from the primary.

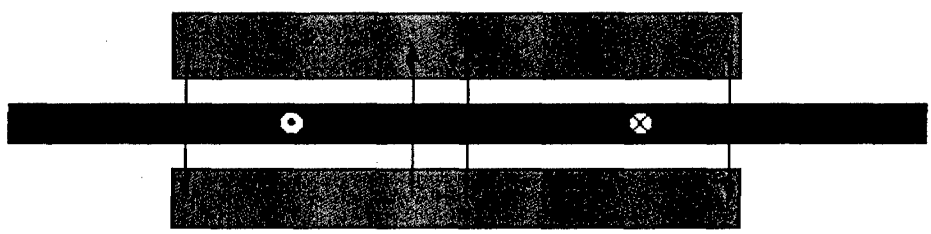

Figure 35 Edge Effect Current's Effect on Transverse Magnetic Field (in negative Z direction)

As can be seen, these edge effect currents create fields that subtract from the applied field in the middle of the secondary and add to the applied field at the ends (or vice-versa). This produces a transverse magnetic field density distribution as seen in Figure 36.

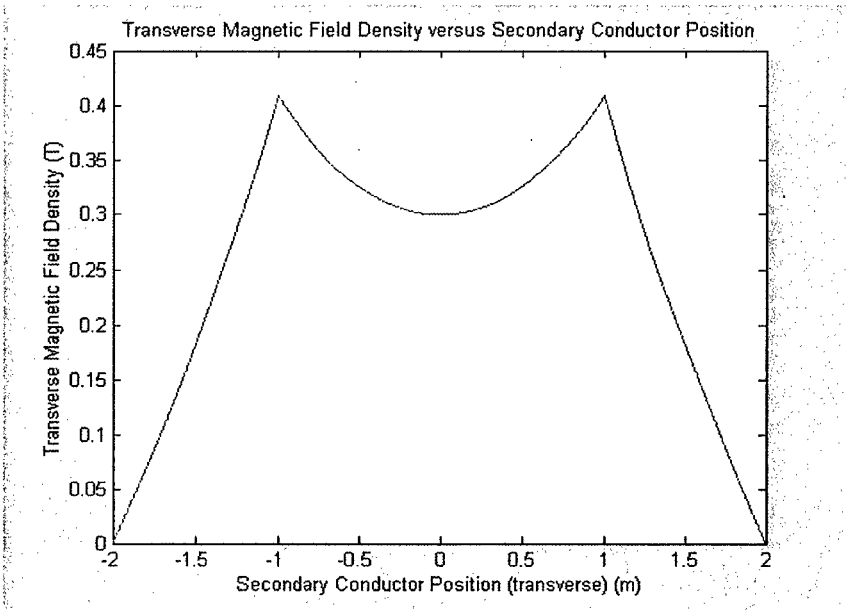

Figure 36 Transverse Magnetic Field Density due to Edge Effect

In this figure, the primary stretches a total of 2 meters from –1 to +1 meters. The secondary stretches a total of 4 meters from –2 meters to +2 meters. The magnetic field peaks at the ends of the primary stack width, and rapidly falls away to zero at the ends of the secondary conductor. The center of the secondary has a local minimum that is a direct result of the induced field created by the transverse components of the secondary current. The formulation of this model is done in Appendix D. The general form of the magnetic field density over the width of the primary stack is [10]:

$$B_y(z) = A + Be^{\alpha \cdot z} + Ce^{-\alpha \cdot z}$$

A, B, C = constants
α = real number

This solution assumes that the primary stack is centered at z = 0.

Intuitively, the influence of the edge effect should decrease with an increase in the secondary width. In the worst case scenario, the secondary would have the same width as the primary stack, and thus all of the transverse current would be under the primary. In the best case scenario, the secondary width would be large compared with that of the primary stack depth, and there would be almost no transverse current component under the primary stack. Boldea and Nasar account for the edge effect by using a correction factor to multiply the secondary resistivity to produce a larger equivalent secondary resistivity [10]. Thus the effect of the transverse current component is to increase secondary resistivity and decrease overall motor efficiency.

3.7 DSLIM Equivalent Circuit

In order to generate a model by which to analyze the DSLIM's power production capability, internal losses and efficiency, an equivalent circuit model must be formulated. This equivalent circuit model takes the same form as that of a conventional electric machine, but certain correction factors are used to account for the peculiarities of the DSLIM. A conventional induction machine circuit model for a single phase of a multi-phase machine is shown in Figure 37. Equations for calculating these equivalent circuit components are located in Appendix E.

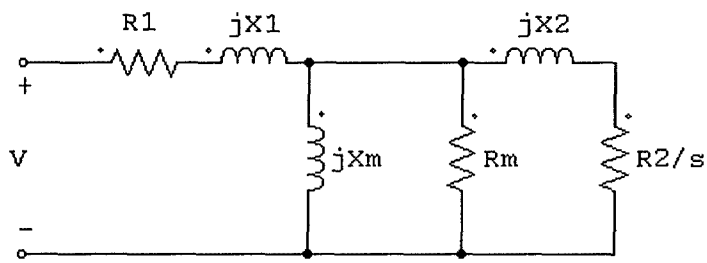

Figure 37 DSLIM Equivalent Circuit

3.7.1 Primary Winding Resistance

The primary winding resistance (R1) is placed in series with the rest of the circuit because the primary windings see all of the applied current. Thus all of the applied primary current will result in resistive heating losses within the primary coils and will need to be accounted for in cooling of the machine.

3.7.2 Primary Leakage Reactance

Likewise, the primary leakage reactance (jX1) is placed in series with the rest of the circuit. All of the primary current produces flux that has the possibility of leaking by without coupling with the shuttle (thus producing no useful work). This leakage reactance represents the fractional amount of flux that does leak by without producing useful work, and as a result causes a greater quadrature component to the primary current. This is how the circuit accounts for leakage flux and the loss of the primary current's capacity to perform useful work.

3.7.3 Magnetizing Reactance

The magnetizing reactance (jXm) is placed in parallel, after the winding resistance and primary leakage reactance, to represent the inductance that links the primary and secondary of the machine.

3.7.4 Magnetizing Resistance

The magnetizing resistance (Rm) is placed in parallel with the magnetizing reactance. This is because the magnetizing resistance loss is proportional to the flux in the machine, which is in turn set up by the applied voltage across the magnetizing reactance. The value of this resistance is largely determined by the lamination of the primary. The best primary laminations (also the most costly) prevent eddy currents to the maximum extent possible by breaking up their flow paths. This has the effect of making Rm very large, and the corresponding resistive heating losses within the primary back iron very small.

3.7.5 Secondary Leakage Reactance

The secondary leakage reactance (jX2) is placed in series with the secondary resistance. In non-sheet type secondarys, where ferrous material is used on the secondary, there are leakage paths within the secondary such that the flux has the capability of bypassing the secondary conductors and therefore producing no useful work. This leakage reactance causes the secondary induced current to have a quadrature component, which contributes to additional resistive heating losses in the secondary, but produces no useful work. Since the DSLIM being considered in this body of work assumes a sheet secondary for weight considerations alone, the secondary leakage reactance for this DSLIM will be zero.

3.7.6 Secondary Resistance

The apparent secondary resistance (R2/s) represents a kind of transformed resistance across the airgap of the machine. This secondary resistance is calculated based on the type of secondary conductor, the primary conductor arrangements (turns and winding factor), the primary stack depth, and the geometry of the shuttle. This secondary resistance is dependent on the speed of the secondary with respect to the primary travelling wave. At a slip of zero, the secondary resistance becomes infinite, which is a reflection of the fact that there would be no induced current in the secondary because there would be no relative motion between the primary field (a travelling wave) and the secondary (shuttle).

3.7.7 Performance Calculations

After the component values of all the aforementioned items have been calculated, the performance of the DSLIM can be calculated on a per-phase basis. These performance characteristics are listed below.

$$P_{input} = V_1 \cdot I_1 \cdot \cos(\phi_1)$$

$$P_{copperloss} = I_1^2 \cdot R_1$$

$$P_{developed} = (1 - s) \cdot \left(V_1 \cdot I_1 \cdot \cos(\phi_1) - I_1^2 \cdot R_1 \right)$$

$$F_{developed} = \frac{1}{V_{shuttle}} \cdot P_{developed}$$

$$P_{copperloss\ (secondary)} = s \cdot \left(V_1 \cdot I_1 \cdot \cos(\phi_1) - I_1^2 \cdot R_1 \right)$$

V_1 = Primary Voltage
I_1 = Primary Current
ϕ_1 = Phase difference between primary voltage and curren
R_1 = Primary Winding Resistance
$V_{shuttle}$ = Velocity of shuttle
s = slip

Thus the performance of the DSLIM can be obtained at various operating points on a per phase basis.

Since the framework of this thesis is optimizing the efficiency of a DSLIM, particularly with regard to EMALS, a method for measuring efficiency must be determined. It could be argued that the overall efficiency would be simply a matter of determining the output power with respect to the input power. This would be a good method for a mass transit system in which the machine could be expected to be in steady state for large portions of time, but not for an aircraft launch system which is always in a state of change. A more appropriate efficiency for an EMALS DSLIM would be energy efficiency. Specifically, the kinetic energy of the load (aircraft) at the end of the linear track would be the output energy. The input energy would be the time integral of the product of the applied voltage and applied current from the beginning of the launch cycle to the end of the launch cycle. Therefore, the efficiency of the EMALS DSLIM should be calculated as below.

$$\eta = \frac{Energy_{out}}{Energy_{in}}$$

$$Energy_{out} = \frac{1}{2} \cdot m_{aircraft} \cdot V_{aircraft}^{2}$$

$$Energy_{in} = \int_{0}^{t_{end}} V_{applied} \cdot I_{applied} \, dt$$

$m_{aircraft}$ = mass of aircraft
$V_{aircraft}$ = Velocity of aircraft at end of launch stroke
$V_{applied}$ = Applied Voltage
$I_{applied}$ = Applied Current
t_{end} = ending time of launch stroke

These efficiency calculations will not include the effects of thrust from the aircraft. All of the energy required to bring the modeled airframes to launch velocity will be assumed to come from the DSLIM. This is a conservative approach, especially when considering aircraft such as the F/A-18, which generates a thrust at afterburner that exceeds its own weight.

THIS PAGE INTENTIONALLY BLANK

Chapter 4

4.0 Induction Machine Motor Drives

4.1 An Introduction to Vector Controls

The term vector control refers to a broad range of controllers that allow variable speed control of AC motors. The technique of vector control for AC variable speed motors has been available from some motor drive manufacturers since the mid-1980s, and has been made possible because of the large strides made in the field of solid-state electronics both with microprocessors and power electronics. For a long time, DC motors and their respective drives were preferable to AC motors and their respective drives due to the degree of controllability that DC motors allow. With torque being directly proportional to the product of the field and the armature current in a DC motor, and with both currents being easily measured and manipulated within the machine, it was easy to build controllers that could set the field current and vary the armature current to enable torque and speed control. AC vector controls are meant to supply that kind of controllability to an AC machine [16].

In an AC induction motor, the flux producing current (Im) and the torque producing current (Ir) cannot be measured externally because, for lack of a better physical description, they are located 'inside' the motor. Because of this, they cannot be measured externally or controlled separately. These two currents are in quadrature with each other, and their vector sum (assuming the magnetizing resistance is large) is the total stator current. The challenge then is to discern the two separate currents from the total stator current, which is the only measurable quantity. A revised circuit model for the DSLIM is located in Figure 38.

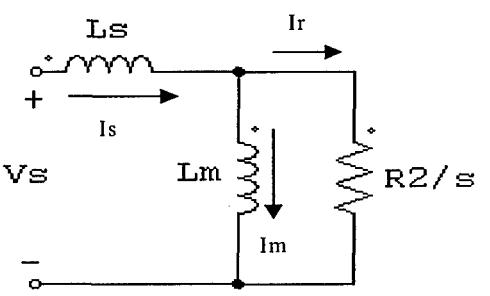

Figure 38 Vector Control Induction Motor Equivalent Circuit

The calculation of the current vectors must be performed by measuring externally available quantities such as stator voltage (Vs), stator current (Is), the phase of the current with respect to voltage, the frequency of the applied current and the speed of the machine and applying these quantities to a motor model. This motor model would have the motor constants such as the leakage inductance, the magnetizing inductance, the secondary resistance, and the winding resistance so that a microprocessor could take the operating point and calculate Im and Ir. These currents would then be used by the microprocessor to calculate how to vary those currents to reach or maintain an operating point [16]. As an example of how this process works, an induction motor is investigated in 3 different load conditions (see Figure 39).

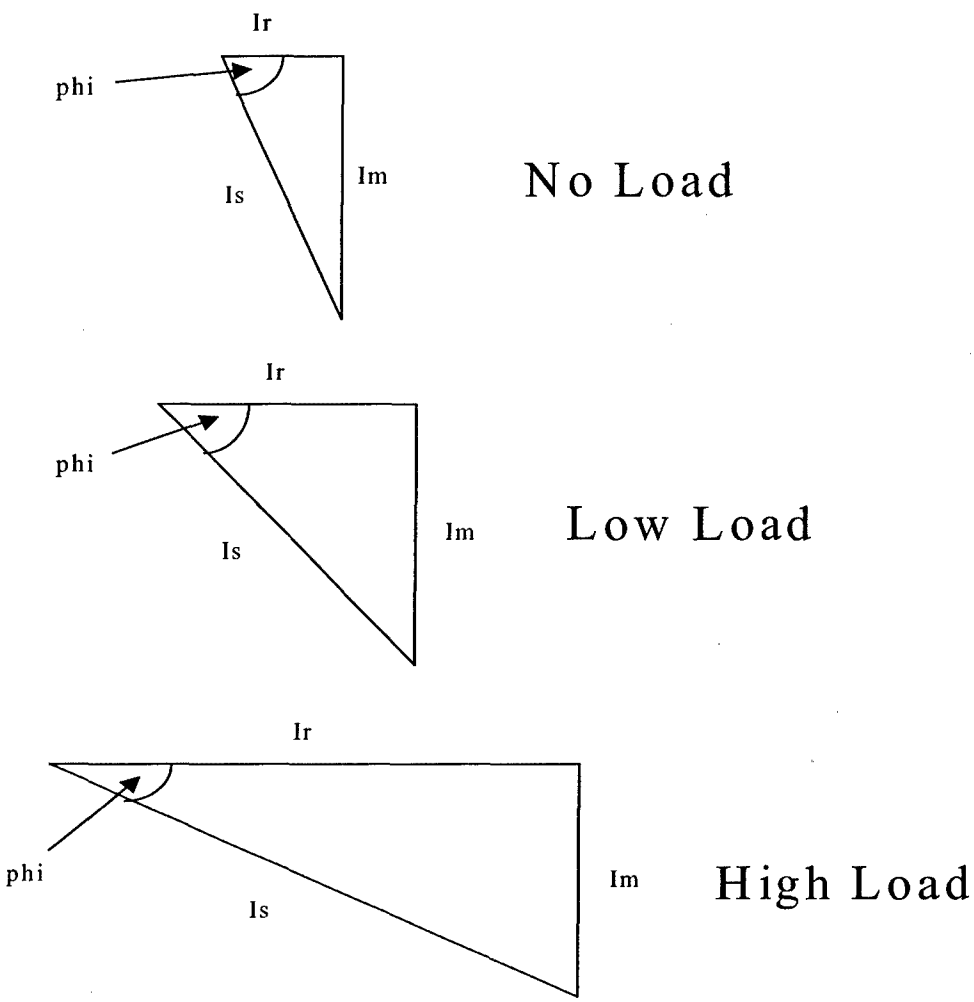

Figure 39 AC Induction Motor Current Vectors

In the no-load condition, slip is nearly zero, and the stator current is almost entirely composed of magnetizing current. The only shuttle current that is needed is that which is required to overcome friction and windage losses within the machine. As a

result, the machine power factor is almost zero because Is will lag Vs by nearly 90 degrees.

In the light-load condition, the magnetizing current is relatively unchanged, while the shuttle current is increased slightly to provide the additional thrust because of the slightly higher slip. The stator current will still lag the stator voltage, but by a slightly smaller angle, and hence the power factor will be slightly higher than the no-load condition.

At the high-load condition, again the magnetizing current is relatively unchanged. However, with a greatly increased slip, the shuttle current is now the dominant current component to the stator current. Stator current still lags stator voltage, but this time at a greatly reduced angle. This causes the power factor of the motor to increase dramatically. In rotary induction motors, the full-load power factor can be in the range of .85.

The central part of the vector control system must therefore be the active motor model. This active motor model is used to continuously model the conditions inside the motor and use these conditions to execute control decisions. It does this by:

- Measuring the Stator current and voltage in each phase
- Measuring the motor speed with an encoder or calculates speed
- Stores the motor constants in memory
- Continuously calculates the flux-producing current
- Controls speed by feedback, feedback is sent to torque control
- Torque control is implemented comparing desired torque to actual torque as calculated by the current and speed measurements

For satisfactory dynamic response of the drive, the model calculations should be performed more than 2000 times per second [16]. This is easily achievable with modern high speed processors, but was not possible just 15 years ago.

4.2 AC Variable Speed Drive Types

Most AC variable speed drives built today employ vector control to some degree. There are essentially 3 basic types of AC variable speed drives currently available [16]:

- Basic fixed Volts/Hertz drive: This drive provides fair speed control and is very reasonably priced
- Volts/Hertz Sensorless Vector Drive: This drive configuration provides better speed regulation, better acceleration, and better starting

torque than fixed volts/hertz because it implements better control of the flux producing current (Im).

- Closed Loop Field Oriented Vector Control: This drive configuration provides the best possible speed and torque control with DC-like performance being advertised.

Each of these drive types implements vector control to a certain extent.

4.2.1 Basic Fixed Volts/Hertz Drives

This is essentially an open-loop control scheme in which the speed reference of the motor, taken from an external source, is used to control the voltage and frequency applied to the motor. In a typical sequence of events, a step change in the speed reference will cause the microprocessor controlling the motor to ramp up the motor's speed by ramping up voltage and frequency. The ratio of the voltage and the frequency is kept constant at all times, hence the term fixed volts/hertz controls. The base voltage and base frequency used for this ratio are taken from the motor's nameplate data, and it is assumed that these values will not cause any flux saturation concerns within the motor over the entire range of operation. There is no speed feedback from the motor (it is an open-loop control scheme), and the motor is assumed to respond to and follow the output frequency of the motor controller. Current feedback is only used for indication and protection, and provides no automated controller response except in the event of an overload condition.

This type of open-loop control is good for controlling steady-state conditions and simple applications that do not require a tight response for speed and torque. Thus this type of controller would not be a good candidate for EMALS, which requires a high degree of responsiveness to control an aircraft as it is accelerated for takeoff. A sample of this type of controller is shown in Figure 40.

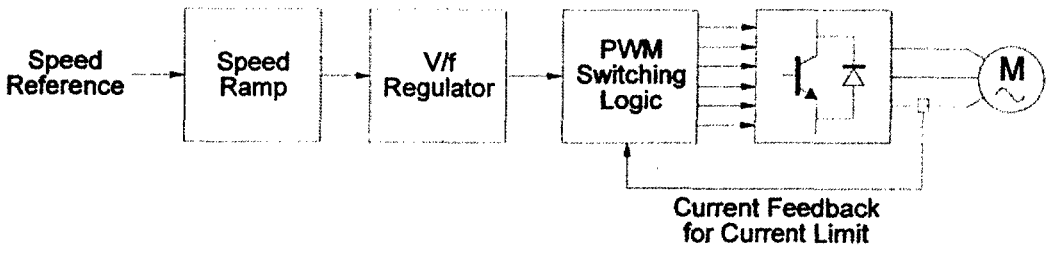

Figure 40 Fixed Volts/Hertz Controller [16]

4.2.2 Volts/Hertz Drives Sensorless Flux-Vector Drives

Sensorless flux-vector drives were developed primarily to overcome the shortcomings of fixed volts/hertz drives in low speed thrust. This type of drive is also called an open-loop vector drive because at its core it is the same fixed volts/hertz open loop controller as before with several improvements:

- A current resolver is included to calculate the two separate current vectors (Im, Ir)
- A current limiter which uses the torque producing current (Ir) to rapidly adjust frequency to limit current
- A flux regulator which adjusts the volts/hertz ratio to maintain an optimum control of the flux-producing current (Im)
- A slip estimator that estimates motor speed based on known motor parameters without the use of an encoder

This control scheme results in greatly improved thrust in the low-speed region of operation, and also gives improved dynamic response [16]. This device does not provide thrust control however. It merely acts to control speed. As such, it is also unsuitable for aircraft launch duty in which the smooth acceleration of an aircraft is of great importance.

4.2.2 Closed-Loop Field Oriented Vector Drives

This type of induction motor control scheme advertises very tight speed control (.01 %) and very good responsiveness (50 radians/sec). This dynamic response is a direct result of the closed loop feedback that is employed, and gives the controller a response that is 10 times better than standard volts/hertz drives [16], [17]. A typical control block diagram for a closed-loop field oriented vector drive controller is located in Figure 41.

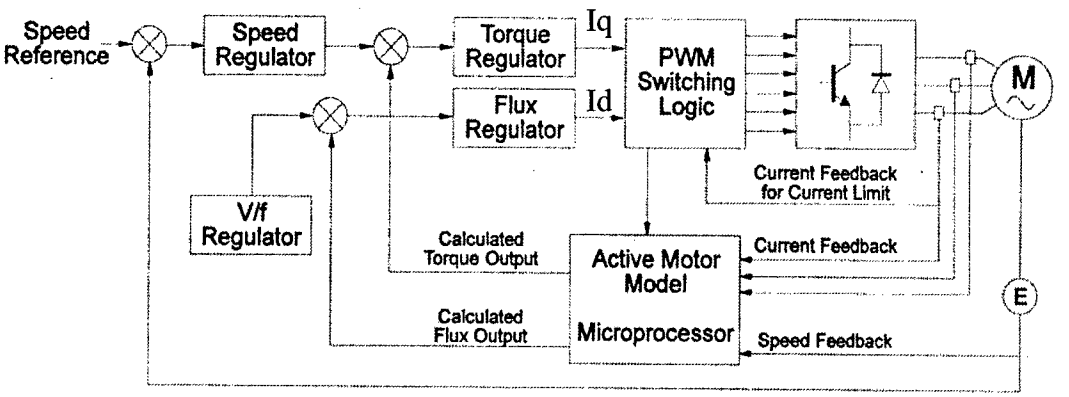

Figure 41 Closed-Loop Field Oriented Vector Drive [16]

As can be seen, there are two separate control loops. One loop is for the control of speed, and the other loop is for the control of current. The speed control loop controls the output frequency, which is proportional to the speed of the motor (slip being the proportionality constant). The torque loop controls the motor in-phase current, which is proportional to torque.

The speed reference command is externally input to this block diagram, but in EMALS, it would most likely be an integral part of the controller. With EMALS, the aircraft will have a launch profile that it must maintain, with it reaching certain speeds at certain points along the track in order to ensure a smooth acceleration and takeoff velocity at the end of the motor track. This speed reference command is compared with the actual speed of the motor (read from an encoder), where it then goes on to the speed regulator. The speed regulator's signal is used as a setpoint for the torque regulator along with the calculated current feedback. These two quantities determine whether the motor is to be accelerated or decelerated. The output from the torque regulator, together with the output from the flux regulator (which ensures voltz/hertz is ensured and saturation conditions do not exist), are fed to the switching logic to determine the firing of the semiconductor switching devices to drive the motor according to the control scheme.

4.3 Implementation of Field Oriented Controls in Induction Machines

Earlier sections have concentrated on the general concepts of field oriented controls of induction machines, but stayed away from the practical implementation challenges of such controls. Field oriented controls strive to give an induction motor the same kind of controllability that is possible with a DC motor. In order to achieve this, a means of measuring and producing direct and quadrature axis currents must be developed. These currents must be used along with machine speed and the machine parameters to determine a course of action to control the machine. All of these items must be performed many times per second in order to attain a high order of dynamic stability.

4.3.1 Direct and Quadrature Axis Current Control

Direct and quadrature axis currents are not readily measurable in an induction motor. This is because they are a mathematical formulation of the individual phase currents of the induction motor meant to aid the measurement and control of the machine. There are only three quantities that are measurable from outside the machine: The individual phase voltages, the individual phase currents, and the speed of the machine

using either an analog tachometer or a digital encoder. With these three quantities, the individual phase quantities can be transformed into their direct and quadrature axis components using Park's Transformation. Park's Transformation, in this case, assumes a rotating coordinate system that is fixed to the direct axis shuttle flux (synchronous frame) of the induction machine [17]. For a three-phase machine, it is:

$$\begin{pmatrix} i_d \\ i_q \\ i_o \end{pmatrix} = \frac{2}{3} \cdot \begin{pmatrix} \cos(\theta) & \cos\left(\theta - \frac{2\cdot\pi}{3}\right) & \cos\left(\theta + \frac{2\cdot\pi}{3}\right) \\ -\sin(\theta) & -\sin\left(\theta - \frac{2\cdot\pi}{3}\right) & -\sin\left(\theta + \frac{2\cdot\pi}{3}\right) \\ \frac{1}{2} & \frac{1}{2} & \frac{1}{2} \end{pmatrix} \cdot \begin{pmatrix} i_A \\ i_B \\ i_C \end{pmatrix}$$

As stated earlier, Park's Transformation uses the individual phase components and combines them into a single in-phase component (direct) and a single out-of-phase component (quadrature). In a balanced three phase system, the individual phase currents sum to zero, therefore there is no zero sequence current. Park's Transformation assumes the shuttle angle is known, and given the fact that we know the shuttle speed (a measurable quantity), we must simply add the shuttle mechanical speed to the slip speed and integrate with respect to time to get the shuttle angle. This angle will provide the flux wave's relative position to that of the physical shuttle itself, and will thus provide a direct indication of where the shuttle flux is. The thrust relation in a linear induction machine is:

$$T_e = \frac{3}{2} \cdot k \cdot \left(\lambda_{dr} \cdot i_{qs} - \lambda_{qr} \cdot i_{ds}\right)$$

Knowing where the shuttle flux is, this position can be established as the new direct axis.

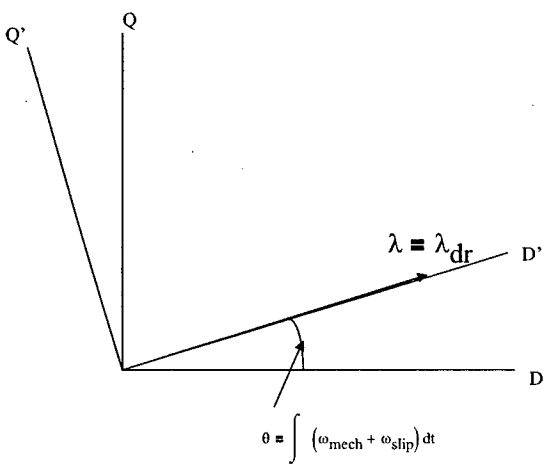

Figure 42 D-Q Axis Transformation

Figure 42 shows this procedure graphically. Thus all of the shuttle flux can be assumed to be on the direct axis, which changes the torque equation to [18]:

$$T_e = \frac{3}{2} \cdot k \left(\lambda_{dr} \cdot i_{qs} \right)$$

Remembering that we can adjust the shuttle direct axis flux by injecting current on the new direct axis, and we can adjust torque by injecting current on the new quadrature axis, a decoupled control is possible. Remembering that these angles are calculated based on a shuttle moving at a certain speed and slip frequency, placing the stator current is a simple matter of magnitude and angle with respect to the new shuttle direct axis (see Figure 43).

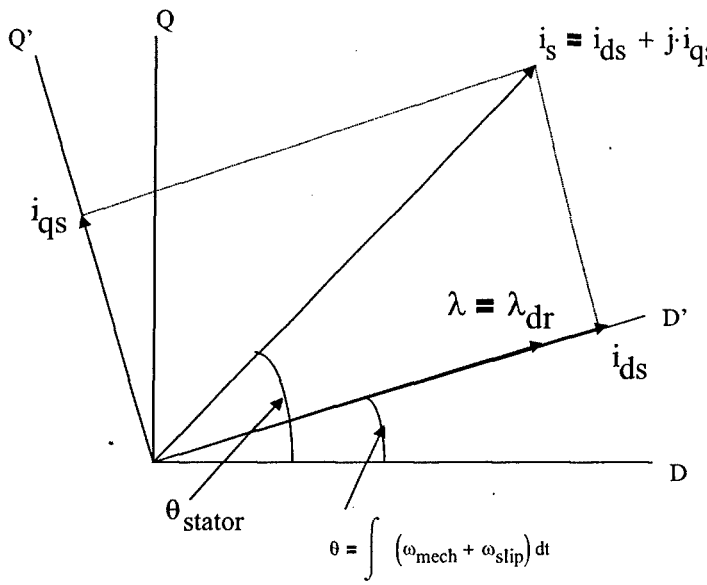

Figure 43 Stator Current Placement

Recognizing that this is a decoupled system, the direct axis stator current is calculated to maintain flux according to the desired speed of the machine (volts/hertz to avoid saturation), and the quadrature axis stator current is calculated based on the requirements of the controller to either speed the machine up or slow it down. The required speed would be passed on to this controller by another microprocessor that would keep track of an aircraft's launch profile. This launch profile would consist of a schedule of speed versus time in order to effect aircraft launch as well as to produce smooth acceleration down the length of the track. All of these calculations are carried out with a microprocessor-based control scheme in which things like the motor parameters and algebraic equations for determining currents are all stored as part of memory. In order to

get an idea of the physical reality of the inside of the machine, Figure 44 shows a diagram representing the shuttle and stator currents (fluxes) in this spatial configuration [17].

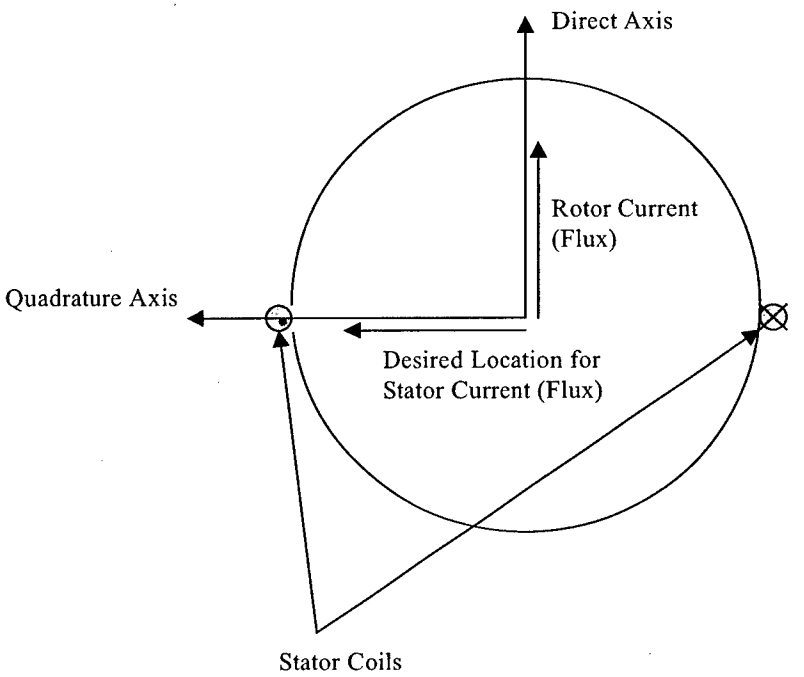

Figure 44 Rotary Induction Motor Physical Layout

In Figure 44, the stator direct axis has already been established on the shuttle direct axis (where the shuttle flux is), and the stator coils which equate to the direct axis of the stator are shown. In order to generate currents on the stator that are in space quadrature with the shuttle, the stator current vector must be spatially displaced from its direct axis in order to have a quadrature component to its current. This spatial angle can be calculated as an increase from that of the shuttle direct axis angle [18]. With a zero increase in shuttle angle, all of the stator current would be placed on the shuttle direct axis, and no torque would be produced. With a 90 degree angle, all of the stator current would be placed on the shuttle quadrature axis. This also would produce no torque because there would be no flux produced. Therefore, for proper operation, direct and quadrature current must be present.

As can plainly be seen in Figure 44, injecting current into the stator in quadrature with the shuttle current will produce the desired results of controllability with respect to torque. The magnitude of this current is calculated by the microprocessor based on the measured versus required speed and thrust limiting concerns. That describes how much quadrature axis current must be provided to the stator. The stator must also be provided with direct axis current as well. Even though, as Figure 44 illustrates, the direct axis

current will not contribute to the torque, it is necessary to supply direct axis current for the flux in the machine. Using a volts/hertz module, and knowing the speed at which the shuttle is traveling, the microprocessor will calculate a voltage to maintain flux within the airgap at a nearly constant level. This is directly analogous to a DC machine in which the field and armature currents produce two fluxes that are orthogonal to each other and one flux is used for the field while the other flux is used for the torque [19].

Now that the microprocessor has calculated the required quadrature and direct axis currents, it must use this to determine what the individual phase currents must be. These phase currents are calculated using an inverse Park's Transformation.

$$\begin{pmatrix} i_A \\ i_B \\ i_C \end{pmatrix} = \begin{pmatrix} \cos(\theta) & -\sin(\theta) & 1 \\ \cos\left(\theta - \frac{2\cdot\pi}{3}\right) & -\sin\left(\theta - \frac{2\cdot\pi}{3}\right) & 1 \\ \cos\left(\theta + \frac{2\cdot\pi}{3}\right) & -\sin\left(\theta + \frac{2\cdot\pi}{3}\right) & 1 \end{pmatrix} \cdot \begin{pmatrix} i_d \\ i_q \\ i_o \end{pmatrix}$$

$$\theta = \theta_{stator}$$

Where the stator (or direct axis shuttle flux) angle is that shown in Figure 43.

The microprocessor now uses these calculated phase currents to develop the firing sequences for the power electronics. It is the power electronics that generate the phase currents for the motor. In a field oriented control scheme, these calculations will go on approximately 2000 times every second [16]. This is to ensure tight control of the motor under all situations, especially highly dynamic situations such as launching an aircraft.

4.3.2 Shuttle Speed and Position Control

As alluded to earlier, induction machine shuttles can be fitted with speed measuring devices such as analog tachometers and digital encoders. These devices allow for position sensing of the shuttle as well using microprocessors for numeric integration. With high-speed sampling, very accurate position calculations can be possible. Depending on the number of poles per unit length in a linear induction machine, combined with the sensed speed of the shuttle, a calculation of the linear velocity of a linear induction machine can be made. This linear velocity would then be used to calculate an angular velocity, which would then be integrated to determine the shuttle angular position. Assuming high-speed sampling is used, a highly accurate determination of shuttle angular position can be made.

With regard to slip frequency in a linear induction motor, the slip speed can be either calculated or measured. With slip speed, and a known pole pitch, a slip frequency is easily calculated. The question is how to determine slip speed.

The most direct method of determining slip speed is measuring the linear shuttle speed and subtracting that from the linear stator speed. The linear stator speed is a function of the applied electrical frequency and the pole pitch. Linear stator speed (synchronous speed) is calculated using the following relation.

$$V_{stator} = \frac{\tau}{\pi} \cdot \omega_{stator}$$

τ = pole pitch (m)

ω_{stator} = stator electrical frequency

Once linear stator speed is known, and the linear shuttle speed has been measured, the linear shuttle speed is subtracted from the linear stator speed, yielding the slip speed. Given the slip speed, the slip frequency is then calculated using the following relation.

$$\omega_{slip} = \frac{\pi}{\tau} \cdot V_{slip}$$

V_{slip} = slip speed (m/s)

This slip frequency is added to the shuttle mechanical frequency and integrated with respect to time to arrive at the shuttle direct axis angle (with a known initial angle).

$$\theta_{rotor} = \int \left(\omega_{mech} + \omega_{slip} \right) dt$$

Thus, direct measurement of the shuttle's speed can be used to calculate the shuttle's direct axis angle, which is used in the control scheme to produce direct and quadrature axis current.

An indirect method of deriving slip speed, and hence slip frequency, is using the motor model to calculate slip speed based on the phase currents. This still requires an initial estimation of the shuttle direct axis angle, and this shuttle direct axis angle estimation must be used and updated at every subsequent sample point in order to calculate slip frequency. Once again assuming that the shuttle direct axis orientation is known, and that all of the shuttle flux is on the shuttle direct axis, the shuttle voltage equations become:

$$0 = \frac{d\lambda_{dr}}{dt} - \omega_{slip} \cdot \lambda_{qr} + R_r \cdot i_{dr}$$

R_r = Rotor Resistance

$$0 = \frac{d\lambda_{qr}}{dt} + \omega_{slip} \cdot \lambda_{dr} + R_r \cdot i_{qr}$$

The shuttle currents can be written as:

$$i_{dr} = \frac{\lambda_{dr}}{L_r} - \frac{M}{L_r} \cdot i_{ds}$$

$$i_{qr} = \frac{\lambda_{qr}}{L_r} - \frac{M}{L_r} \cdot i_{qs}$$

M = Mutual Inductance
L_r = Rotor Inductance

Substituting these into the voltage equations and recognizing that there is no quadrature axis shuttle flux yields:

$$0 = \frac{d\lambda_{dr}}{dt} + R_r \cdot \left(\frac{\lambda_{dr}}{L_r} - \frac{M}{L_r} \cdot i_{ds} \right)$$

$$0 = \omega_{slip} \cdot \lambda_{dr} - R_r \cdot \frac{M}{L_r} \cdot i_{qs}$$

With a bit more algebraic manipulation, this produces [19]:

$$T_R \cdot \frac{d\lambda_{dr}}{dt} + \lambda_{dr} = M \cdot i_{ds}$$

$$\omega_{slip} = \frac{M}{T_R} \cdot \frac{i_{qs}}{\lambda_{dr}}$$

$$T_R = \frac{L_r}{R_r}$$ rotor time constant

Thus slip frequency can be calculated using only the direct and quadrature axis stator currents. These direct and quadrature axis stator currents are in turn calculated from the measured stator phase currents via a Park's Transformation which uses the shuttle direct axis angle estimation from the previous iteration. The shuttle flux linkage is calculated from the applied direct axis stator current. Direct axis stator current is used as a DC quantity in this instance because only the magnitude is important in determining the time required to build up the shuttle flux. Thus, the solution for shuttle flux is:

$$\lambda_r(t) = M \cdot i_{ds} \cdot \left(1 - e^{\frac{-t}{T_r}} \right)$$

Figure 45 shows a schematic of this type of control scheme.

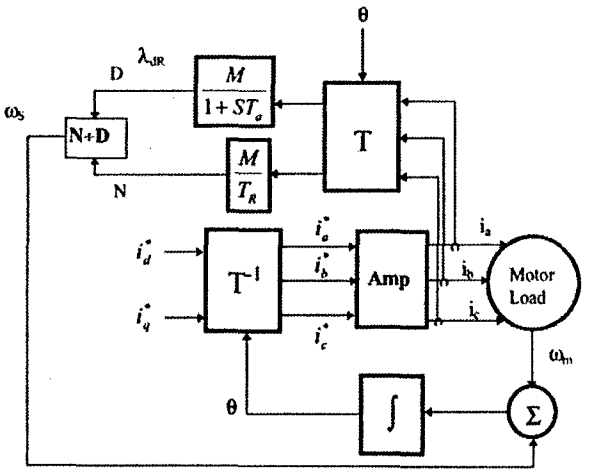

Figure 45 Field Oriented Controller with Slip Calculation [19]

Knowing the shuttle and mutual inductances, an expression for thrust in a DSLIM can be formulated. Recognizing that surface currents are what are being controlled in a field-oriented controller, and assuming that the controller can adequately determine where the shuttle's flux wave is centered, the electromagnetic thrust is calculated as:

$$T_e = \frac{3}{2} \cdot k\left(\lambda_{dr} \cdot i_{qs}\right) \qquad k = \frac{\pi}{\tau}$$

τ = pole pitch (m)
λ_{dr} = direct axis rotor flux
i_{qs} = quadrature axis stator current

Knowing that shuttle direct axis flux can be independently calculated and controlled based on stator direct axis current (which is indirectly measured), the sole variable for thrust production is stator quadrature axis surface current, which can also be independently calculated and controlled. The net result is decoupled flux and thrust control.

4.4 Comparison of Drive Methods

A rudimentary comparison of two induction motor drive methods was performed working under the assumption that each drive method was trying to launch an F-14 Tomcat in a distance of 90 meters. On the low end of controllability, the sensorless volts per hertz controller, and on the high end of controllability, the field-oriented vector controller, were implemented in Simulink using the parameters and fifth order model of a standard (non-linear) induction motor [20]. The assumption was that the linear motor would have a sufficiently long shuttle and a sufficiently large pole pitch to reduce the deleterious effects due to the end effects and leakage flux, and thus the standard induction motor model could be used. The motor parameters used for both simulations were:

$M = 162.6 \cdot 10^{-3}$ — M = Mutual Inductance (H)

$L_S = 6.92 \cdot 10^{-3} + M$ — L_S = Stator Inductance (H)

$L_R = 8.59 \cdot 10^{-3} + M$ — L_R = Rotor Inductance (H)

$R_S = .295$ — R_S = Stator Resistance (ohms)

$R_R = .277$ — R_R = Rotor Resistance (ohms)

$\omega_{base} = 120$ — ω_{base} = Base Frequency (rad/s)

$V_{base} = 14400$ — V_{base} = Base Voltage (Volts)

$\tau = 2$ — τ = pole pitch (m)

The motor parameters above were derived based on launching an F-14 Tomcat, with a launch speed of approximately 67 m/s, in the distance of 90 meters, which is approximately the length of a standard steam catapult. It was assumed in both cases that the motor would be operating in the low-slip region of the torque speed curve, and that the slip would be approximately constant at .1. This slip approximation was used to determine the pole pitch by recognizing that the pole pitch, angular speed, and linear speed were related by:

$.9 \cdot V_{synch} = V_m$ — V_{synch} = linear synchronous speed

$V_{synch} = \frac{\tau}{\pi} \cdot \omega_{synch}$ — V_m = linear mechanical speed

ω_{synch} = rotational synchronous speed

The pole pitch was selected such that the base frequency of the motor would not be excessive. Thus a pole pitch of 2 meters yields a base frequency of 120 rad/sec.

4.4.1 Sensorless Volts/Hertz Control

It was assumed that the controller was designed in such a way as to not cause any deleterious effects on the machine (such as saturation). The base voltage and base frequency were selected to ensure that the aircraft (19777 kg) could make it to takeoff velocity within the required distance of 90 meters. A block diagram of the controller, motor, and linearization model is shown in Figure 46.

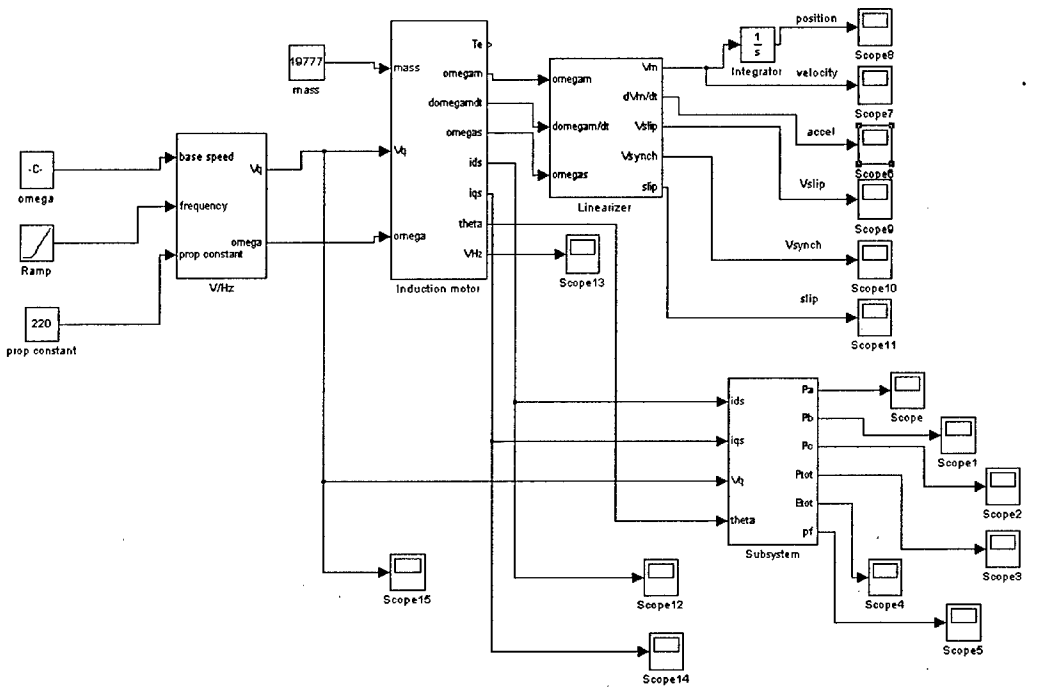

Figure 46 Model Used for Volts/Hz Simulation

Given that the F-14 must take off in the space of 90 meters, and that the acceleration must be nearly constant, the aircraft must have an acceleration of approximately 25 m/s^2 and the total launch will last approximately 3 seconds. The transient is shown in Figure 47.

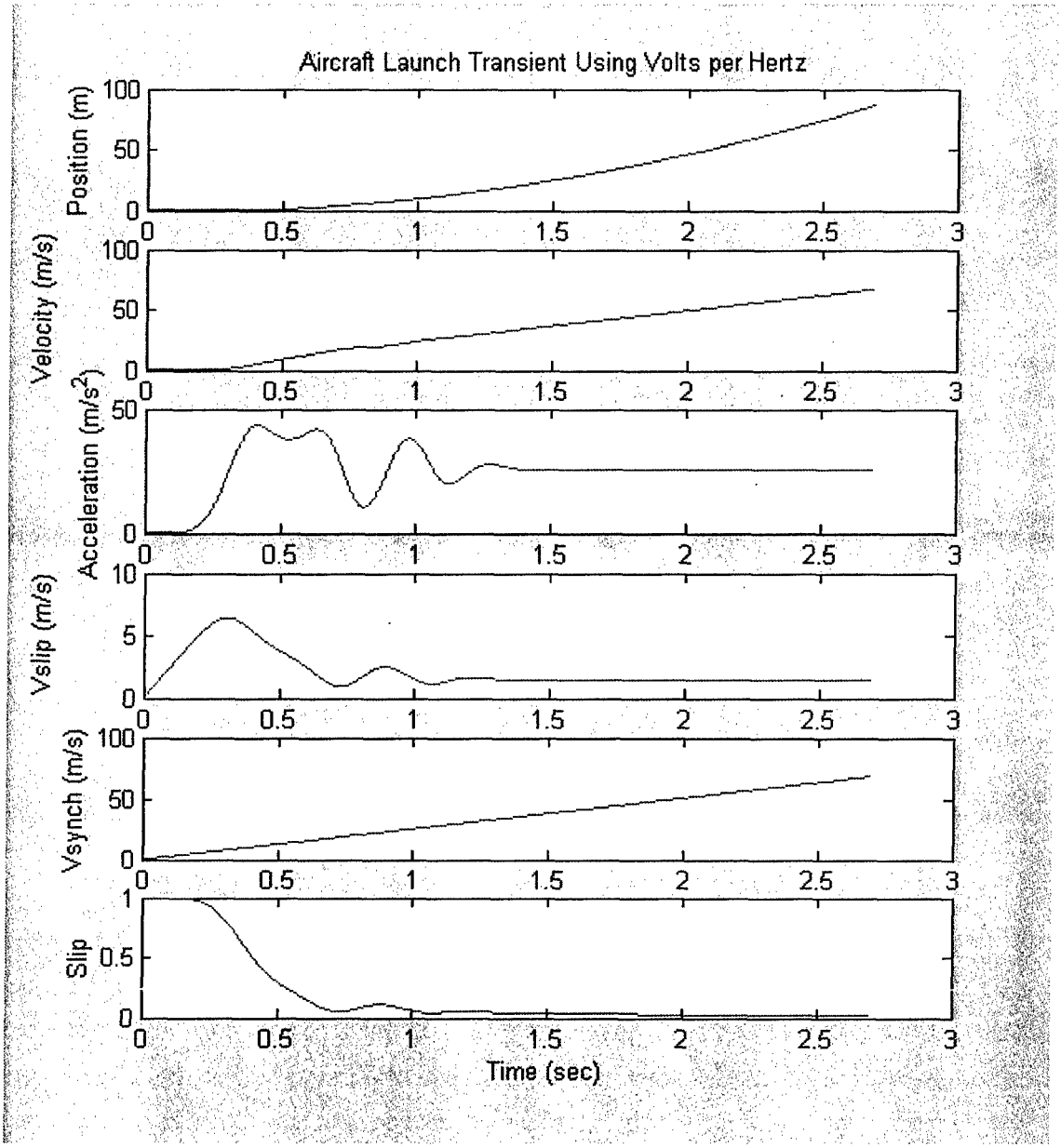

Figure 47 Aircraft Launch Transient using Volts/Hertz Control

After the first second of the transient, the acceleration stabilizes somewhat at approximately 25 m/s^2, at which point the slip has also become somewhat stable. The instabilities at the start of the catapult shot are clearly due to the startup transient. The startup transient was severe because the slip, and therefore the slip frequency, immediately jumped to some finite value and continued to increase with time. It took the DSLIM some time to catch up and create an equilibrium, and this was what happened at approximately the 1 second point. Of course, this startup transient was much more benign than an across-the-line start, and an across-the-line start would never be used for this type of application where a constant acceleration is highly desirable.

It is also interesting to view, for purposes of comparison, how power and energy were delivered in this machine. Figure 48 shows power delivered and total energy consumed versus time.

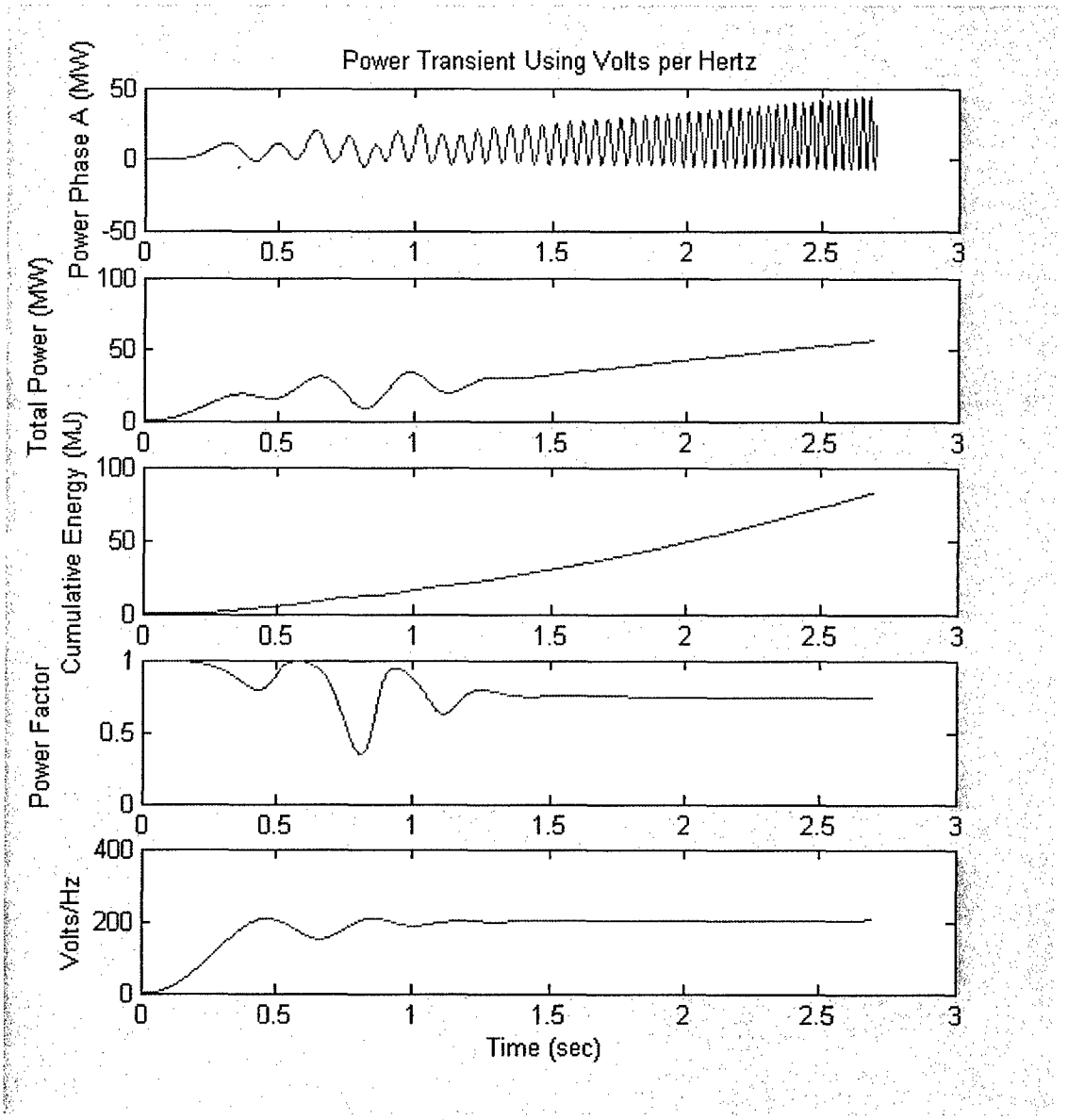

Figure 48 Power and Total Energy Consumption

Of course, the energy delivered to the motor was just the time integral of the power delivered to the motor. Thus, in the launch transient, the EMALS DSLIM consumed approximately 90 million Joules of energy in 3 seconds. In contrast, a 20,000 kg F-14 travelling at approximately 67 m/s at the end of the catapult shot represents approximately 44 million Joules of kinetic energy. Therefore, the efficiency of the energy transfer was approximately 53%. Much of the energy that was lost was lost due to the resistances of the primary and the secondary during the flux build-up, and the power factor of the motor as a whole contributes substantially to resistive heating losses.

It should also be noted that this machine was operating at a higher power factor than can be reasonably expected from a DSLIM. However, this is only meant to serve as an illustration of how well this motor can perform, using volts/hertz, in the transfer of electromagnetic to kinetic energy.

4.4.2 Field Oriented Vector Control

Once again, with this new control scheme, the assumption was made that the motor and controller were designed to be completely compatible. The controller, in block diagram form, is shown below in Figure 49.

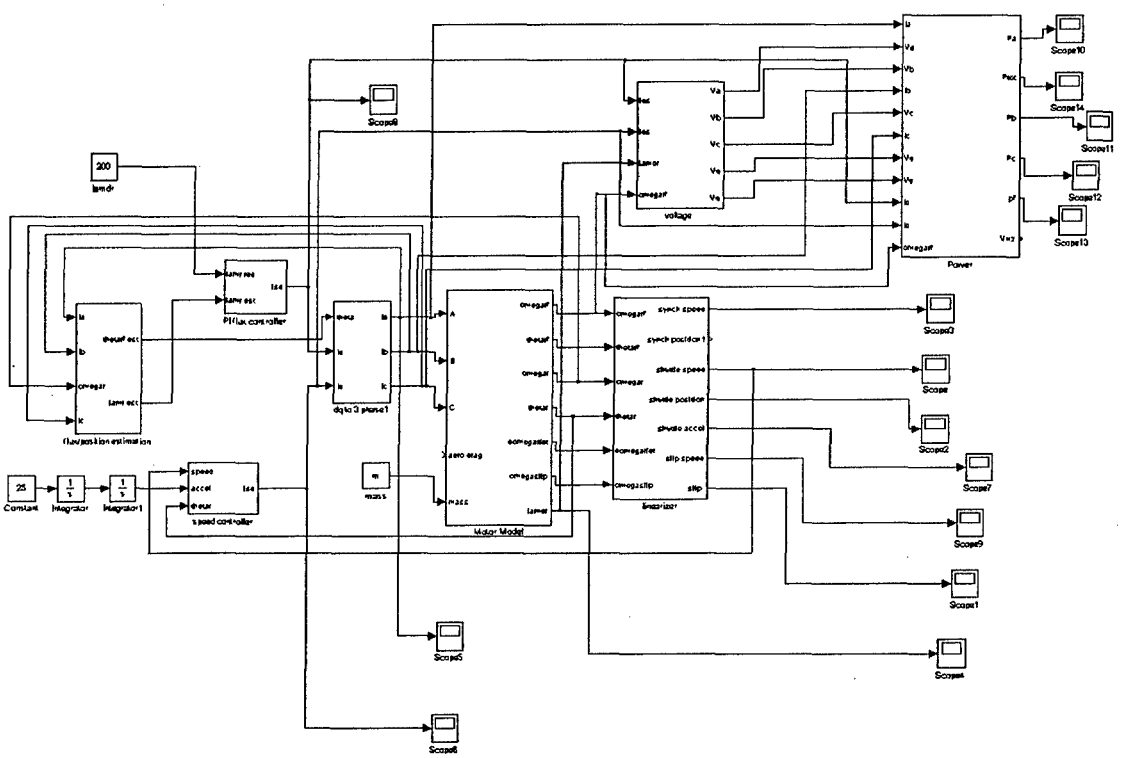

Figure 49 Model Used for Field Oriented Simulation

The above block diagram provides for a nearly constant acceleration while also maintaining a nearly constant d-axis shuttle flux. As before, the acceleration was a constant 25 m/s^2 in order to enable the F-14 Tomcat to reach takeoff velocity at the 90 meter point. The controller measured all three phase currents as well as the shuttle velocity, and used these in a feedback loop to maintain tight control of the launch sequence. The position disparity was calculated based on the expected position given the above constant acceleration and the time integration of the actual shuttle velocity. This position disparity was then used to generate a velocity error, which in turn was sent through a PID controller to generate the necessary q-axis current. The proportional,

integral, and derivative gains for the controller were 100, .1, and 500 respectively, and this produced the response seen in Figure 50.

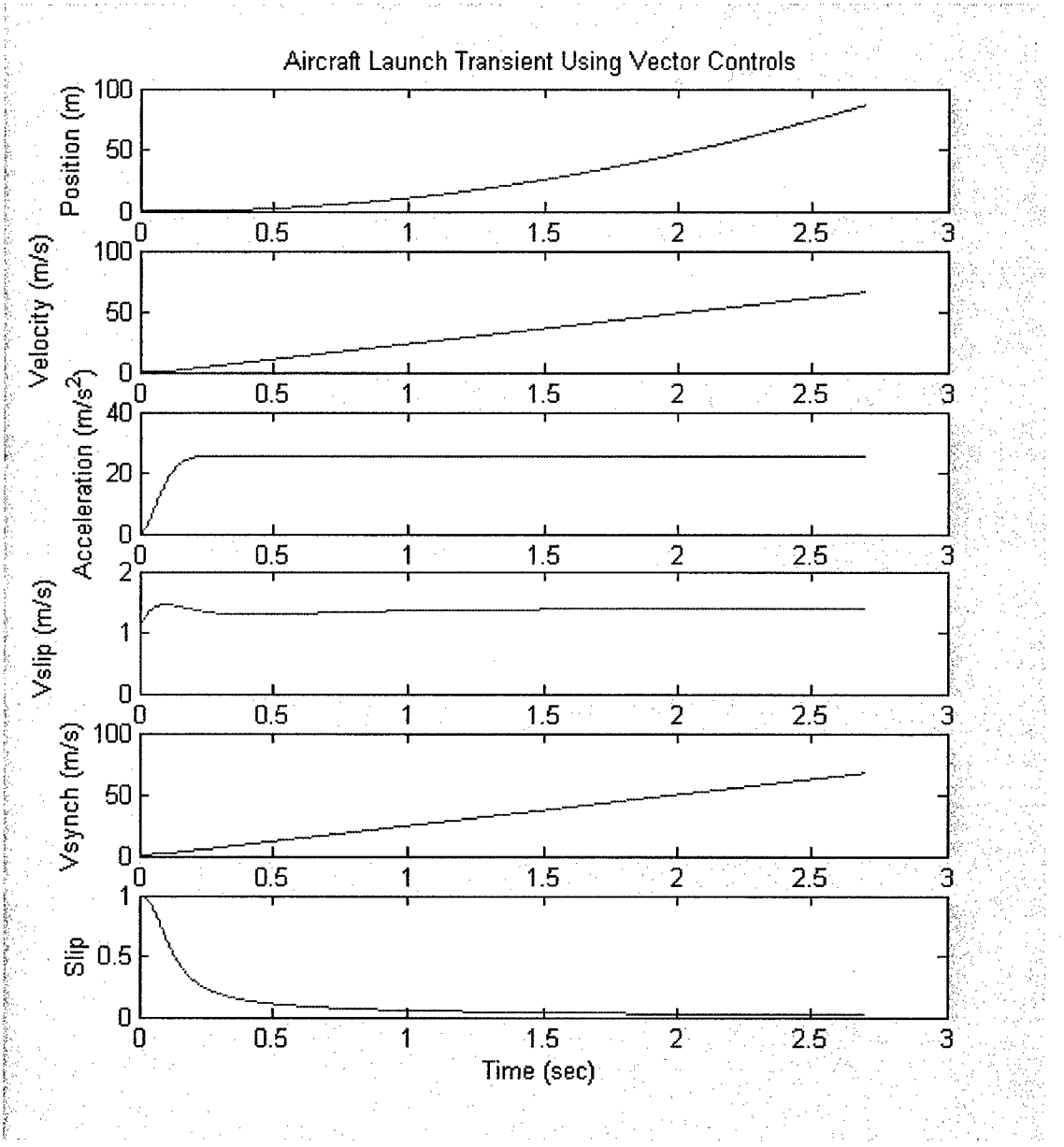

Figure 50 F-14 Catapult Launch Using Field Oriented Controls

Two major items of note are the acceleration profile and slip. As before, in volts per hertz control, the average acceleration was approximately 25 m/s^2. However, the aircraft's acceleration was expeditiously brought to that level in about .25 seconds, and held that level almost perfectly throughout the remainder of the transient. This transient shows a marked improvement from the volts per hertz control in that airframe and aircrew stresses were reduced as a result of the even acceleration.

The power dissipated and the energy consumed by the EMALS were also calculated during the transient, and these results are shown in Figure 51.

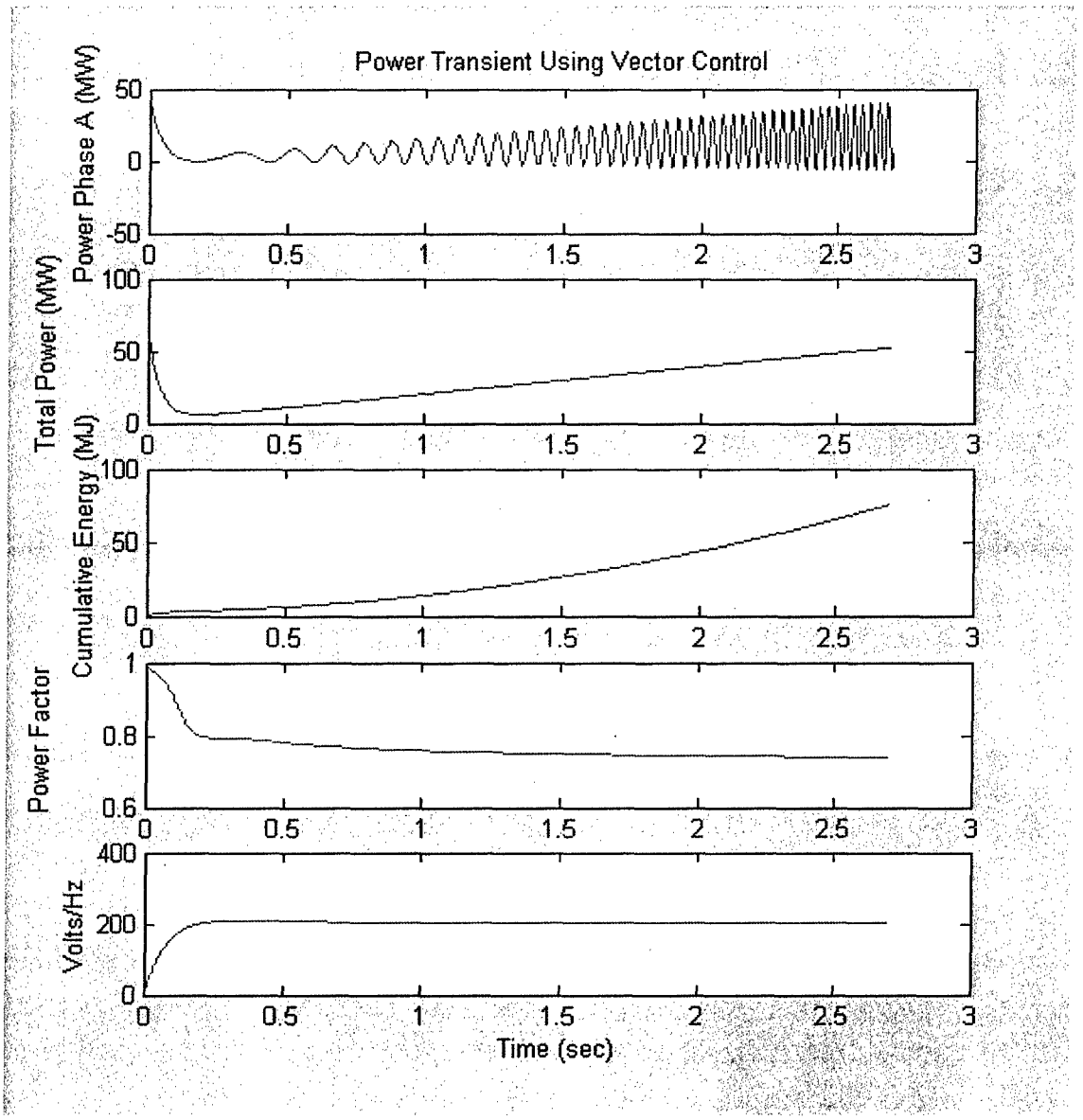

Figure 51 Transient Power and Cumulative Energy in Vector Control

With the previously calculated kinetic energy of an F-14 at takeoff being approximately 44 million Joules, and with this machine having consumed approximately 75 million Joules, the energy efficiency of the system was approximately 59%. This is 6% better than the volts per hertz method of control, and when combined with its controllability, this method is very attractive.

4.5 Controls Method Conclusion

Using exactly the same motor parameters and motor model, field oriented controls represent a better fit for shipboard applications such as EMALS due to their higher efficiency and excellent control capability. In an environment where electrical power generation is limited, a field-oriented controller has very little wasted effort. Both the flux level and the acceleration are rapidly brought up to their required levels, and every

ampere of injected current is used in the most efficient means possible to control the launch sequence. Thus, the argument can be made that this control scheme is the most efficient method possible of controlling the DSLIM. The control of acceleration is highly desirable for the benefits of reduced airframe and aircrew stresses and the assurance that it provides that the aircraft will attain launch velocity by the end of the launch transient. As a point of comparison, conventional steam catapults produce peak-to-mean force ratios of up to 2.0, with averages of 1.25. The peak-to-mean force ratio for this simulated field-oriented controller is less than 1.05, which is the advertised EMALS capability [1]. Additionally, steam catapults are only about 5% efficient [2], [3], which is in stark contrast to the simulated field-oriented control efficiency of 59%. Further investigation into this control scheme will be performed with an actual DSLIM motor model and a more sophisticated controller that will include the effects of saturation within the current source inverter. Detailed block diagrams for the motor and controllers can be found in Appendix F.

THIS PAGE INTENTIONALLY BLANK

Chapter 5

5.0 DSLIM EMALS Design Synthesis

5.1 EMALS Requirements

It was previously established in Chapter 1 that the current US Navy aircraft carrier steam catapult launch system, the C-13-2, was reaching the limit of its useful capability. Larger strike aircraft, such as the F/A-18 E/F Super Hornet, are beginning to have gross weights at takeoff that test the limits of the steam catapult's capacity [2], [3], [4]. This is in addition to the undesirable control scheme of the C-13-2, which employs no feedback. Though fatal catapult system failures are rare, they do occur, and in a system such as the C-13-2, there is no recourse for system failures.

Therefore, in the design of an EMALS system, efficiency, controllability, reliability, and thrust capability should be the primary design considerations. Efficiency and thrust capability are in the domain of the motor design itself, while efficiency, controllability and reliability are in the domain of the motor controller. As stated in chapter 1, the design goal is to get the best efficiency possible, and that will come as a result of the proper motor/controller combination. Of course, these vital parameters must be weighed against a very important shipboard parameter: weight. The back iron of the DSLIM will weigh a considerable amount. Therefore, the most efficient motor design must be carefully considered with respect to the ship's ability to carry such a design.

Patterson states the likely specifications for an EMALS system as follows [13]:

- Maximum LaunchVelocity: 200 Knots, ~100m/s
- Power Stroke: 310 feet, ~100m
- Braking Distance (shuttle): 30 feet, ~10m
- Maximum Kinetic Energy: 120MJ
- Maximum Thrust: 1.29MN
- Maximum Airframe Mass: 26530 kg

According to these numbers, it would appear that no account is being made for engine thrust, which will be a substantial quantity (on the order of 20%). The maximum thrust listed above is a direct calculation from the maximum airframe mass and an assumed acceleration of 5g. Therefore, the only thing accelerating the airframe to takeoff velocity is the catapult. Consequently, this design will also proceed under the conservative assumption that no thrust from the aircraft's engines will be present.

5.2 Preliminary Motor Layout

It has already been established that the motor for the EMALS system must be a DSLIM. However, the general arrangement of this DSLIM has not been proposed. Winding layout, secondary conductor thickness, secondary conductor length, secondary conductor material, primary stack height, and primary winding thickness are the principal characteristics to be decided upon.

5.2.1 Winding Layout, Primary Stack Height and Thickness

While many of the winding types discussed in chapter 3 held significant promise, some can be immediately thrown out. Windings that required slots in the pole face that were only 3 phases and full-pitch are obviously unacceptable due to their spatial modulation of the field. This spatial modulation of the field would cause eddy currents in the secondary conducting sheet, which would result in resistive heating losses in the secondary conducting sheet. These heating losses produce an energy loss, therefore reducing overall motor efficiency.

Recall, however, that with a $5/6^{th}$ pitch winding and a 15-phase source, that the spatial harmonics were reduced considerably (~10% THD). On the basis of reducing spatial harmonics alone, this seems like a reasonable winding layout. However, the complexity of such a design with the winding configuration, the back iron machining, and the semiconductor controls for the excitation of the primary create a development risk as well as a fleet maintenance risk. The more complex a machine becomes, the more difficult it is to teach fleet maintenance people how to repair it. Fleet maintenance personnel are used to working on 3-phase rotary machines. It is likely that a 15-phase machine could create conceptual problems for them.

Laithwaite's diamond coil design is an innovative way of obviating spatial harmonics produced by the field as well as removing end turn losses that plague the former types of winding layouts [14]. With a single turn diamond coil mounted against back iron in a composite matrix, all of the conductors contribute to forward thrust, and there effectively eliminating end turns. This design has two major drawbacks. First, although all of the conductors contribute to forward thrust, they only contribute by a factor of .7071. Second, because the conductors are mounted on top of the back iron rather than in slots, the effective airgap is increased, resulting in higher magnetizing current. There is no published data available for any LIM built in this fashion, and as a

result, the technological risk of designing a motor with this type of winding configuration is deemed unacceptable.

This leaves the Gramme Ring Winding as the design choice. The Gramme Ring Winding has been around for over 100 years, and is effective at obviating spatial harmonics because it is wound directly on top of the back iron. This winding will consist of a number of copper wires (the exact number is determined later) that are wound around the back. Figure 52 shows one side of a Gramme Ring Winding for a DSLIM.

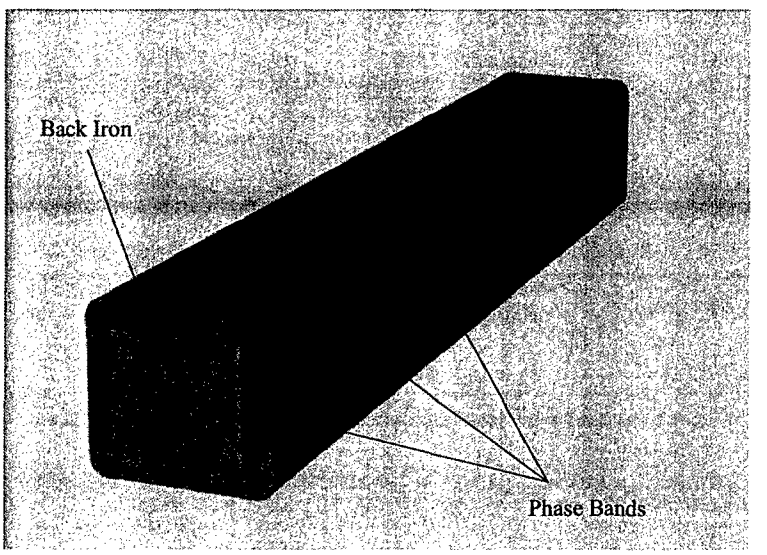

Figure 52 Winding Layout (Gramme Ring)

As discussed in Chapter 3, in order to reduce the leakage flux of the EMALS DSLIM, the track will have to be split up into sections that are activated as the shuttle moves by. The leakage flux results in a large reactive power component to the current (represented in the model as leakage inductance). If the DSLIM were to truly be built like a rotary motor that was cut and the back iron rolled flat, the back iron would be a continuous piece of iron, and all of the armature windings would be activated at the same time. In this unrealistic DSLIM, the armature coils would be continuously covered by the moving shuttle, which would have to be at least twice as long as the stator. Of course, this is not physically possible, especially on an aircraft carrier where space is a premium. Thus, in a real DSLIM, the shuttle will continually cover and uncover stator sections as it moves linearly along its track.

Winding thickness was based on estimates of previous DSLIM designs by Yamamura. Yamamura's DSLIM designs were of the short primary type, but nevertheless were the basis for a short duty cycle winding thickness given the linear current densities he was using. Yamamura was using winding thicknesses on the order of

1 cm for current densities of approximately 65,000 A/m [6]. Based on this, the EMALS DSLIM, which will have higher current densities over short durations, was assumed to have a winding thickness of 2 cm.

Primary stack height was limited to 1 m. This was based on being able to mount the motor completely within a single deck height and allowing room above and below for maintenance access and deck structural members. Given an average deck height on the O3 level of about 8 feet (not including structural members and other overhead items), this allows for a total of 5 feet above and below the motor.

5.2.2 Secondary Conducting Sheet

For better flux coupling, many have argued that back iron should be added to the secondary conductor of a LIM. The layout is like that of a squirrel cage induction motor in that the secondary conductor is laid in strips into the laminated secondary back iron, with end caps on the top and bottom of the conducting sheet to complete the secondary current path. However, using iron in any form in the secondary drastically increases the mass of the secondary. This mass would have to be accelerated along with the aircraft as well as stopped, and as such would use additional energy. It has been noted that adding iron to the secondary does not appreciably increase flux coupling in the motor, and therefore this concept was discarded [9].

Aluminum, with its light weight and good conductivity, was the obvious choice for the secondary conducting sheet. A realistic shear stress for a motor of this type is on the order of 100 kN/m^2 [12]. Given the primary stack height is limited to no more than 1 m of active height, and that the peak force will be 1.29 MN, this requires that the secondary conducting sheet be no less than 5 m long. Of course, the conducting sheet must be extended above and below the active primary area to minimize transverse edge effects. For this design, the secondary will extend .25 m above and below the active portion of the primary stack.

5.2.3 Preliminary Motor Layout Summary

The preliminary motor layout is shown below in Figure 53 with most of the

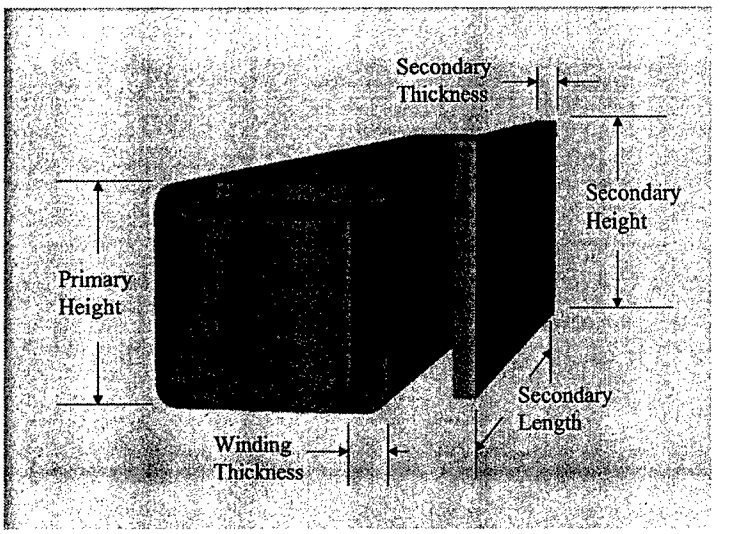

Figure 53 Preliminary Motor Design Parameters

critical aspects labeled. For clarity, only one side of the primary is shown. Figure 54 shows a different view of the same motor with the addition of the second side of the primary to the picture. With the second side of the primary, a true picture of the constituents of the airgap appears. In order to account for contraction of the deck and the possible lateral deflection of the shuttle in a magnetic field that will not be perfectly balanced, the air-filled portion of the airgap will be initially set at 3 cm, 1.5 cm on either side of the secondary. When this is added to the 2 cm of conductor on either side, and the thickness of the secondary (set initially at 2 cm), the magnetic airgap becomes approximately 9 cm. This is in stark contrast to the airgaps of rotary induction motors, which are on the order of millimeters.

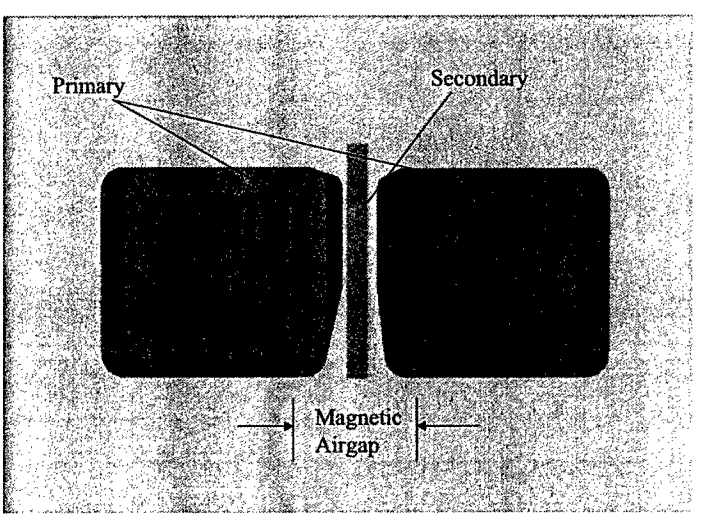

Figure 54 Magnetic Airgap Illustration

5.3 Preliminary Motor Operational Parameters

Now that some of the preliminary motor layout work has been completed, some of the key operational parameters will be identified and calculated. Items such as pole pitch, operating frequency, linear current density, back iron weight and heat dissipation are all important parameters that depend on each other. Recognizing that pole pitch and operating frequency are related by the maximum linear velocity that the aircraft must achieve (104 m/s) through slip, these parameters may be calculated directly given any pole pitch. Many advocate that a larger pole pitch results in a greater net power transfer, and hence greater efficiency [9], [10], [14]. This is a direct result of Laithwaite's Goodness Factor, which shows that real power transfer to the airgap (shuttle) increases with pole pitch. In fact, the Goodness Factor increases as the square of the pole pitch. Unfortunately, the weight of the motor also increases with pole pitch. Figure 55 is an illustration of the total weight of a possible DSLIM configuration as pole pitch is increased.

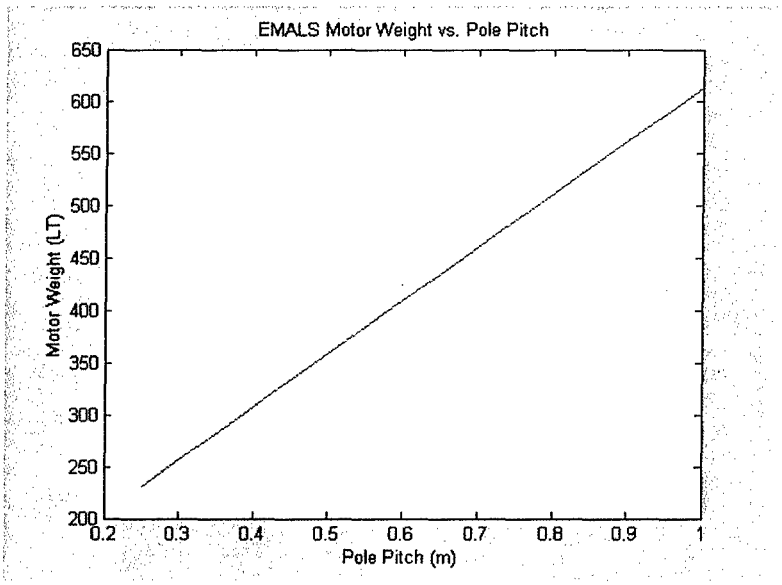

Figure 55 Motor Weight vs. Pole Pitch

This weight is based on the weight of the back iron and copper windings as well as a 4 LT energy storage device and a 20 LT design margin (for power electronics, transformers) [21]. As pole pitch increases, the total weight becomes dominated by the back iron weight. The weight of the current steam catapult system, the C-13-2, is approximately 464 LT [22]. Thus, to prevent any increase in the center of gravity of the ship (and hence a reduction in the stability of the ship), the pole pitch will be kept to .75 meters or less.

In chapter 3, the end effect phenomenon was dealt with as it related to the reduction of a short secondary DSLIM's force output. This issue is now re-visited to determine if it will be a problem with the preliminary motor geometry that is under consideration. Because the shuttle will be no less than 5 m long, and because the largest pole pitch will be .7 meters long, the worst case scenario will be with the shuttle being approximately 7 poles in length. To determine if the end effect is a primary effect under these conditions, The DSLIM model with end effect is run again to produce normalized torque slip curves illustrating the thrust production with and without end effect (Figure 56).

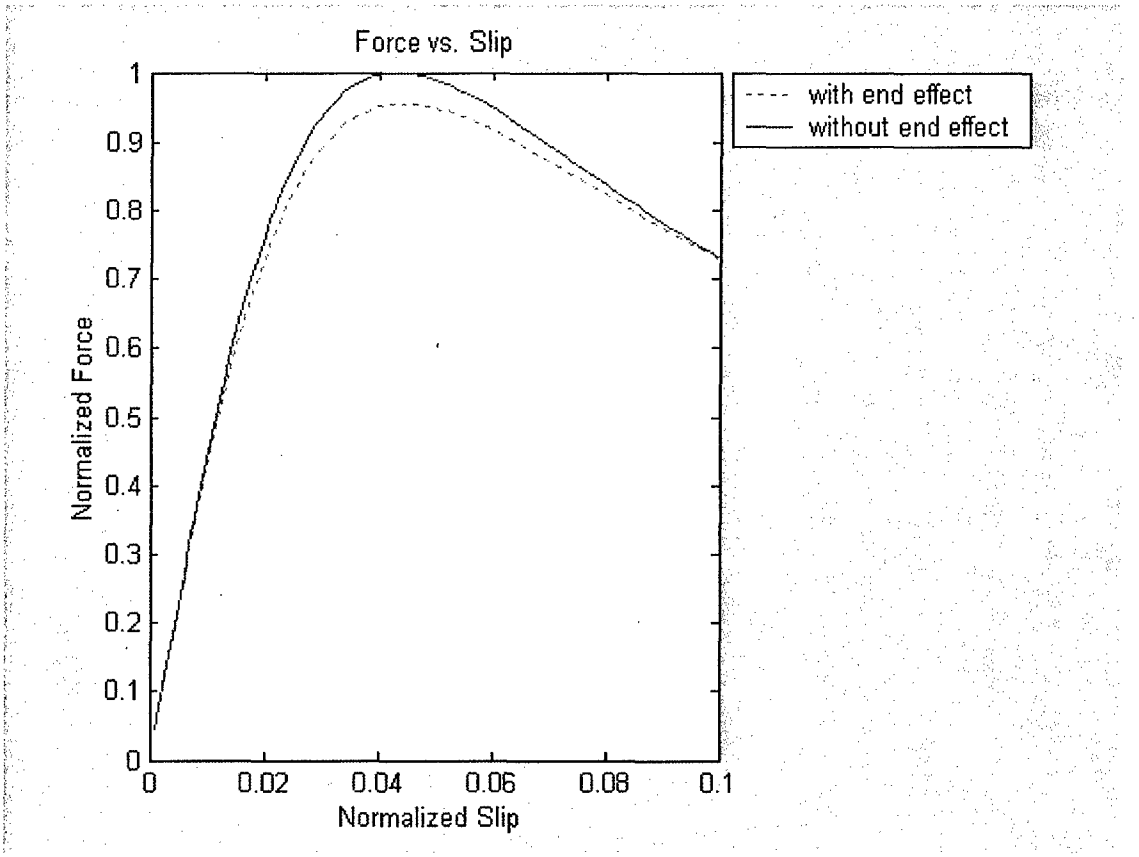

Figure 56 DSLIM Normalized Thrust Slip Curves

The 2 curves track well with each other, with no more than a 5% difference at the worst operating point. Although the DSLIM will operate at different slips (depending on the mass of the aircraft and the required acceleration), it is expected that it will operate in the .02-.05 per unit slip region. Given the fact that only a 5% disparity exists, the end effect model will not be used. Instead, a conventional induction machine equivalent circuit model will be used to calculate the operational performance of different machines with a factor of .95 applied to the thrust calculation. Pole pitch, depth of the primary stack, number of primary turns, rotor length, rotor thickness, and magnetic airgap will be

varied to determine which combination of parameters will give the most efficient operating point. The operating point that will be chosen is the 1.29 MN operating point (maximum thrust) with a 5% margin for peak to mean thrust deviation and a further 5% design margin for other anomalies. Thus, the operating point that is being designed to is 1.43 MN.

Induction machines tend to have their highest efficiencies at low per unit slip. Thus, it is beneficial to move the peak thrust of the DSLIM as far to the right as possible in order to reap the reward of an efficient operating point at maximum thrust. This point is illustrated in Figure 57.

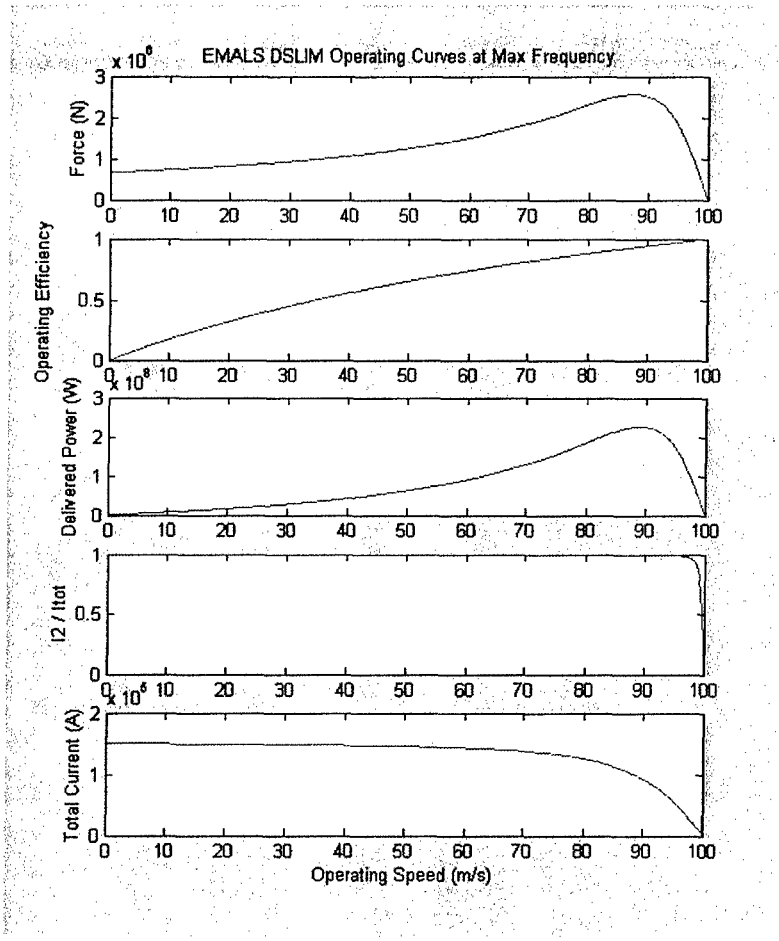

Figure 57 DSLIM Operating Parameters vs. Speed

This hypothetical motor's operating efficiency is nearly 90% at peak thrust. The motor also happens to be producing maximum power at the maximum thrust point. Also of note is the fact that, for lighter loads, the operating point will shift to the right, and the efficiency will increase.

It has been established already that a Volts per Hertz controller with no feedback is a poor method of control for the DSLIM as an EMALS. However, to illustrate a point

as to how the motor will react to accelerating a load from zero to takeoff velocity, the above DSLIM is run again in a variable frequency drive configuration. The operation of the DSLIM is swept from stopped to full speed in 10 m/s increments (Figure 58). Of particular note is the fact that the thrust decreases somewhat at lower speeds, but not by more than 10% (except for the first 2 increments when acceleration is ramping up). Thus, the motor has the capacity to accelerate its load at a nearly constant slip throughout the launch transient.

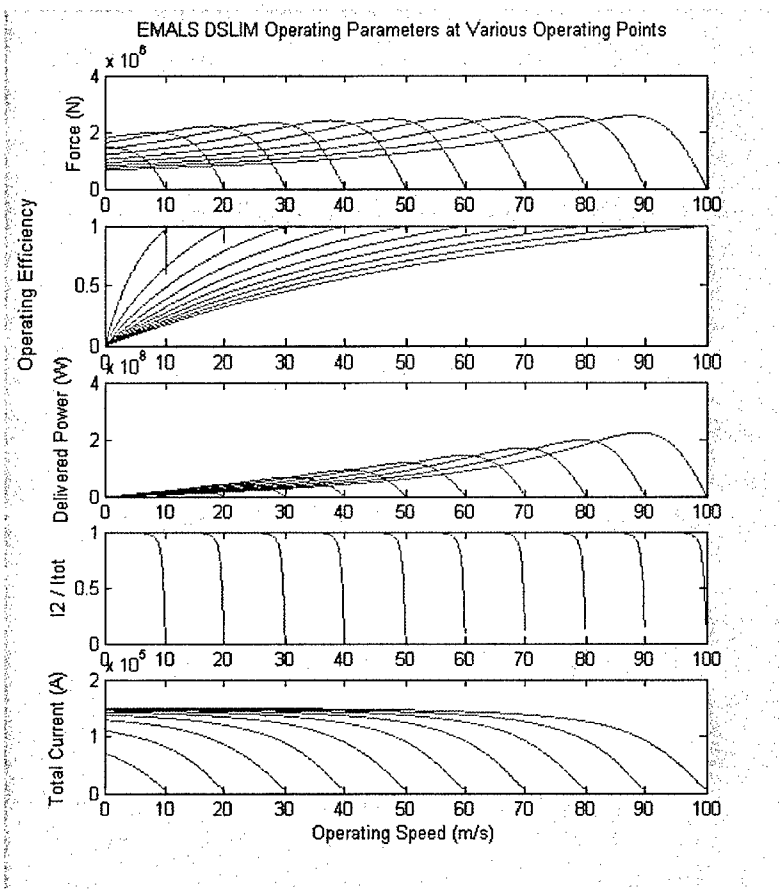

Figure 58 Operating Parameters during Acceleration

Also note that the operating efficiency for each curve is very high in the low slip region. Thus, during the acceleration transient, it is expected that the motor's efficiency will be quite high with the utilization of a vector controller.

With the above background in mind, several Matlab functions were generated to cover the design space of the possible motor configurations. Pole pitch was varied from .25 to .75 meters, primary stack height was varied from .5 to 1.0 meters, the rotor length was varied from 5 to 10 meters, and the number of turns was varied from 1 to 5. Inductance calculations were made with a 20% allowance for leakage flux (due to flux fringing), and thus the total stator flux was multiplied by 1.2 for motor sizing

considerations. Calculations for all motor parameters are located in Appendix G. The Matlab functions first determined if the DSLIM was capable of producing the 1.43 MN peak force. If the DSLIM had the capability, then all of the operating parameters for the 1.3 MN operating point were calculated, including slip and efficiency. After covering the entire design space, the Matlab code then selected the motor configuration with the highest operating efficiency. The motor configuration and operating parameters for the motor with the best operating efficiency (.79) are located in Table 1.

Table 1 Motor Operating Parameters

DSLIM Motor Parameters					
Magnetic Airgap	9	cm	**Shuttle Length**	9	m
Pole Pitch	0.385	m	**Shuttle Thickness**	2	cm
Primary Surface Current Density	291,000	A/m	**Shuttle Height**	1.04	m
Primary Stack Height	0.45	m	**Shuttle Material**	Al	
Primary Stack Width	0.11	m	**Maximum Operating Frequency**	136	Hz
Primary Turns (Per Phase/Per Side)	3	turns	**Weight**	138	tonnes
Primary Packing Factor	0.3		**Winding Thickness (Either Side)**	2	cm
Primary Current	12,460	Amps (RMS)	**Phase Belt Current Density**	14.6	MA/m^2
Primary Voltage	9,257	Volts (RMS)	**Maximum Delta T**	1.1	C
Active Stator Sections	3		**Operating Slip**	0.05	
Total Stator Sections	26		**Power Factor**	0.49	
Track Length	100	m	**Space Between Sections**	2	cm
Poles Per Section	10		**Section Length**	3.85	m

The motor sizing program, the various functions that it calls, and the Mathcad motor sizing worksheet are all located in Appendix G.

The motor was further examined via FEMMVIEW, a two-dimensional finite element program, to validate the flux density in the airgap as well as in the back iron of the motor. Figure 59 illustrates the flux distribution with phase A at its maximum. Thus, the back iron flux density is a maximum in the iron directly behind the phase A conducting band. In this area of maximum flux density, Figure 59 illustrates that the back iron flux density peaks out at approximately 1.8 T, which is the maximum flux density that the back iron can handle without saturating [23]. Figure 59 also illustrates that the airgap flux density reaches a peak of approximately 1 T. Both the Matlab model and the Mathcad model of the DSLIM predicted these values.

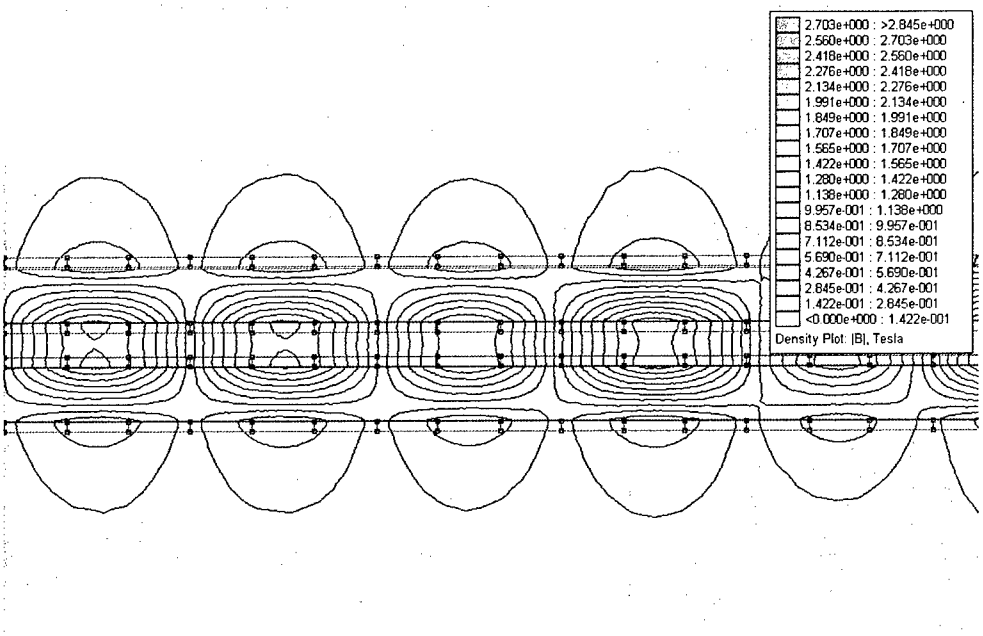

Figure 59 Graphic of Back Iron Flux Density

5.4 Calculation of the Per Phase Equivalent Circuit

As discussed earlier, the motor model can be described as an equivalent circuit to the voltage source. The previous section calculated inductances and resistances within Matlab based on machine parameters. This section will discuss the calculation of the resistances, and will use finite elements to arrive at a better calculation of leakage inductance. The equivalent circuit model is shown below in Figure 60.

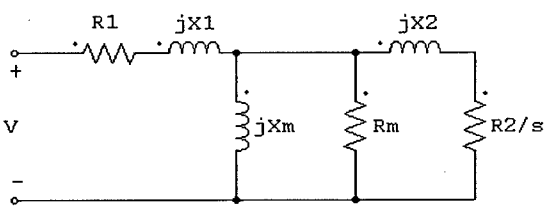

Figure 60 Per Phase Induction Machine Equivalent Circuit

Since the secondary is a sheet conductor, the secondary leakage inductance was assumed to be zero. Also, because laminations were used on the primary, the magnetizing resistance was not calculated for the circuit model (losses were accounted for by using the manufacturer's guidelines [23]). Thus, the only parameters that required calculation were the leakage inductance, magnetizing inductance, stator resistance, and shuttle resistance. In a conventional rotary induction machine, the magnetizing (or mutual) inductance tends to be 30 times that of the leakage inductance while the airgap

tends to be at least 10 times smaller than that of a DSLIM. Thus, we would expect that for a DSLIM, the leakage inductance would be somewhat larger compared to the magnetizing inductance. Because the total stator inductance is a sum of the magnetizing and leakage inductances, the stator inductance was calculated first, and the two constituent inductances were separated.

5.4.1 Stator Leakage Inductance and Magnetizing Inductance

FEMMVIEW was once again utilized to determine the total inductance of the active portion of the machine. Coils in phase A only were energized, and the integral of the magnetic vector potential times the current density was taken along the active sections. This produced a total inductance of 1.7 mH (calculated 1.6 by Mathcad with a 20% fringing effect). This inductance of 1.7 mH is actually a sum of the mutual inductance and the stator leakage inductance (as alluded to earlier). Knowing the geometry of the machine (pole pitch, depth of the primary stack), a hand calculation was performed to determine the mutual inductance. The difference between the two inductances was then the stator leakage inductance (since shuttle leakage inductance is zero). The mutual inductance was calculated to be 1.0 mH, which means the stator leakage inductance was 0.7 mH. As can be seen, the geometry of the short secondary DSLIM has a profound effect on flux leakage, and thus leakage inductance. The mutual inductance is no larger than the leakage inductance, which means the machine's power factor is likely to be low.

5.4.2 Stator Resistance

Stator resistance was calculated in a very straightforward manner as discussed in chapter 3. The total length of the stator wires was calculated based on the perimeter of the back iron and the number of turns in each phase belt as well as accounting for end turn lengths and transmission lengths. Then, this value was divided by the product of the conductivity of Copper and the cross sectional area of the copper conductors. To this was added the effective on-state resistances of the semi-conductor switching devices. Semiconductor switches that are capable of switching 11 kA are not made. Therefore, 7 of the 2 kA bi-directional Silicon Controlled Rectifiers (SCR) in parallel were assumed to be switching track sections on or off as the shuttle went by [24]. Since all of these track sections are in series (in order to limit phase imbalances), the total stator resistance is a sum of the 4 active stator section resistances and the semiconductor and transmission

losses of the remaining stator sections that are bypassed or de-energized. The total stator resistance was determined to be .025 ohms.

5.4.3 Shuttle Resistance

Shuttle resistance was calculated using the method discussed in chapter 3 [11]. This produced a virtual rotor (shuttle) resistance of .019 ohms. This resistance takes into effect the transverse edge effect, the number of primary turns (6 total per pole per phase), the half-thickness of the shuttle, and the pole pitch. This value was multiplied by 2 because of the 2 sides of the DSLIM.

5.4.4 Shuttle Linked Flux

This key parameter is included in the circuit description because it is set by the field-oriented controller as a constant. It is calculated assuming an airgap flux density of 1 T, and it is based on the total area that the shuttle presents to the airgap flux. The more flux that the shuttle links, the higher the traction possible on the shuttle. Based on a shuttle length of 9 m, a primary stack depth of .45 m, and a pole pitch of .385 m, the total linked flux was calculated to be 4.767 Webers.

5.5 Summary

It is important to note that the efficiency for the selected DSLIM is a steady-state operating point efficiency, and does not take into account transient behavior. This transient behavior will be looked at more closely in chapter 6, where aerodynamic drag will also be accounted for. The true measure of the efficiency of the EMALS is how efficiently it can transfer electromagnetic energy to kinetic energy. Chapter 6 will be concerned with the transient energy efficiency of the machine.

While this DSLIM gives a theoretical maximum operating efficiency of .79, the shuttle experiences a 63 C temperature rise during the maximum effort launch transient using a highly conservative estimate of an adiabatic heat transfer. It is highly unlikely, given a wind over deck and other loss mechanisms, that this temperature rise will occur. However, there is no doubt that a means of cooling the shuttle after each shot should be designed. This problem has been addressed before, with different means of attacking the problem [25]. The analysis will continue under the assumption that the temperature rise of the shuttle can be managed.

The motor has now been amply described to begin simulation. The Mathcad spreadsheet, which describes the operating point of the DSLIM in more detail, is located in Appendix G. The motor parameters needed for simulation are listed below.

Design Summary

$R_1 = 0.025\Omega$

$R_2 = 0.019\Omega$

$L_1 = 7.069\times 10^{-4}\,H$

$M = 1.001\times 10^{-3}\,H$

$Stress = 1.466\times 10^{5}\,Pa$

$depth = 0.45m$

$width = 0.11m$

$thickness_{rotor} = 0.02m$

$Voltage = 9.257\times 10^{3}\,V$

$current = 1.246\times 10^{4}\,A$

$flux_{rotor} = 4.767Wb$

$Efficiency = 0.795$

$B_{airgappeak} = 0.997T$

$B_{backironpeak} = 1.744T$

$rotorlength = 9m$

$height_{rotor} = 1.04m$

Chapter 6

6.0 EMALS Motor Model Simulation

6.1 Motor Model for Field-Oriented Simulation

Chapter 5 has produced a motor model for a DSLIM that will be subsequently used in this chapter to determine the motor's overall energy efficiency. Realizing that the motor's efficiency will be lowest during the maximum effort launch transient, it is the maximum effort launch transient that will be simulated. The motor model and significant airframe parameters are shown below.

Transient Model for EMALS DSLIM

$L_{stator} := L_1 + M$ $\quad L_{stator} = 1.708\times 10^{-3}\,H$

$L_{rotor} := M$ $\quad L_{rotor} = 1.001\times 10^{-3}\,H$

$R_s := R_1$ $\quad R_s = 0.025\Omega$

$R_r := R_2$ $\quad R_r = 0.019\Omega$

$flux_{rotor} = 4.767Wb$ $\quad mass := 24000kg$

$\tau = 0.385m$ $\quad acceleration := 53\frac{m}{s^2}$

$C_{drag} := .043$

The field-oriented control model has also been improved to account for harmonic losses and iron core losses as well as aerodynamic drag. The harmonic losses are based on a Total Harmonic Distortion (THD) of the applied current of 10%, while the iron core losses are a known loss quantity given the operating frequency of the stator and the total back iron weight. With a maximum operating frequency of 136 Hz, the core losses are calculated to be approximately 8 W/kg. This is insignificant when compared to the primary loss components of the motor; the stator and rotor resistances.

The equivalent circuit model of the DSLIM that was formulated as part of Chapter 5 provides the likely maximum operating voltage and current of the machine. Within a 13.8 kV distribution system, it is assumed that a DC voltage of approximately 10,000 V can be used upstream of the current source inverter. In all cases, it is assumed

that semiconductor devices can be used in a serial or parallel fashion when voltage or current limiting conditions exist respectively.

6.2 Conventional Field-Oriented Simulation Results

As expected from previous results in Chapter 4, the controllability of the motor is excellent, with the thrust and hence acceleration rapidly ramping up to their required values in order to effect a launch. The maximum effort launch transient is shown below in Figure 61.

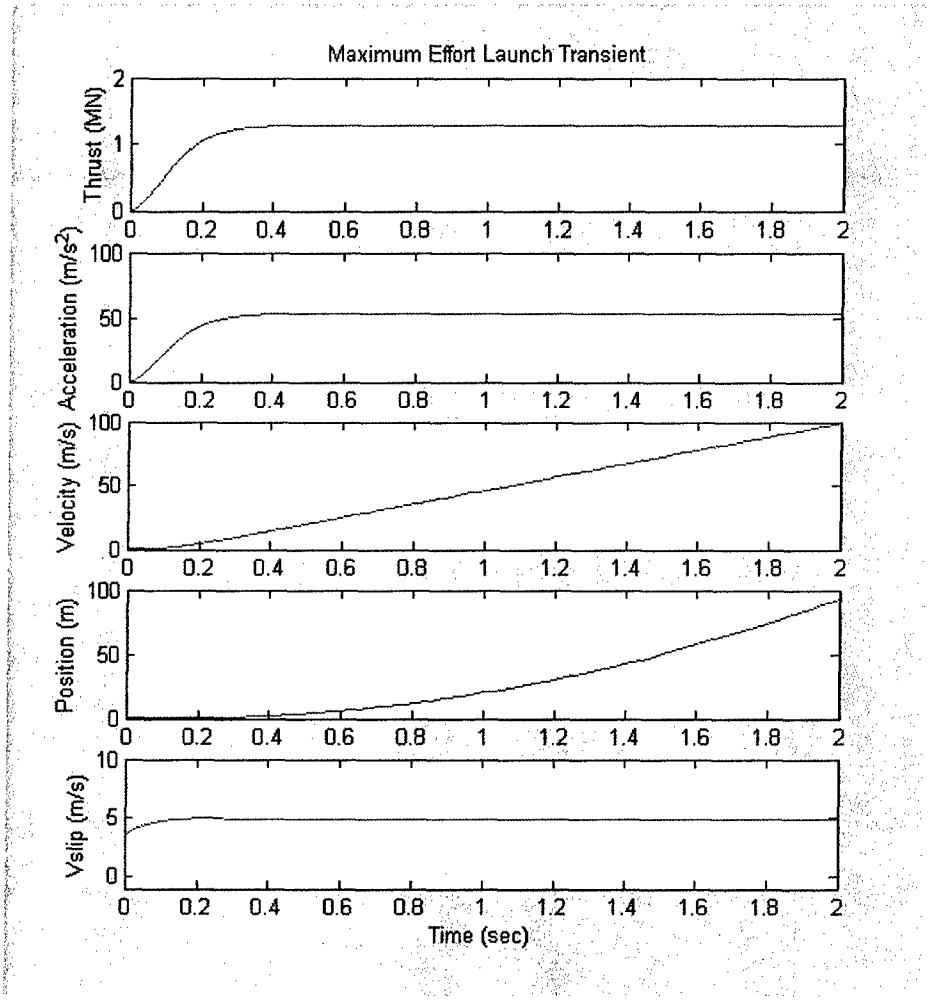

Figure 61 Maximum Effort Aircraft Launch Transient

As seen from the figure, the controller rapidly ramps the required force up to 1.3MN, causing an airframe acceleration of approximately 53 m/s^2. The aircraft attains launch velocity at approximately the 90 m point. The slip velocity, the difference in linear velocity between the synchronous field of the stator and the shuttle to which the aircraft is attached is nearly constant at 5 m/s. This corresponds to a slip of approximately .05 per unit.

The same transient is now looked at electrically. Specifically voltage, current, total developed power, and power efficiency are looked at through the transient (Figure 62).

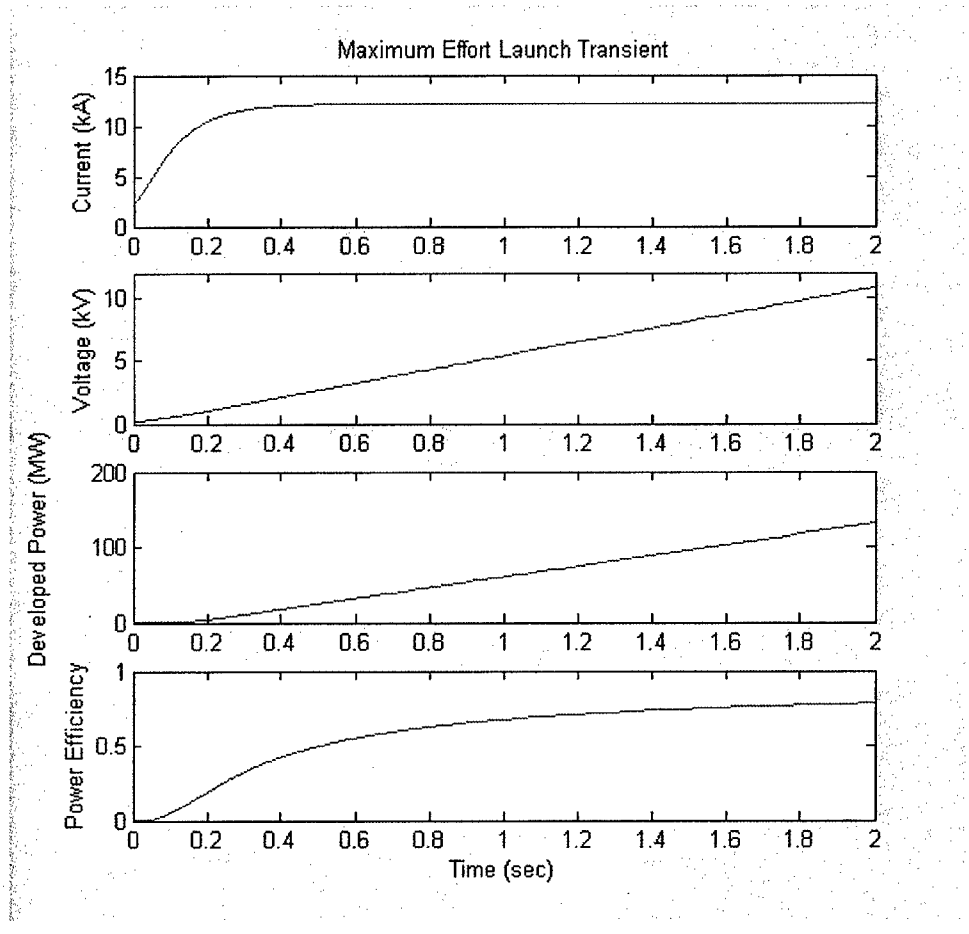

Figure 62 Electrical Operating Characteristics During Max Effort Launch Transient

As expected, because this is a field-oriented controller, the injected current is constant during the constant acceleration portion of the transient. As velocity increases, so too does the necessary applied voltage, thus also increasing the total developed power of the motor in a linear fashion. Power efficiency also increases with time, as the motor overcomes the initial transient and settles into its operating point. The motor is nearly at its steady-state operating efficiency point of 79% by the end of the transient. Thus, even in the worst-case maximum effort launch transient, the motor is nearly able to reach its steady-state operating efficiency, and therefore increase its overall energy efficiency.

Finally, the launch transient is analyzed from an energy standpoint. With the total accelerated mass of 24000 kg, and with a takeoff velocity of 100 m/s, the total kinetic energy at takeoff is easily calculated as 120MJ. This energy is divided by itself and the sum of all the loss mechanisms in the DSLIM to arrive at the total energy efficiency of the machine (Figure 63).

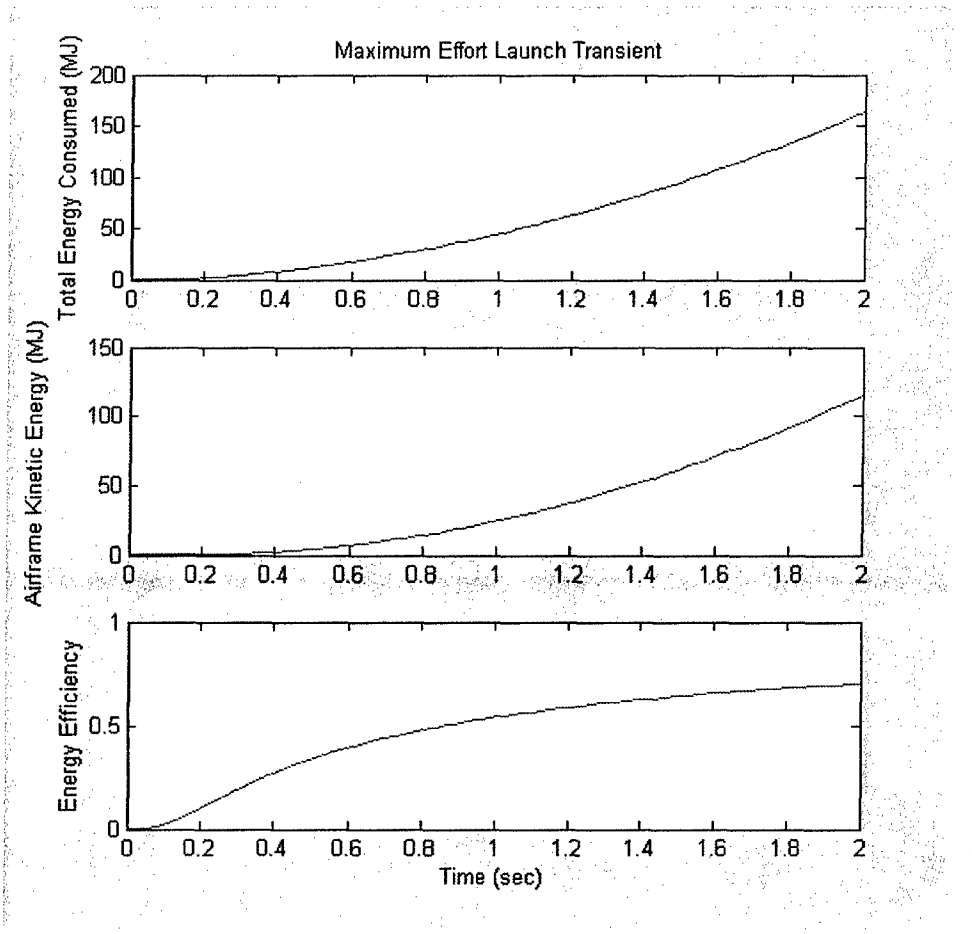

Figure 63 Maximum Effort Launch Transient Energy Efficiency

Clearly, the initial start transient is hard on the motor's overall energy efficiency. As the motor continues on through the transient, the efficiency becomes increasingly better as the motor begins to reach its steady state operating point. However, the motor never quite gets there, and the total energy efficiency of the motor reaches a peak of 70%. This is not bad considering an operating point power factor of approximately .49.

Recognizing that every launch is not going to be at the maximum effort, an average launch transient was simulated. This again consisted of a 24000 kg aircraft, but this time the takeoff velocity was 150 knots (77 m/s) and the total transient is over 2.7 seconds. Clearly, this is a much more benign transient, and since the operating thrust of the motor is likely to be lower on the thrust-slip curve, it is expected that the efficiency will be slightly higher. Figure 64 shows the launch transient.

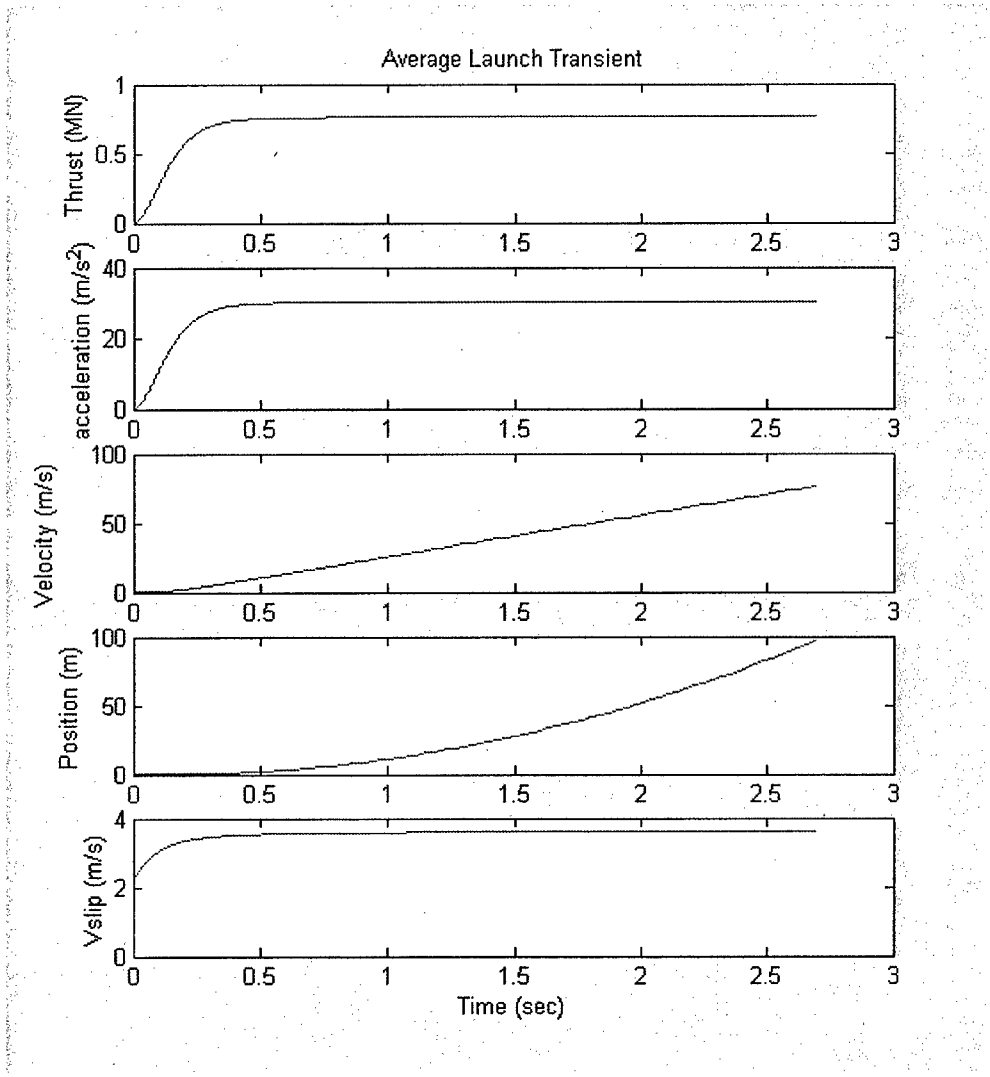

Figure 64 Average Launch Transient

Note the peak thrust for this transient is approximately 750 kN, which is a little more than half of the required thrust for the maximum effort launch. Also note the slip velocity, which is now 3.5 m/s throughout most of the transient, which also corresponds to a lower point on the thrust-slip curve of the DSLIM. Not surprisingly, the overall control of the transient is very similar to the maximum effort launch transient, with the acceleration again brought expeditiously to a level of 30 m/s^2, and held there almost perfectly throughout the entire transient.

Now, the average launch transient is considered from an electrical standpoint. Current, voltage, total power delivered, and power efficiency are plotted with respect to time to see their relationship (Figure 65). Because this is a much more benign transient, and requires lower overall thrust, it is expected that the power efficiency of the DSLIM under these operating conditions will be better than under the operating conditions of the maximum effort launch transient.

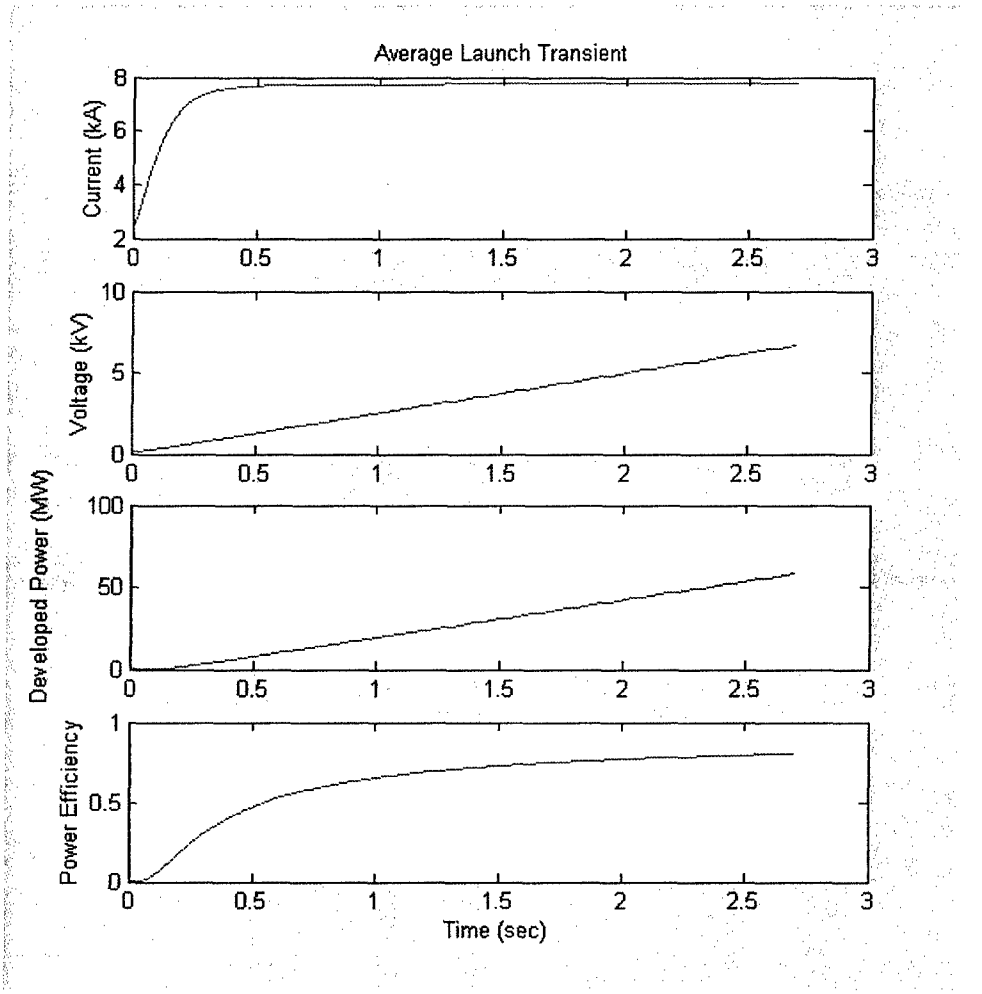

Figure 65 Electrical Characteristics during Average Launch Transient

At the very end of the launch transient, the operating efficiency of the motor is 81%. This is 2% better than the maximum effort launch transient, and entirely expected given the fact that the motor is operating at a relatively lower slip velocity.

Finally, the energy efficiency of an average launch transient is analyzed (Figure 66). Again, the start transient causes the motor to expend a lot of energy, but by the end of the transient, the total energy efficiency of the system is 73%. This is 3% more efficient than the maximum effort launch transient is. Given the highly negative slope of the thrust-slip curve for this DSLIM, and the moderate positive slope of the efficiency-slip curve, it is not at all surprising that the motor can give up half of its thrust and only gain 3% in efficiency. The thrust-slip curve and efficiency-slip curve for this DSLIM are shown in Figure 67 and Figure 68 respectively.

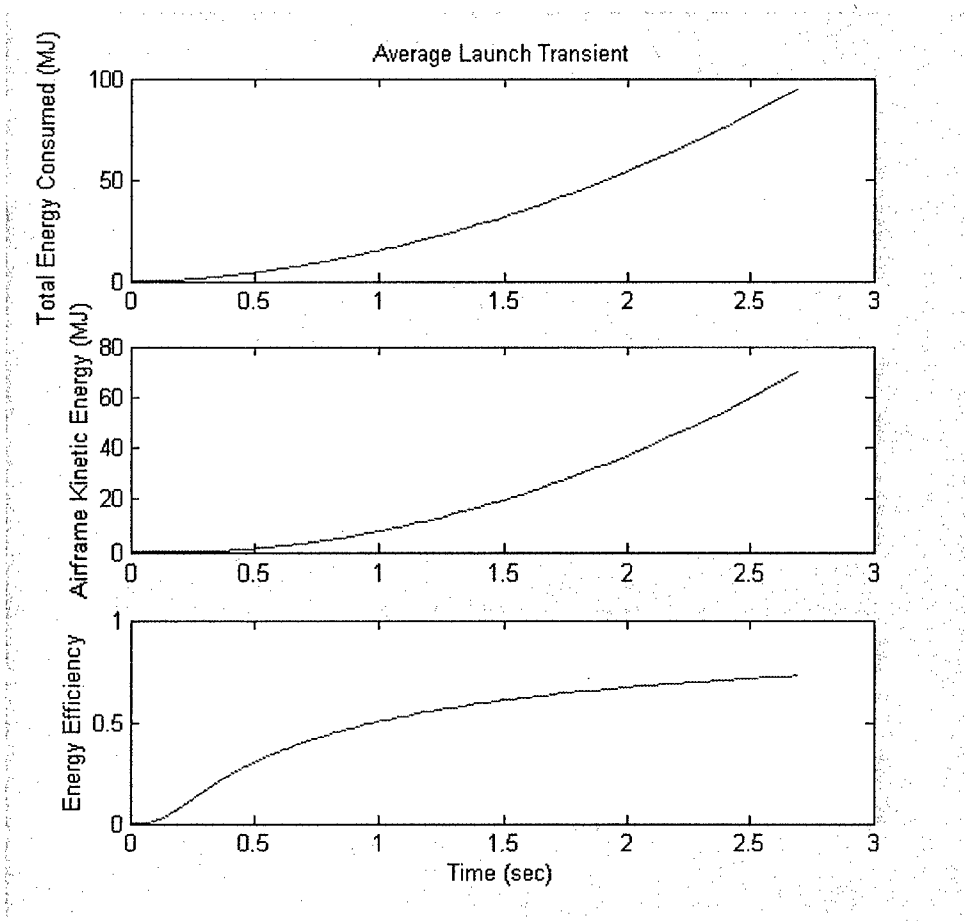

Figure 66 Average Launch Transient Energy Efficiency

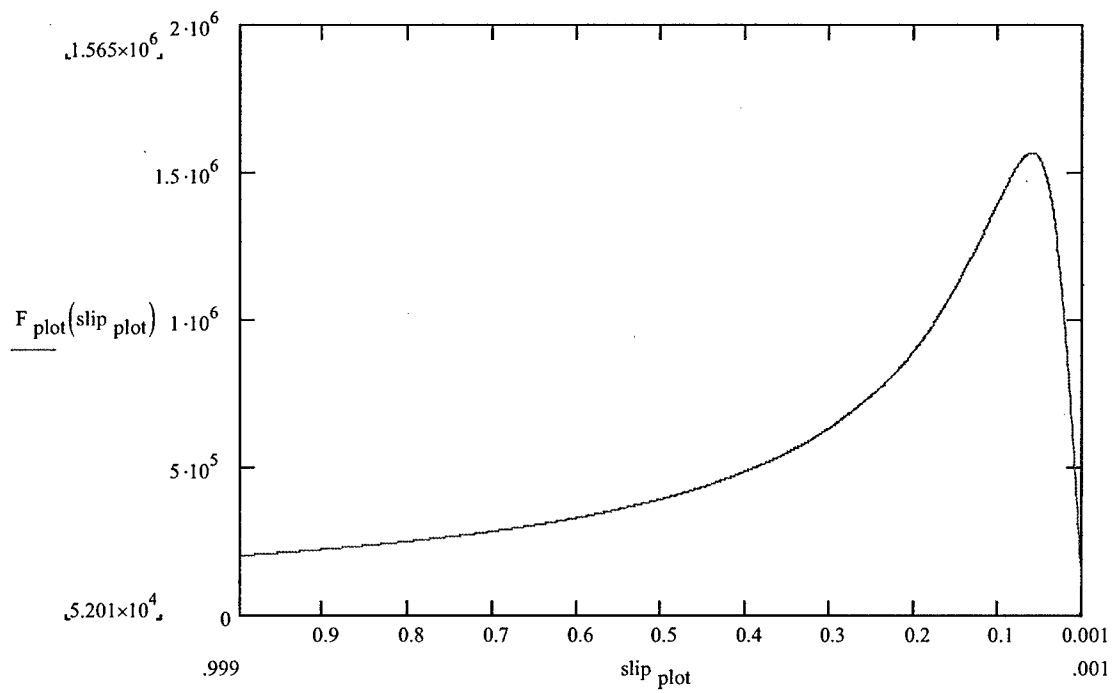

Figure 67 EMALS DSLIM Thrust-Slip Curve

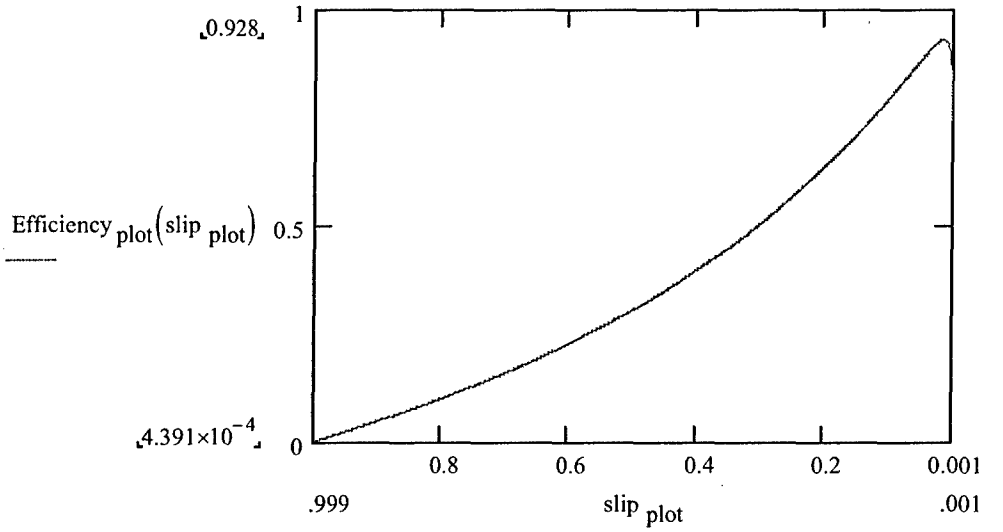

Figure 68 EMALS DSLIM Efficiency-Slip Curve

The efficiency of this DSLIM is at its maximum value of 91% at a slip of approximately .01. This equates to a thrust of approximately 400 kN. It is unknown if there are any aircraft in the US Navy inventory that require such little force for an assisted takeoff. However, with the increasing use of Unmanned Aerial Vehicles (UAV), it is possible that they would fit into such an acceleration profile.

6.3 Non-conventional Field-Oriented Simulation Results

A small change was performed in the field-oriented controller of the previous section to determine the overall impact on efficiency of bringing the field up to its nominal level over the surface of the shuttle before starting the acceleration of the shuttle. The field-oriented controller is actually two different PID controllers. One PID controller establishes the field of the machine through direct axis current. The second PID controller establishes the thrust (acceleration) of the machine through quadrature axis current. The second PID controller, known hereafter as the acceleration controller, was set to establish an acceleration of 0 m/s^2 for the first .5 seconds of the launch transient, while the first PID controller, known hereafter as the rotor flux controller, was allowed to establish normal rotor flux. The .5 seconds corresponds to roughly five rotor electrical time constants, or essentially a steady-state condition for the rotor flux. At .5 seconds, the acceleration controller set the normal acceleration for the aircraft, which caused the quadrature axis current to ramp up to its required level and also caused the rotor flux wave to start moving down the length of the track. The desired result is to increase the overall efficiency of the motor by mitigating the losses associated with bringing the rotor flux wave up to its desired level before the actual launch begins.

This new field-oriented controller was run with average launch transient parameters to determine if it had any impact on the overall efficiency of the machine. Figure 69 shows the average launch transient with this non-conventional field-oriented controller.

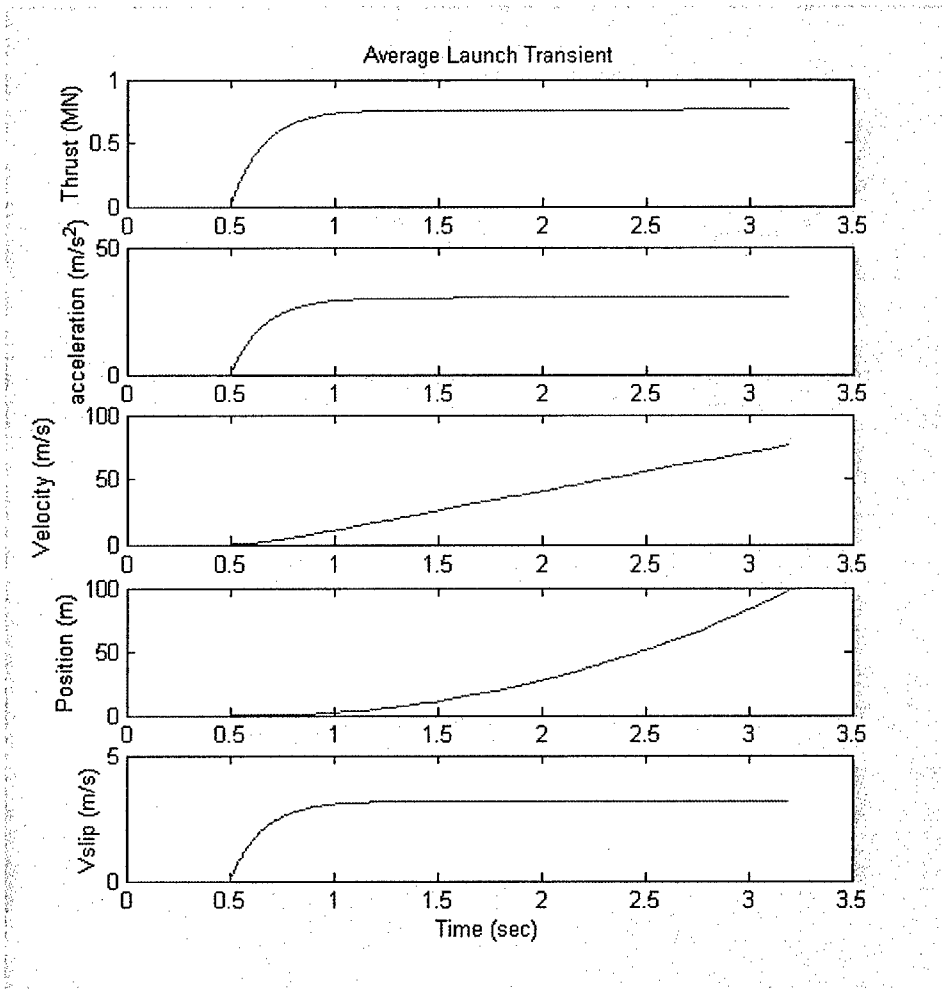

Figure 69 Average Launch Transient (Non-Conventional Controller)

The transient is nearly identical to that of the previous average launch transient, except the acceleration does not start until .5 seconds into the transient, and does not finish until the 3.2 second point. The electrical characteristics of the transient are shown in Figure 70 below.

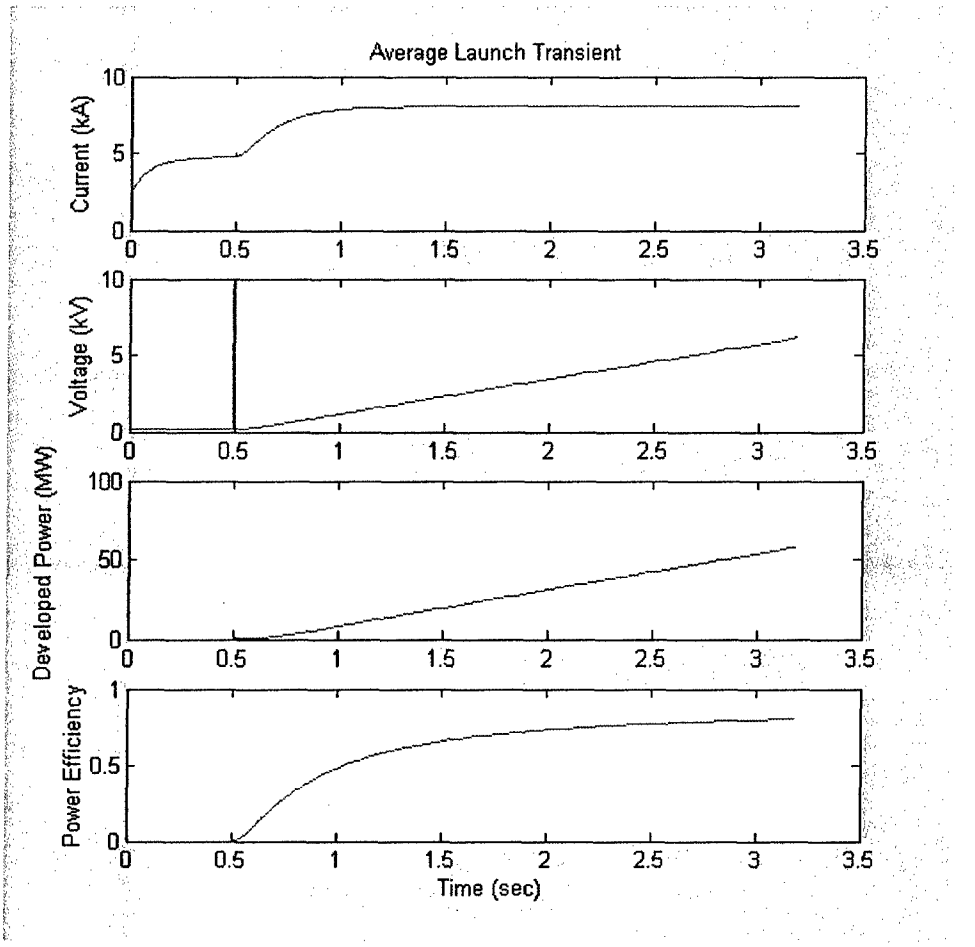

Figure 70 Average Launch Transient Electrical Characteristics (Non-conventional)

The difference here is clear in that the current for the machine ramps up twice. The first ramp represents the current used to establish the shuttle flux. The second ramp represents the current used to establish the acceleration of the shuttle. Note that the first current ramp is nearly level before the second ramp is initiated. This is a good indication that the shuttle flux is established by the time the acceleration of the shuttle is initiated. The perturbation in the voltage at the .5 second point is caused by problems that the ODE45 solver in Matlab has with a step jump in the required acceleration. The actual voltage is expected to ramp up gradually throughout the launch transient, as it is shown doing. Finally, this control scheme variation was analyzed for its overall energy efficiency. Figure 71 below shows the overall energy efficiency of the machine at the end of the transient.

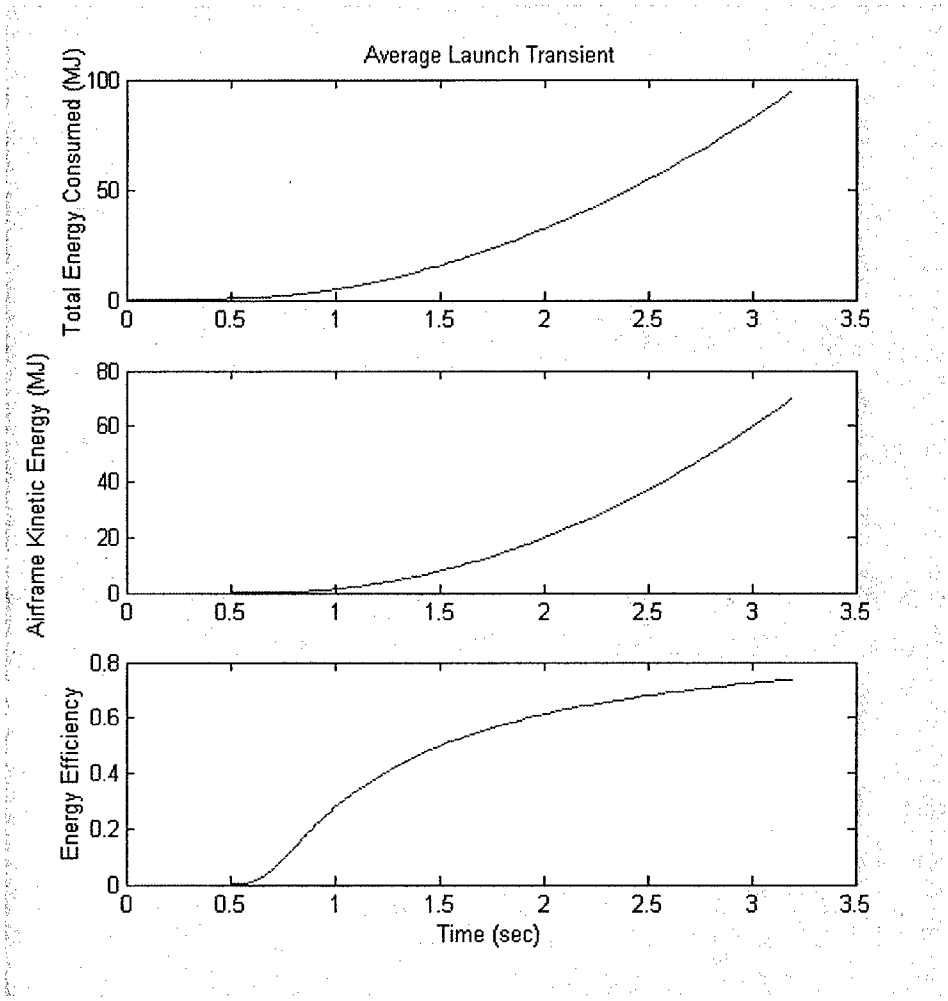

Figure 71 Average Launch Transient Energy Efficiency (Non-Conventional)

This is very similar to the energy efficiency using the conventional field-oriented controller. The energy efficiency using this control scheme variation is approximately 75%, which is 2% better than the conventional field-oriented control scheme. From an efficiency point of view, it is a slightly better method of controlling the aircraft launch transient. It could also provide for an indication of the motor's health prior to launch by energizing the windings of the motor and measuring whether the motor is responding properly. From the standpoint of safety alone, this control method is probably the most desirable control method available.

THIS PAGE INTENTIONALLY BLANK

Chapter 7

7.0 Conclusions and Recommendations

7.1 Conclusions

This thesis was begun with an incomplete understanding of linear motors in general. Much of the past written work on linear motors focused on mass transit systems and the short-primary type of DSLIM as a novel means of a traction force rather than wheels. Virtually all of this work focused on the end effect as the single-most deleterious effect on linear motor efficiency [6], [9], [10], [11], [14]. This is indeed the case for short primary DSLIM, where the forward velocity of the vehicle makes it extremely difficult for the magnetic field to establish itself over the secondary-conducting sheet. On the other hand, while leakage flux and inductance were also identified as contributing factors to poor efficiency, they were identified as lesser contributors. The single greatest cause of the leakage flux in short primary DSLIM was correctly identified as the large airgap, which was necessitated by having to provide a safe clearance between the stator and the secondary-conducting sheet. The transverse edge effect's decrease on secondary resistivity was the only major peculiarity that the short-primary and short-secondary DSLIM had in common.

The effect that the end effect has on the peak thrust of a short-secondary DSLIM is drastically reduced once the shuttle (secondary) goes beyond one pole pitch in length, and is effectively negated once the shuttle is about 7 pole pitches in length. With an aircraft launcher using a pole pitch of .385 m, and a shuttle that is 9 m long, clearly the end effect is not a significant issue. Chapter 5 has shown that the difference in thrust, with a shuttle that is 7 pole pitches long, is no more than 5% at any slip. Thus, using a factor of .95 in the total thrust calculation adequately accounts for this effect.

Leakage flux, however, is the single biggest issue in a DSLIM. The struggle in the design process is focusing the flux on exactly where the shuttle is at any time. The problem is that as the shuttle moves down the track, this requires the energization and deenergization of track sections as the shuttle enters and leaves respectively. In order to focus the maximum flux possible, single pole pairs at a time could be energized, with the equivalent of only a single pole of leakage flux at either end of the shuttle. An approach such as this, assuming a pole pitch of .385 m, would have required a track split up into 258 individual sections. Clearly this is unrealistic, but it does provide for the least

amount of leakage flux. This design proceeded under the assumption that no stator section should be less than 2.5 m, and thus a more reasonable number of individual stator sections resulted. The final, optimal design had a total of 26 stator sections, and yet it still had a leakage inductance that was nearly equal to its mutual inductance. Its power factor at its maximum thrust operating point was abysmal at .49, but even still it could manage an operating efficiency of .79. This is a testament to the low stator resistance of the motor, which is a direct result of the motor's geometry. In maximum effort operation, it is capable of a theoretical maximum energy efficiency of 70%.

It is important to remember that this is a *theoretical* efficiency. Transient impedance effects such as the gating of thyristors as individual stator sections are turned on or off are not modeled here, and these effects could have a serious consequence on the overall efficiency of the machine. Other systems would also have to be taken into account in the overall efficiency, such as a cooling system for the shuttle, or a braking system for the shuttle. Also important to remember here is that there are energy recovery methods available that are not in the model. These could boost the overall energy efficiency. The thrust of this thesis has been to focus on the motor, and how it is controlled, and to glean an energy efficiency for those 2 inter-twined systems. The thrust of this thesis has not been to look at all of the necessary support systems. Clearly this would be required for the eventual placement of a DSLIM on an aircraft carrier such as the CVN-21.

Another key point of this paper is that the method of controlling the DSLIM has an effect on the overall efficiency of the machine. While it was not the primary focus of this work, the variation on the field-oriented controller that established the shuttle flux before the initiation of the shuttle acceleration was clearly a safer control scheme in that it allowed the coils of the motor to be energized first to allow the control system to gauge the 'health' of the motor before initiating acceleration. This control scheme also allowed for a small increase in overall efficiency of approximately 2%. While the increase in efficiency is inconsequential, the added safety factor for the aircrew is significant and that alone makes it worthwhile.

7.2 Recommendations for Future Work

It was originally this author's intent to make a small scale DSLIM to use as an educational tool as to how DSLIMs work, and to perhaps do some minor testing of peak thrust and efficiency. This has only been partially completed, and is not ready for

assembly as of the writing of this thesis. The recommendation of future work going forward from this thesis and the body of knowledge that it drew from is to build a small-scale DSLIM for educational and testing purposes. Of specific interest to the author is the building of a small-scale motor on which performance testing could be conducted to determine the adequacy of theoretically-derived performance data in its ability to predict actual motor performance. Because of the cost and complexity of field-oriented controllers, they would not be used. Instead, a simple Volts per Hertz controller would be used to drive the motor, and simple known masses would be accelerated. The velocity of these known masses would be measured at the end of the acceleration, and a kinetic energy could be calculated. This would be used to determine the operating thrust of the motor. Assuming a simple data acquisition system such as Labview could record the transient electrically, an overall energy efficiency could also be calculated. A simple system such as this could prove a highly valuable teaching tool in a laboratory environment.

THIS PAGE INTENTIONALLY BLANK

References

[1] Richard Bushway, "Electromagnetic Aircraft Launch System Development Considerations," *IEEE Transactions on Magnetics*, January 2001.

[2] Global Security, "Electromagnetic Aircraft Launch System – EMALS," April 2004, http://www.globalsecurity.org/military/systems/ship/systems/emals.html.

[3] Michael R. Doyle, Douglas J. Samuel, Thomas Conway, Robert R. Klimowski, "Electromagnetic Aircraft Launch System – EMALS," *IEEE Transactions on Magnetics*, January 1995.

[4] Amy Dwyer, "Aircraft Design for Carrier Operations," Naval Air Systems Command Briefing (Air 4.10), November 1997.

[5] Daniel Raymer, *Aircraft Design: A Conceptual Approach Third Edition*, American Institute of Aeronautics and Astronautics Inc., 1999.

[6] Sakae Yamamura, *Theory of Linear Induction Motors*. John Wiley and Sons, 1972.

[7] Old Dominion University Maglev Train News Report, "Glitches Postpone Debut of Maglev," October 10, 2002, http://www.odu.edu/af/maglev/files/glitchestext.html

[8] Greg Paula, "Evaluating EPACT's Impact," Mechanical Engineering Magazine, June 1998.

[9] E. R. Laithwaite, *Induction Machines for Special Purposes*, George Newnes Limited, 1966.

[10] Ion Boldea and S.A. Nasar, *Linear Motion Electromagnetic Devices*, Taylor and Francis, 2001.

[11] S. A. Nasar, *Handbook of Electric Machines*, McGraw Hill, 1987.

[12] James L. Kirtley (private communication), 2004.

[13] D. Patterson, et al, "Design and Simulation of an Electromagnetic Aircraft Launch System," *IEEE Review*, 2002

[14] E. R. Laithwaite, *Transport Without Wheels*, Elek Science, 1977.

[15] M. A. Plonus, *Applied Electromagnetics*, McGraw Hill, 1978.

[16] Malcolm Barnes, *Practical Variable Speed Drives and Power Electronics*, Newnes, 2003.

[17] Peter Vas, *Sensorless Vector and Direct Torque Control*, Oxford Science Publications, 1998.

[18] Ion Boldea and S. A. Nasar, *Vector Control of AC Drives*, CRC Press, 1992.

[19] "Induction Machine Control and Simulation," class notes for 6.685, Department of Electrical Engineering and Computer Science, Massachusetts Institute of Technology, Spring 2004.

[20] B. K. Bose, *Power Electronics and Variable Frequency Drives*, IEEE Press, 1997

[21] Robert Hebner, Joseph Eno, Alan Walls, "Flywheel Batteries Come Around Again," IEEE Spectrum, April 2002.

[22] Robert Walker (email conversation), Naval Surface Warfare Center – Carderock Division, 2005.

[23] Metglas Inc., "Magnetic Alloy 2605CO (Iron-based) Technical Bulletin," 2004.

[24] Fukuryo Semicon Engineering Corporation, "A 6kV/5kA Reverse Conducting GCT," 2001.

[25] E. R. Laithwaite, "Adapting a linear induction motor for the acceleration of large masses to high velocities," IEE Proceedings, July 1995.

Appendix A – One Dimensional Model

THIS PAGE INTENTIONALLY BLANK

Appendix A One-Dimensional Steady-State Model

$$g \cdot \frac{dH_y}{dx} = K_s + K_r$$

$K_s = K_o \cdot e^{j \cdot (k \cdot x - \omega \cdot t)}$ primary current

g = airgap length

$k = \frac{\pi}{\tau}$ τ = pole pitch (meters)

d = secondary thickness

$\omega = \frac{\pi}{\tau} \cdot V_s$ V_s = synchronous speed

V = shuttle speed

$$\frac{dE_r}{dx} = \frac{dH_y}{dt}$$ Faraday's Law

$K_r = \sigma_s \cdot E_2$ Rotor surface current

$\sigma_s = \sigma \cdot d$ (surface conductivity)

$$\frac{1}{\sigma_s} \cdot \frac{dK_r}{dx} = \frac{dH_y}{dt}$$

$$g \cdot \frac{d^2 H_y}{dx^2} = \frac{dK_s}{dx} + \sigma_s \cdot \frac{dH_y}{dt}$$

$$g \cdot \frac{d^2 H_y}{dx^2} = 2 \cdot \mu_0 \cdot \frac{dK_s}{dx} + \sigma_s \cdot \mu_0 \cdot \frac{dH_y}{dt}$$

$$\frac{dH_y}{dt} = \frac{dH_y}{dt} + V \cdot \frac{dH_y}{dx}$$ V = shuttle speed

$$g \cdot \frac{d^2 H_y}{dx^2} = \frac{dK_s}{dx} + \sigma_s \cdot \mu_0 \cdot \left(\frac{dH_y}{dt} + V \cdot \frac{dH_y}{dx} \right)$$

$$H_y = H_o \cdot e^{j(k \cdot x - \omega \cdot t + \delta)}$$

$$\frac{d^2H_y}{dx^2} = -k^2 \cdot H_o \cdot e^{j(k \cdot x - \omega \cdot t + \delta)} \qquad \frac{dK_s}{dx} = j \cdot k \cdot K_o \cdot e^{j(k \cdot x - \omega \cdot t)}$$

$$\frac{dH_y}{dt} = -j \cdot \omega \cdot H_o \cdot e^{j(k \cdot x - \omega \cdot t + \delta)} \qquad \frac{dH_y}{dx} = j \cdot k \cdot H_o \cdot e^{j(k \cdot x - \omega \cdot t + \delta)}$$

substituting into the original equation...

$$-g \cdot k^2 \cdot H_o \cdot e^{j(k \cdot x - \omega \cdot t + \delta)} = j \cdot k \cdot K_o \cdot e^{j(k \cdot x - \omega \cdot t)} + \mu_o \cdot \sigma_s \cdot (-j \cdot \omega + j \cdot k \cdot V) \cdot H_o \cdot e^{j(k \cdot x - \omega \cdot t + \delta)}$$

or...

$$-g \cdot k^2 \cdot H_o \cdot e^{j\delta} = j \cdot k \cdot K_o + \mu_o \cdot \sigma_s \cdot (-j \cdot \omega + j \cdot k \cdot V) \cdot H_o \cdot e^{j\delta}$$

Real parts yield:

$$\delta = \tan^{-1}\left[\frac{-g \cdot \left(\frac{\pi}{\tau}\right)}{\mu_o \cdot \sigma_s \cdot (V_s - V)}\right]$$

Imaginary parts yield:

$$H_o = \frac{K_o}{-g \cdot \left(\frac{\pi}{\tau}\right) \cdot \sin(\delta) + \mu_o \cdot \sigma_s \cdot (Vs - V) \cdot \cos(\delta)}$$

Using Poynting's Theorem for Time-Average Thrust over the length of the shuttle:

$$\text{Thrust} = D \cdot \frac{1}{2} \cdot K_1 \cdot B_y \cdot \cos(-\delta_b) \cdot \int_0^L 1 \, dx$$

$$\text{Thrust} = \frac{D}{2} \cdot K_1 \cdot B_y \cdot L \cdot \cos(-\delta_b)$$

L = length of secondary (shuttle)
D = depth of primary

$$\text{slip} = \frac{(V_s - V)}{V_s}$$

$$V = (1 - \text{slip}) \cdot V_s$$

Short Primary DSLIM Motor Parameters

$f = 50\text{Hz}$	$g = 15\text{mm}$	$K_1 = 65300\frac{A}{m}$
$V_s = 9\frac{m}{s}$	$d = 5\text{mm}$	
		$\tau = 90\text{mm}$
poles = 4	$D = 90\text{mm}$	Aluminum secondary

from Yamamura's 'Linear Induction Motor Theory'

THIS PAGE INTENTIONALLY BLANK

Appendix B – End Effect Model

THIS PAGE INTENTIONALLY BLANK

Appendix B One-Dimensional Model with End Effects

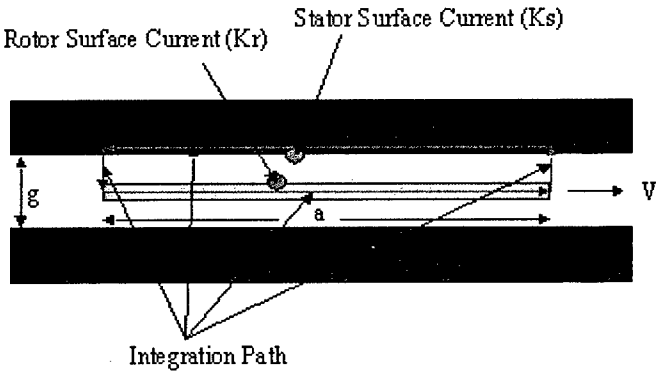

τ = pole pitch (m) Vs = synchronous speed

$\lambda = 2\cdot\tau$ $k = \frac{2\cdot\pi}{\lambda}$ $k = \frac{\pi}{\tau}$

$V_s = 2\cdot\frac{\tau}{T}$ $T = \frac{2\cdot\pi}{\omega}$ $V_s = \frac{\tau}{\pi}\cdot\omega$ $\omega = \frac{\pi}{\tau}\cdot V_s$

s = slip $s = \frac{V_s - V}{V_s}$

$\omega_s = s\cdot\omega$ slip frequency

$\omega_s = \frac{\pi}{\tau}\cdot(V_s - V)$

x is referenced to a coordinate system moving with the rotor

The derivation will proceed under the assumption that the B-field in the airgap is only y-directed.

$$\frac{1}{2}\cdot g\cdot\frac{dH_y}{dx} = K_s + K_r \qquad \text{(Ampere's Law)}$$

$$\frac{1}{2}\cdot\frac{g}{\mu}\cdot\frac{dB_y}{dx} = K_s + K_r \qquad \text{(Eq. 1)}$$

Stator surface current density is of the form:

$$K_s = K_o\cdot e^{j\cdot\frac{\pi}{\tau}\cdot\left[x-(V_s-V)\cdot t\right]} \qquad \text{(Eq. 2)}$$

On rotor, referencing Faraday's Law of Induction

$$\frac{dE_z}{dx} = \frac{dB_y}{dt}$$

$$\frac{dK_r}{dx} = \sigma_r \cdot \frac{dB_y}{dt} \qquad \text{(Eq. 3)} \qquad \text{where } \sigma_r = \text{rotor surface conductivity}$$

Taking the second derivative of Eq. 1, and plugging in Eq. 2 and 3:

$$\frac{d^2B_y}{dx^2} = \frac{2\cdot\mu}{g}\cdot\left[j\cdot\frac{\pi}{\tau}\cdot K_o \cdot e^{j\cdot\frac{\pi}{\tau}\cdot\left[x-\left(V_s-V\right)t\right]} + \sigma_r\cdot\frac{dB_y}{dt}\right]$$

B_y will be of the form:

$$B_y = B_o \cdot e^{-j\cdot\frac{\pi}{\tau}\cdot\left(V_s-V\right)t}$$

$$\frac{dB_y}{dt} = -j\cdot\frac{\pi}{\tau}\cdot\left(V_s - V\right)B_o\cdot e^{-j\cdot\frac{\pi}{\tau}\cdot\left(V_s-V\right)t}$$

which leads to:

$$\frac{d^2B_o}{dx^2}\cdot e^{-j\cdot\frac{\pi}{\tau}\cdot\left(V_s-V\right)t} = \frac{2\cdot\mu}{g}\cdot\left[j\cdot\frac{\pi}{\tau}\cdot K_o\cdot e^{j\cdot\frac{\pi}{\tau}\cdot x} \cdot e^{-j\cdot\frac{\pi}{\tau}\cdot\left(V_s-V\right)\cdot t} - j\cdot\sigma_r\cdot\frac{\pi}{\tau}\cdot\left(V_s - V\right)\cdot B_o\cdot e^{-j\cdot\frac{\pi}{\tau}\cdot\left(V_s-V\right)\cdot t}\right]$$

the time variations cancel out, leaving:

$$\frac{d^2B_o}{dx^2} = \frac{2\cdot\mu}{g}\cdot\left[j\cdot\frac{\pi}{\tau}\cdot K_o\cdot e^{j\cdot\frac{\pi}{\tau}\cdot x} - j\cdot\sigma_r\cdot\frac{\pi}{\tau}\cdot\left(V_s - V\right)\cdot B_o\right]$$

rearranging terms:

$$\frac{d^2B_o}{dx^2} + j\cdot\frac{2\cdot\mu\cdot\sigma_r}{g}\cdot\left(\frac{\pi}{\tau}\right)\cdot\left(V_s - V\right)\cdot B_o = j\cdot\frac{2\cdot\mu}{g}\cdot\left(\frac{\pi}{\tau}\right)\cdot K_o\cdot e^{j\cdot\frac{\pi}{\tau}\cdot x}$$

Particular Solution will be of the form:

$$B_{op} = C_o \cdot e^{j \cdot \frac{\pi}{\tau} \cdot x}$$

$$\frac{dB_{op}}{dx} = j \cdot \left(\frac{\pi}{\tau}\right) \cdot C_o \cdot e^{j \cdot \frac{\pi}{\tau} \cdot x}$$

$$\frac{d^2 B_{op}}{dx^2} = -\left(\frac{\pi}{\tau}\right)^2 \cdot C_o \cdot e^{j \cdot \frac{\pi}{\tau} \cdot x}$$

plugging this into the differential equation:

$$-\left(\frac{\pi}{\tau}\right)^2 \cdot C_o \cdot e^{j \cdot \frac{\pi}{\tau} \cdot x} + j \cdot \frac{2 \cdot \mu \cdot \sigma_r}{g} \cdot \left(\frac{\pi}{\tau}\right) \cdot (V_s - V) \cdot C_o \cdot e^{j \cdot \frac{\pi}{\tau} \cdot x} = j \cdot \frac{2 \cdot \mu}{g} \cdot \left(\frac{\pi}{\tau}\right) \cdot K_o \cdot e^{j \cdot \frac{\pi}{\tau} \cdot x}$$

$$\left[j \cdot \frac{2 \cdot \mu \cdot \sigma_r}{g} \cdot (V_s - V) - \frac{\pi}{\tau} \right] \cdot C_o = j \cdot \frac{2 \cdot \mu}{g} \cdot K_o$$

$$C_o = \frac{j \cdot \frac{2 \cdot \mu}{g} \cdot K_o}{\left[j \cdot \frac{2 \cdot \mu \cdot \sigma_r}{g} \cdot (V_s - V) - \frac{\pi}{\tau} \right]}$$

Homogeneous solution will be:

$$r^2 + j\cdot\frac{2\cdot\mu\cdot\sigma_r}{g}\cdot\left(\frac{\pi}{\tau}\right)\cdot\left(V_s - V\right) = 0$$

$$r_{pos} = j\cdot\sqrt{j\cdot\frac{2\cdot\mu\cdot\sigma_r}{g}\cdot\left(\frac{\pi}{\tau}\right)\cdot\left(V_s - V\right)}$$

$$r_{neg} = -j\cdot\sqrt{j\cdot\frac{2\cdot\mu\cdot\sigma_r}{g}\cdot\left(\frac{\pi}{\tau}\right)\cdot\left(V_s - V\right)}$$

$$\alpha = \sqrt{j\cdot\frac{2\cdot\mu\cdot\sigma_r}{g}\cdot\left(\frac{\pi}{\tau}\right)\cdot\left(V_s - V\right)}$$

$$B_{oh} = C_1\cdot e^{j\cdot\alpha\cdot x} + C_2\cdot e^{-j\cdot\alpha\cdot x}$$

The total solution will be of the form:

$$B_o = C_o\cdot e^{j\cdot\frac{\pi}{\tau}\cdot x} + C_1\cdot e^{j\cdot\alpha\cdot x} + C_2\cdot e^{-j\cdot\alpha\cdot x}$$

and:

$$B_y = B_o\cdot e^{-j\cdot\frac{\pi}{\tau}\cdot\left(V_s - V\right)\cdot t}$$

B_o is comprised of the spatially steady state response due to the applied magnetic field as well as 2 travelling waves created as a result of the magnetic diffusion into the rotor. These diffusion waves, one forward travelling and one reverse travelling, are comprised of a real and an imaginary part, and as a result, their magnitudes decay as they progress further into the rotor. It can be seen that the magnitude of the exponent, α, is directly proportional to the slip of the rotor. The larger the disparity between synchronous speed and rotor speed, the larger the value of the exponent (both real and imaginary parts).

Boundary conditions need to be established in order to determine C_1 and C_2. It is known that the rotor surface current will be a sinusoidal function as a result of the applied magnetic field. The rotor is a sheet of metal of finite length, and as such, all of the z-directed rotor surface currents must sum to zero. If they indeed sum to zero, then it follows that the magnetic field across the rotor must behave as though it is due only to the stator current since the total sum of the rotor current will be zero. This sets up the following integration in which the limits are set just outside the rotor on either end, thus the net sum of rotor current is zero. Because the magnetic field must be continuous across the boundary due to the same reasoning, the results at either end are set equal to each other, and the constants may be solved for.

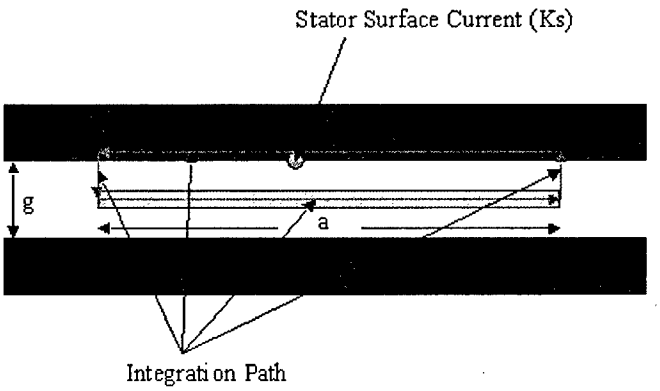

Using Ampere's Law:

$$\frac{1}{2}\cdot g\cdot\frac{dH_y}{dx} = K_s \qquad K_s = K_o\cdot e^{j\cdot\frac{\pi}{\tau}\cdot\left[x-\left(V_s-V\right)\cdot t\right]}$$

$$\frac{1}{2}\cdot\frac{g}{\mu}\cdot\frac{dB_y}{dx} = K_s$$

$$\frac{dB_y}{dx} = \frac{2\cdot\mu\cdot K_s}{g}$$

$$\frac{dB_y}{dx} = \frac{2\cdot\mu}{g}\cdot K_o\cdot e^{j\cdot\frac{\pi}{\tau}\cdot\left[x-\left(V_s-V\right)\cdot t\right]}$$

$$B_y(x,t) = \frac{2\cdot\mu}{g}\cdot K_o\cdot e^{-j\cdot\frac{\pi}{\tau}\cdot(V_s - V)\cdot t}\cdot\int e^{j\cdot\frac{\pi}{\tau}\cdot x}\,dx$$

$$B_y(x,t) = \frac{-j\cdot 2\cdot\mu\cdot\tau}{\pi\cdot g}\cdot K_o\cdot e^{j\cdot\frac{\pi}{\tau}\cdot\left[x-(V_s - V)\cdot t\right]}$$

$$B_o(x) = \frac{-j\cdot 2\cdot\mu\cdot\tau}{\pi\cdot g}\cdot K_o\cdot e^{j\cdot\frac{\pi}{\tau}\cdot x}$$

$$B_o(0) = -j\cdot\frac{2\cdot\mu\cdot\tau}{\pi\cdot g}\cdot K_o = C_o + C_1 + C_2$$

$$B_o(a) = -j\cdot\frac{2\cdot\mu\cdot\tau}{\pi\cdot g}\cdot K_o\cdot e^{j\cdot\frac{\pi}{\tau}\cdot a} = C_o\cdot e^{j\cdot\frac{\pi}{\tau}\cdot a} + C_1\cdot e^{j\cdot\alpha\cdot a} + C_2\cdot e^{-j\cdot\alpha\cdot a}$$

Solving for C_1 and C_2 yields:

$$C_2 = \frac{B_o(a) + \left(e^{j\cdot\alpha\cdot a} - e^{j\cdot\frac{\pi}{\tau}\cdot a}\right)\cdot C_o - B_1\cdot e^{j\cdot\alpha\cdot a}}{\left(e^{-j\cdot\alpha\cdot a} - e^{j\cdot\alpha\cdot a}\right)}$$

$$C_1 = B_o(0) - C_o - C_2$$

Now, for solving for rotor current explicitly

$$\frac{dK_r}{dx} = -j\cdot\sigma_r\cdot\left(\frac{\pi}{\tau}\right)\cdot\left(V_s - V\right)\cdot B_o\cdot e^{-j\cdot\frac{\pi}{\tau}\cdot\left(V_s - V\right)t}$$

$$K_r = -j\cdot\sigma_r\cdot\left(\frac{\pi}{\tau}\right)\cdot\left(V_s - V\right)\cdot e^{-j\cdot\frac{\pi}{\tau}\cdot\left(V_s - V\right)\cdot y}\cdot\int B_o\,dx$$

$$K_r = -j\cdot\sigma_r\cdot\left(\frac{\pi}{\tau}\right)\cdot\left(V_s - V\right)\cdot e^{-j\cdot\frac{\pi}{\tau}\cdot\left(V_s - V\right)\cdot t}\cdot\left(-j\left(\frac{\tau}{\pi}\right)\cdot C_o\cdot e^{j\cdot\frac{\pi}{\tau}\cdot x} - j\cdot\frac{1}{\alpha}\cdot C_1\cdot e^{j\cdot\alpha\cdot x} + j\cdot\frac{1}{\alpha}\cdot C_2\cdot e^{-j\cdot\alpha\cdot x}\right) + C_3$$

In order to solve for the final constant of integration, the rotor surface current boundary condition is invoked:

$$\int_0^a K_r\,dx = 0$$

$$-j\cdot\sigma_r\cdot\left(\frac{\pi}{\tau}\right)\cdot\left(V_s - V\right)\cdot e^{-j\cdot\frac{\pi}{\tau}\cdot\left(V_s - V\right)\cdot t}\cdot\left[-\left(\frac{\tau}{\pi}\right)^2\cdot C_o\cdot e^{j\cdot\frac{\pi}{\tau}\cdot x} - \left(\frac{1}{\alpha}\right)^2\cdot C_1\cdot e^{j\cdot\alpha\cdot x} - \left(\frac{1}{\alpha}\right)^2\cdot C_2\cdot e^{-j\cdot\alpha\cdot x}\right] + C_3\cdot x$$

evaluated at x = a and x = 0 yields:

$$C_3 = j\cdot\frac{\sigma_r}{a}\cdot\left(\frac{\pi}{\tau}\right)\cdot\left(V_s - V\right)\cdot e^{-j\cdot\frac{\pi}{\tau}\cdot\left(V_s - V\right)\cdot t}\cdot\left[\left(1 - e^{j\cdot\frac{\pi}{\tau}\cdot a}\right)\cdot\left(\frac{\tau}{\pi}\right)^2\cdot C_o + \left(1 - e^{j\cdot\alpha\cdot a}\right)\cdot\left(\frac{1}{\alpha}\right)^2\cdot C_1 + \left(1 - e^{-j\cdot\alpha\cdot a}\right)\cdot\left(\frac{1}{\alpha}\right)^2\cdot C_2\right]$$

Thus the rotor current is fully determined for any point along the rotor at any given instant of time. This current, when multiplied times the magnetic field and integrated over the face of the rotor, will give the net force on the rotor. It has been assumed through this derivation that there is sufficient rotor surface outside the active primary zone to allow current to flow in the x-direction to complete the circuit, so to speak.

THIS PAGE INTENTIONALLY BLANK

Appendix C – Spatial Harmonics

THIS PAGE INTENTIONALLY BLANK

Appendix C Spatial Harmonic Fourier Analysis

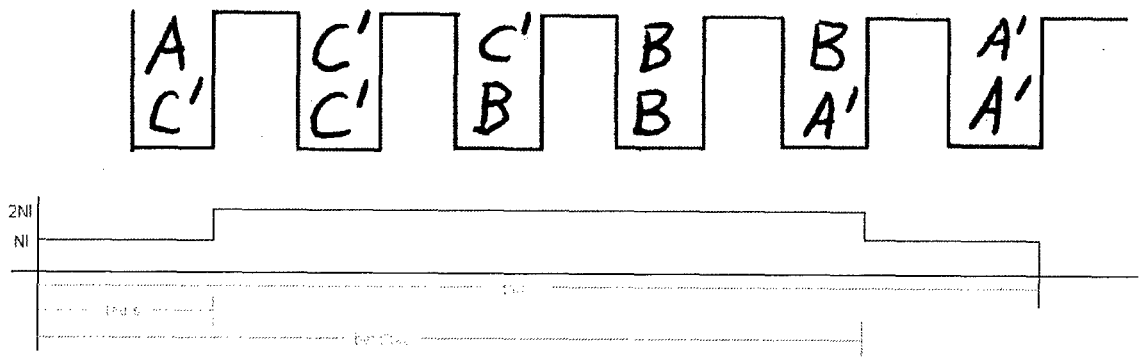

The red graph above indicates the mmf wave due to the A phase of the 5/6 pitch motor winding. This derivation will produce the Fourier coefficients for the A phase wave, and by phase shifting of this wave, waves for an infinite number of phases can be produced. This wave is an odd function, and therefore only the sin function Fourier Coefficients will be required. Beta refers to the degree of short-pitching, in this case 5/6. Tau is the pole pitch in meters. Tau s is the slot pitch, also in meters.

$$f(x) = \sum_{n=1}^{\infty} b_n \cdot \sin(n \cdot k \cdot x)$$

$k = \frac{\pi}{\tau}$ τ = pole pitch

$$b_n = \frac{N \cdot I}{\tau} \cdot \left(\int_0^{\tau_s} \sin\left(n \cdot \frac{\pi}{\tau} \cdot x\right) dx + \int_{\tau_s}^{\beta \cdot \tau} 2 \cdot \sin\left(n \cdot \frac{\pi}{\tau} \cdot x\right) dx + \int_{\beta \cdot \tau}^{\tau} \sin\left(n \cdot \frac{\pi}{\tau} \cdot x\right) dx - \int_{\tau}^{\tau + \tau_s} \sin\left(n \cdot \frac{\pi}{\tau} \cdot x\right) dx - \int_{\tau + \tau_s}^{\tau + \beta \cdot \tau} 2 \cdot \sin\left(n \cdot \frac{\pi}{\tau} \cdot x\right) dx - \int_{\tau + \beta \cdot \tau}^{2 \cdot \tau} \sin\left(n \cdot \frac{\pi}{\tau} \cdot x\right) dx \right)$$

which yields:

$$b_n = \frac{N \cdot I}{n \cdot \pi} \cdot \left[\cos\left[n \cdot \frac{\pi}{\tau} \cdot (\tau + \tau_s)\right] - \cos(n \cdot \pi) + 2 \cdot \cos\left[n \cdot \frac{\pi}{\tau} \cdot (\tau + \beta \cdot \tau)\right] - 2 \cdot \cos\left[n \cdot \frac{\pi}{\tau} \cdot (\tau + \tau_s)\right] + \cos(2 \cdot n \cdot \pi) - \cos\left[n \cdot \frac{\pi}{\tau} \cdot (\tau + \beta \cdot \tau)\right] - \cos\left(n \cdot \frac{\pi}{\tau} \cdot \tau_s\right) + 1 - 2 \cdot \cos(n \cdot \pi \cdot \beta) + 2 \cdot \cos\left(n \cdot \frac{\pi}{\tau} \cdot \tau_s\right) - \cos(n \cdot \pi) + \cos(n \cdot \pi \cdot \beta) \right]$$

The coefficients will remain the same for each phase, but f(x) will be altered in the following way:

$$f(x) = \sum_{n=1}^{\infty} b_n \cdot \sin\left(n \cdot k \cdot x - 2 \cdot \pi \cdot \frac{\text{phase}}{m}\right)$$ where phase = 0 to 2 in a 3 phase system, and m = total # of phases (3 in a 3 phase system)

The mmf contributions of each phase are added together to produce the total spatial distribution of flux as a function of primary position.

THIS PAGE INTENTIONALLY BLANK

Appendix D – Transverse Edge Effect

THIS PAGE INTENTIONALLY BLANK

Appendix D Transverse Edge Effect

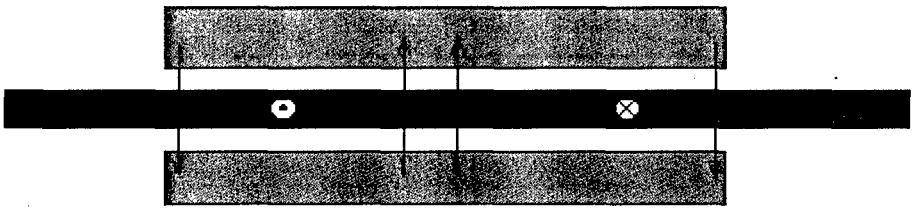

Ampere's Law in the transverse plane yields:

$$g \cdot \frac{dH_y}{dx} = J_{2x} \cdot d \qquad J_{2x} = \text{current density in x-direction}$$

Ampere's Law in the longitudinal plane yields:

$$g \cdot \frac{d}{dx}\left(H_y + H_o\right) = J_p + J_{2z} \cdot d$$

J_p = primary current density

J_{2z} = secondary current density in z-direction

Faraday's Law yields:

$$\frac{dJ_{2z}}{dx} - \frac{dJ_{2x}}{dz} = -j \cdot \omega \cdot s \cdot \mu \cdot \sigma \cdot \left(H_y + H_o\right)$$

H_y = field due to induced secondary currents

H_o = field due to primary current alone

Taking second derivatives and substituting:

$$\frac{g}{d} \cdot \frac{d^2 H_y}{dz^2} - \frac{g}{d} \cdot \frac{d^2 H_y}{dx^2} + \frac{g}{d} \cdot \beta^2 \cdot H_o \cdot e^{j\left(\omega t - \beta x + \frac{\pi}{2}\right)} - j \cdot \frac{1}{d} \cdot \beta \cdot J_m \cdot e^{j(\omega t - \beta x)} = -j \cdot \omega \cdot s \cdot \mu \cdot \sigma \cdot \left(H_y + H_o\right)$$

recognizing that:

$$H_y = H(z) \cdot e^{j(\omega t - \beta x + \delta)} \qquad H_o = \frac{J_m}{\beta} \cdot e^{j\left(\omega t - \beta x + \frac{\pi}{2}\right)}$$

β = wavenumber (π/τ)

s = slip

and assuming that the machine is nearly at synchronous speed:

$$\delta = \frac{\pi}{2}$$

Yields the final equation:

$$\frac{d^2 H(z)}{dz^2} - \left(\beta + \frac{d}{g}\cdot\omega\cdot s\cdot\mu\cdot\sigma\right)\cdot H(z) = \frac{d}{g}\cdot\omega\cdot s\cdot\mu\cdot\sigma\cdot\frac{1}{\beta g}\cdot J_m$$

particular solution:

$$H(z) = \frac{\frac{d}{g}\cdot\omega\cdot s\cdot\mu\cdot\sigma\cdot\frac{1}{\beta g}}{\beta + \frac{d}{g}\cdot\omega\cdot s\cdot\mu\cdot\sigma}\cdot J_m$$

homogeneous solution:

$$H(z) = Be^{\alpha z} + Ce^{-\alpha z}$$

$$\alpha = \sqrt{\beta + \frac{d}{g}\cdot\omega\cdot s\cdot\mu\cdot\sigma} \quad \text{and} \quad \alpha = -\sqrt{\beta + \frac{d}{g}\cdot\omega\cdot s\cdot\mu\cdot\sigma}$$

total solution:

$$H(z) = \frac{\frac{d}{g}\cdot\omega\cdot s\cdot\mu\cdot\sigma\cdot\frac{1}{\beta g}}{\beta + \frac{d}{g}\cdot\omega\cdot s\cdot\mu\cdot\sigma}\cdot J_m + Be^{\alpha\cdot z} + Ce^{-\alpha\cdot z}$$

This solution assumes the the z-coordinate is centered in the center of the primary stack.

Appendix E – Equivalent Circuit Parameters

THIS PAGE INTENTIONALLY BLANK

Appendix E Equivalent Circuit

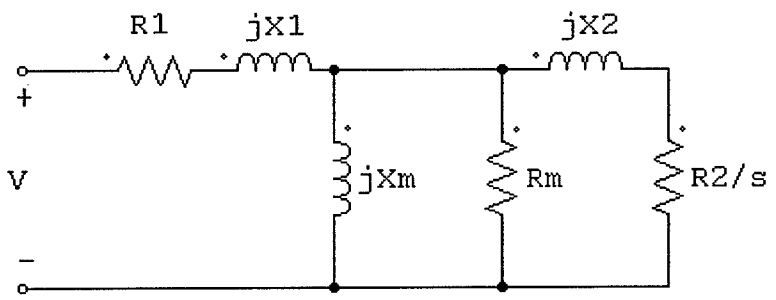

$X2 = 0$ $Rm = \infty$

$$R1 = \left[\left[\frac{12 \cdot N^2 \cdot (\text{depth} + \text{width}) \cdot (\text{statorpoles})}{\sigma_{Cu} \cdot \tau \cdot t \cdot \lambda} + \frac{4 \cdot N}{\sigma_{Cu} \cdot t} \cdot \text{statorpoles}\right] \cdot 1.5 + R_{line}\right]$$

$$R2 = \left[\frac{12 \cdot N^2 \cdot (a_e) \cdot \text{rotorpoles}}{\sigma_{Al} \cdot \tau \cdot d \cdot K_{transverse}} + \frac{2 \cdot \frac{\tau}{3} \cdot \text{rotorpoles}}{\sigma_{Al} \cdot \frac{\text{overhang}}{2} \cdot d \cdot K_{transverse}}\right] \cdot 1$$

$$K_{transverse} = 1 - \frac{\tanh\left(.5 \cdot \frac{\pi}{\tau} \cdot \text{depth}\right)}{.5 \cdot \frac{\pi}{\tau} \cdot \text{depth} \cdot \left(1 + \tanh\left(.5 \cdot \frac{\pi}{\tau} \cdot \text{depth}\right) \cdot \tanh\left(\frac{\pi}{\tau} \cdot c\right)\right)}$$

$$M = \frac{\mu_0 \cdot \tau \cdot N^2 \cdot \text{depth} \cdot (\text{rotorpoles}) \cdot 2}{g}$$

$$Ltot = M \cdot \frac{\text{statorpoles}}{\text{rotorpoles}} \cdot 1.2$$

$$L1 = L_{tot} - M$$

τ = pole pitch (m)

σ_c = copper conductivity

σ_{Al} = Aluminum conductivity

N = turns per pole per phase per side

depth = depth of primary stack (m)

width = width of primary stack (m)

statorpoles = # of active stator poles

rotorpoles = # of active rotor poles

g = magnetic airgap (m)

overhang = shuttle overhang over primary depth (m)

a_e = equivalent primary stack height (m)

t = primary winding thickness (m)

$K_{transverse}$ = transverse edge effect correction factor

d = shuttle thickness (m)

c = height of secondary conducting sheet

μ_0 = permeability of back iron

Appendix F – Simulink Models

THIS PAGE INTENTIONALLY BLANK

Volts Per Hertz Controller

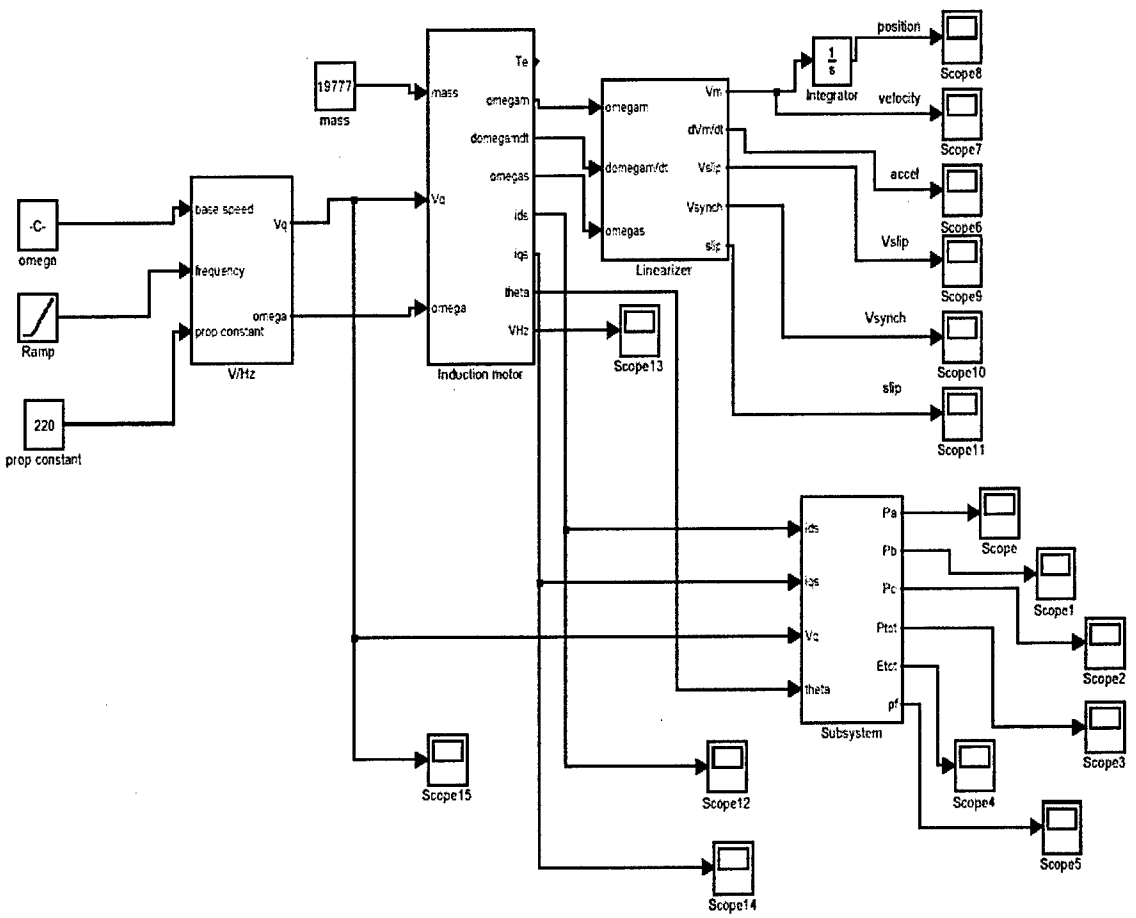

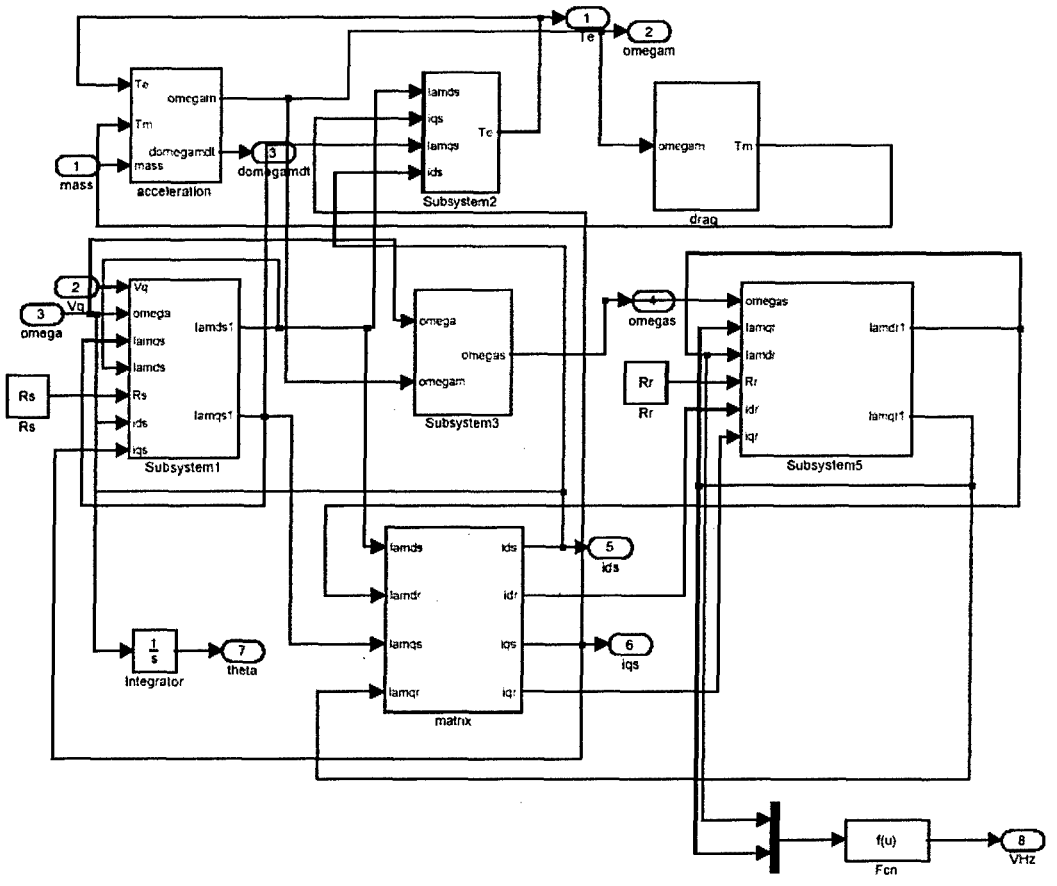
1
Te
2
omegam
Te
omegam
Tm
domegamdt
mass
acceleration
3
domegamdt
1
mass
lamds
iqs
lamqs
ids
Te
Subsystem2
omegam
Tm
drag
2
Vq
3
omega
Rs
Rs
Vq
omega
lamds
lamqs
Rs
ids
iqs
lamds1
lamqs1
Subsystem1
omega
omegas
omegam
Subsystem3
4
omegas
Rr
Rr
omegas
lamqr
lamdr
Rr
idr
iqr
lamdr1
lamqr1
Subsystem5
lamds
lamdr
lamqs
lamqr
ids
idr
iqs
iqr
matrix
5
ids
6
iqs
1
s
integrator
7
theta
f(u)
Fcn
8
VHz

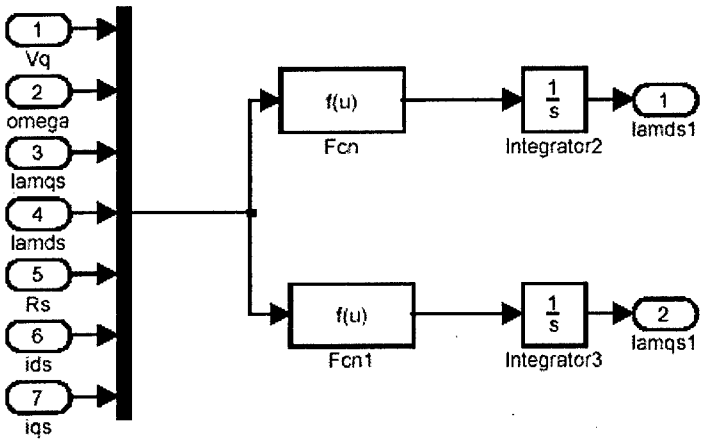
1
Vq
2
omega
3
lamqs
4
lamds
5
Rs
6
ids
7
iqs
f(u)
Fcn
1
s
Integrator2
1
lamds1
f(u)
Fcn1
1
s
Integrator3
2
lamqs1

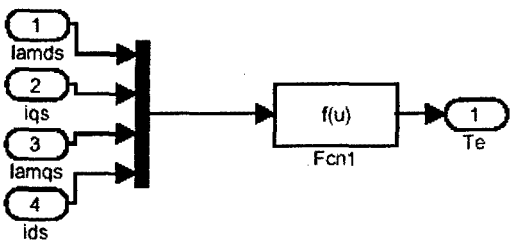
1
lamds
2
iqs
3
lamqs
4
ids
f(u)
Fcn1
1
Te

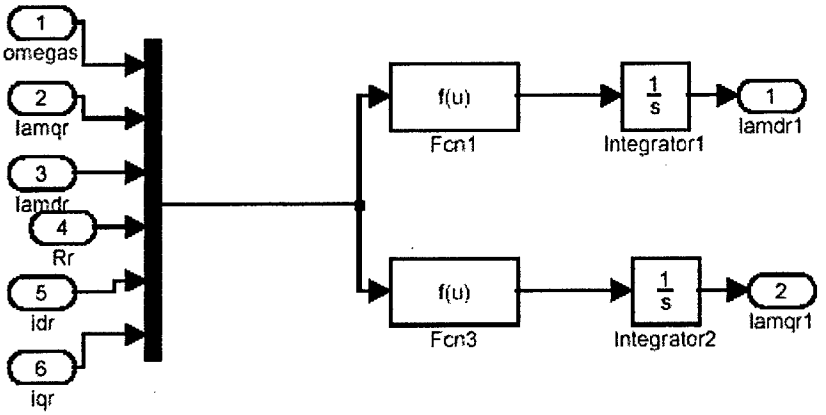
1
omegas
2
lamqr
3
lamdr
4
Rr
5
idr
6
iqr
f(u)
Fcn1
1
s
Integrator1
1
lamdr1
f(u)
Fcn3
1
s
Integrator2
2
lamqr1

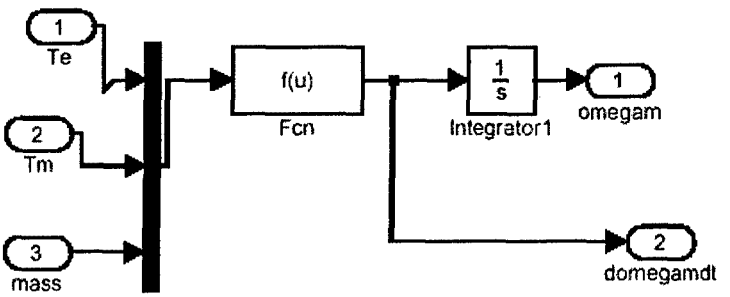
1
Te
2
Tm
3
mass
f(u)
Fcn
1
s
Integrator1
1
omegam
2
domegamdt

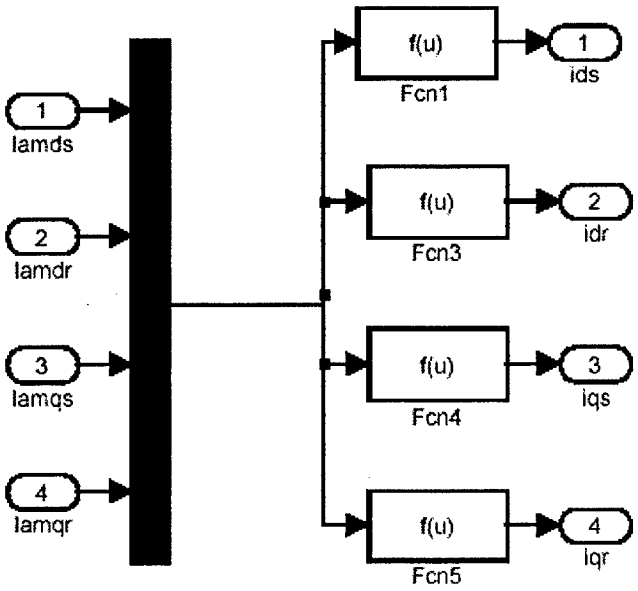
1
lamds
2
lamdr
3
lamqs
4
lamqr
f(u)
Fcn1
1
ids
f(u)
Fcn3
2
idr
f(u)
Fcn4
3
iqs
f(u)
Fcn5
4
iqr

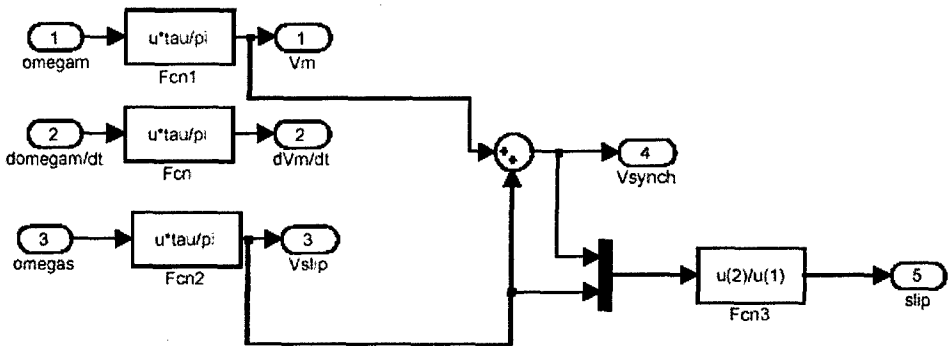
1
omegam
u*tau/pi
Fcn1
1
Vm
2
domegam/dt
u*tau/pi
Fcn
2
dVm/dt
3
omegas
u*tau/pi
Fcn2
3
Vslip
4
Vsynch
u(2)/u(1)
Fcn3
5
slip

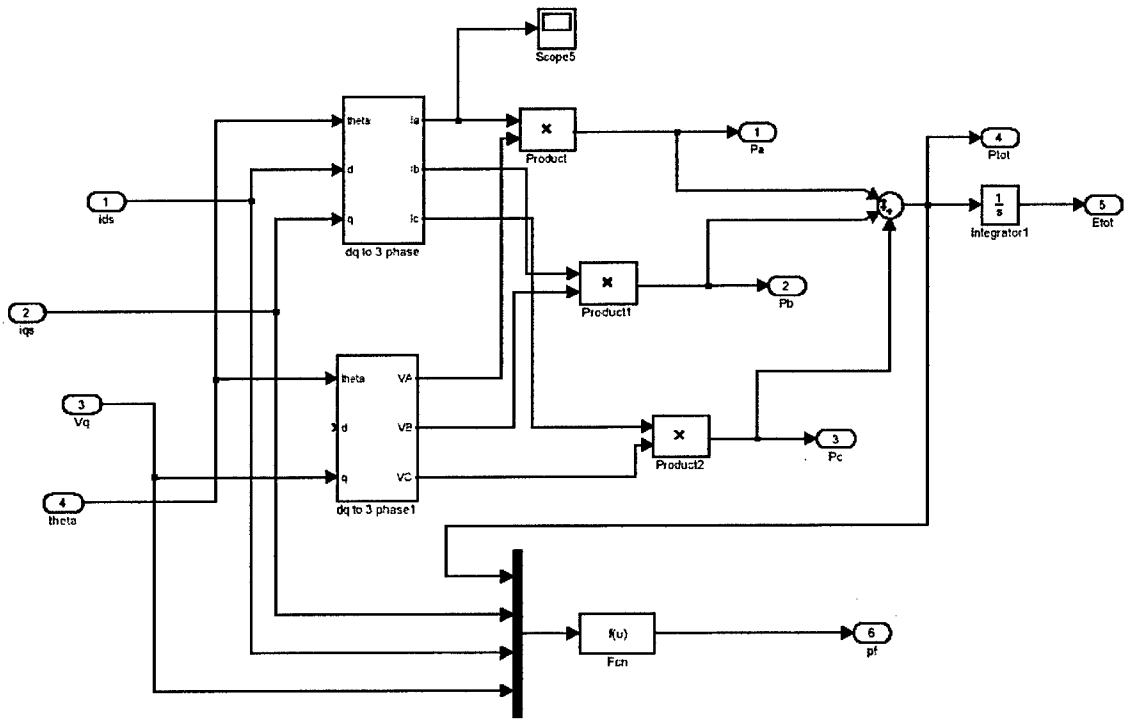
Scope5
theta
d
q
ia
ib
ic
dq to 3 phase
Product
1
Pa
4
Ptot
1
ids
Product1
2
Pb
2
iqs
1
s
Integrator1
5
Etot
theta
VA
VB
VC
dq to 3 phase1
3
Vq
Product2
3
Pc
4
theta
f(u)
Fcn
6
pf

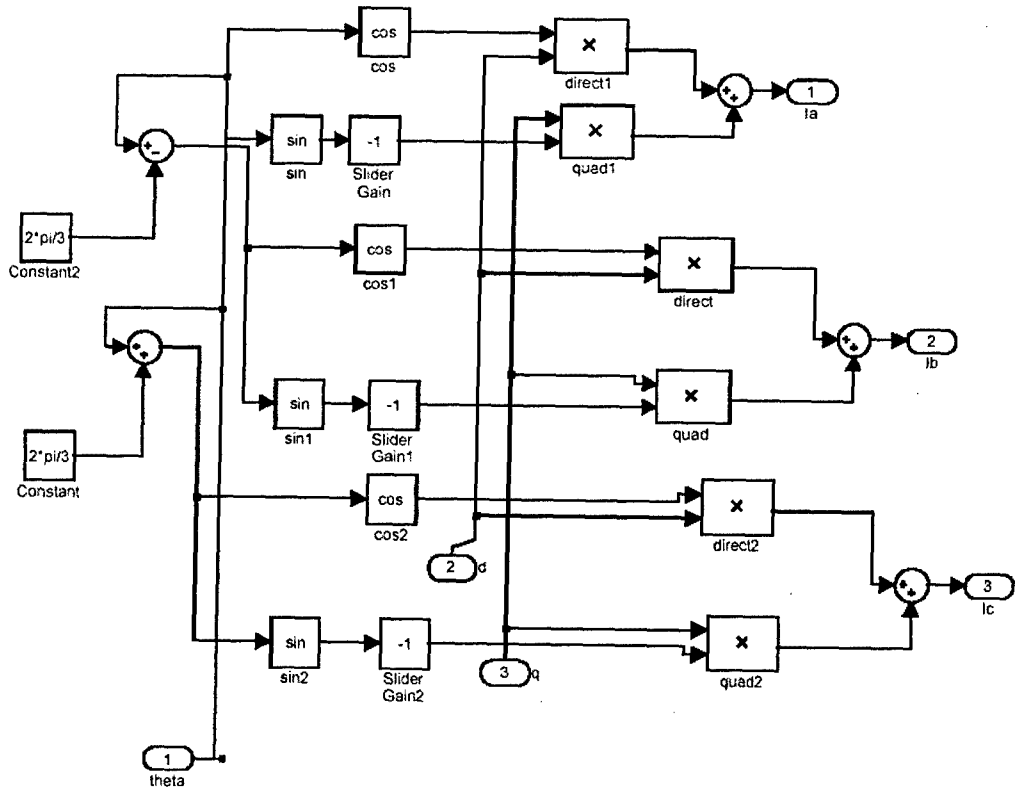
cos
cos
direct1
1
Ia
sin
sin
-1
Slider
Gain
quad1
2*pi/3
Constant2
cos
cos1
direct
2
Ib
sin
sin1
-1
Slider
Gain1
quad
2*pi/3
Constant
cos
cos2
direct2
2
d
3
Ic
sin
sin2
-1
Slider
Gain2
3
q
quad2
1
theta

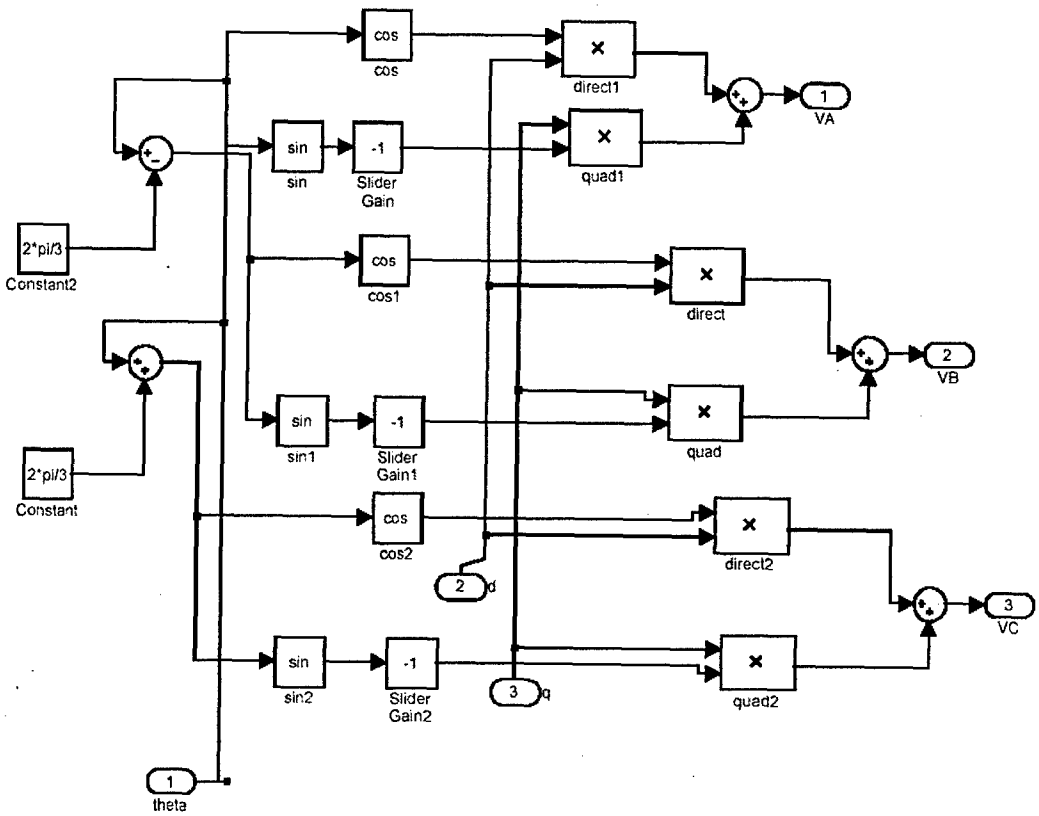
cos
cos
direct1
1
VA
sin
sin
-1
Slider
Gain
quad1
2*pi/3
Constant2
cos
cos1
direct
2
VB
sin
sin1
-1
Slider
Gain1
quad
2*pi/3
Constant
cos
cos2
direct2
2
d
3
VC
sin
sin2
-1
Slider
Gain2
3
q
quad2
1
theta

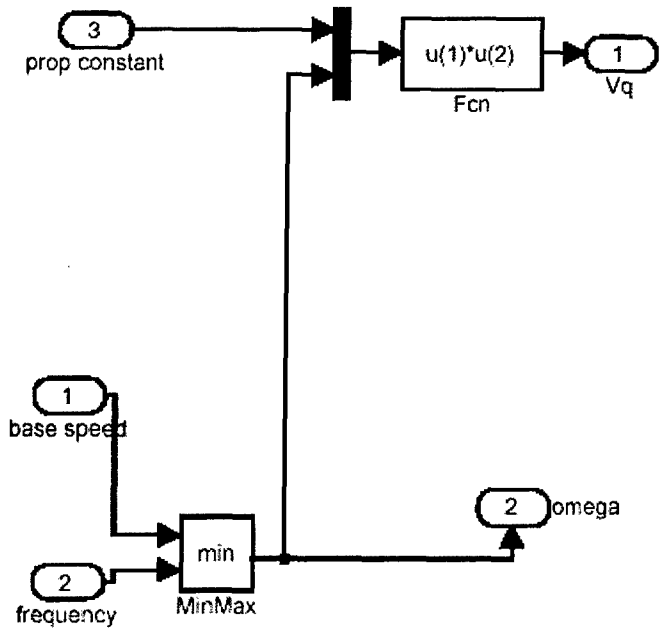
3
prop constant
u(1)*u(2)
Fcn
1
Vq
1
base speed
2
omega
min
MinMax
2
frequency

Field-Oriented Controller

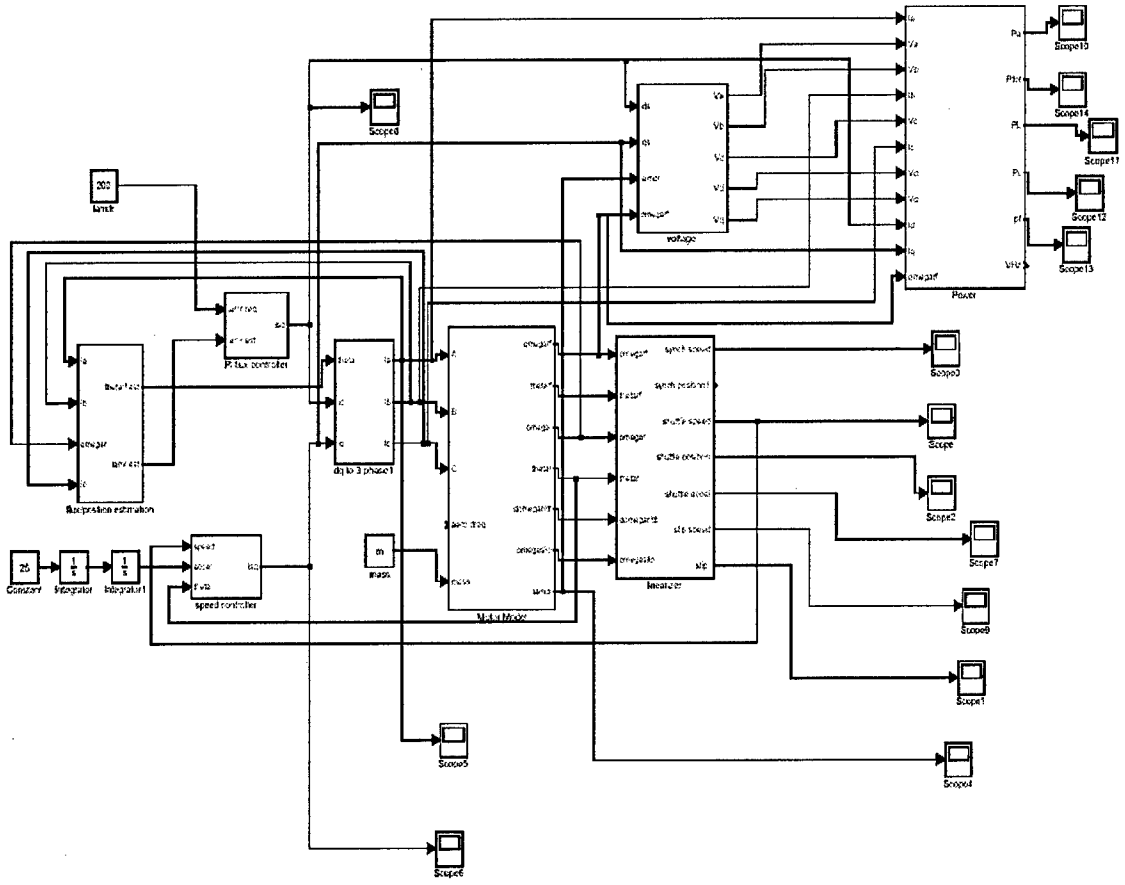

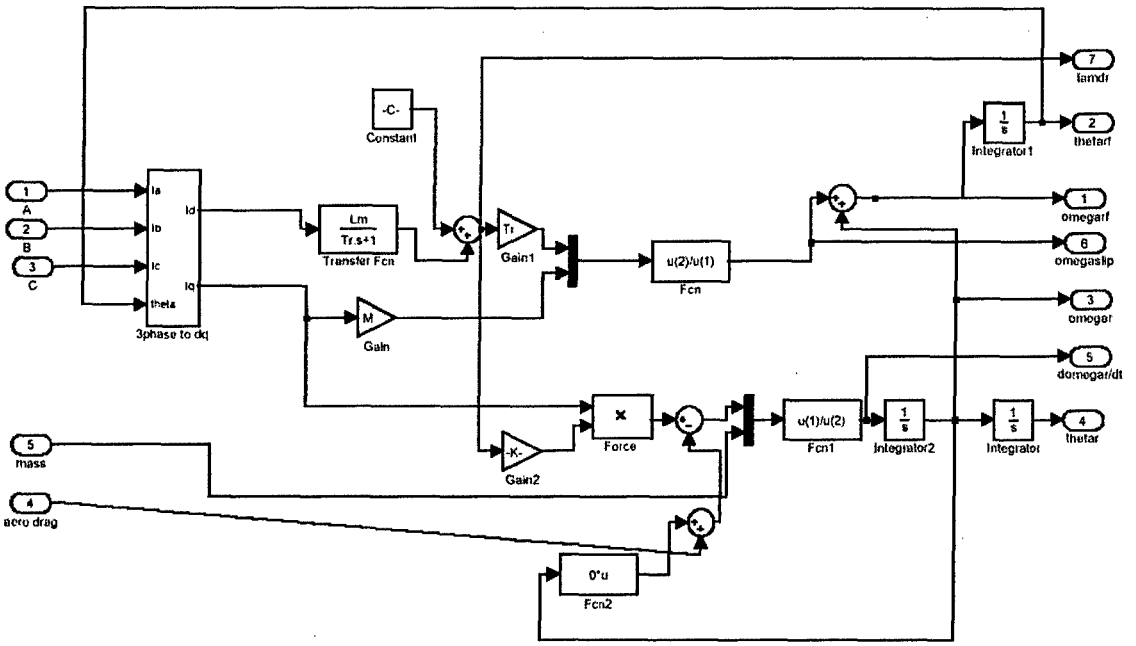
1
A
2
B
3
C
Ia
Ib
Ic
theta
Id
Iq
3phase to dq
Lm
Tr.s+1
Transfer Fcn
-C-
Constant
Tr
Gain1
M
Gain
u(2)/u(1)
Fcn
7
lamdr
2
thetarf
1
omegarf
6
omegaslip
3
omegar
5
domegar/dt
4
thetar
1/s
Integrator1
1/s
Integrator
1/s
Integrator2
u(1)/u(2)
Fcn1
-K-
Gain2
Force
5
mass
4
aero drag
0*u
Fcn2

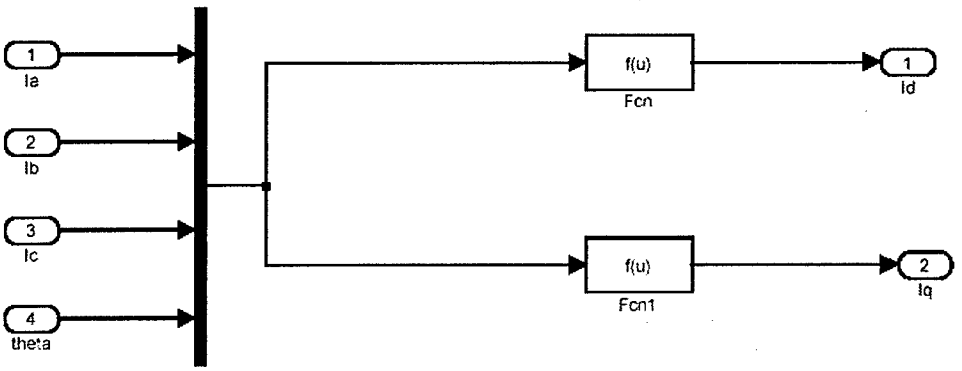
1
Ia
2
Ib
3
Ic
4
theta
f(u)
Fcn
1
Id
f(u)
Fcn1
2
Iq

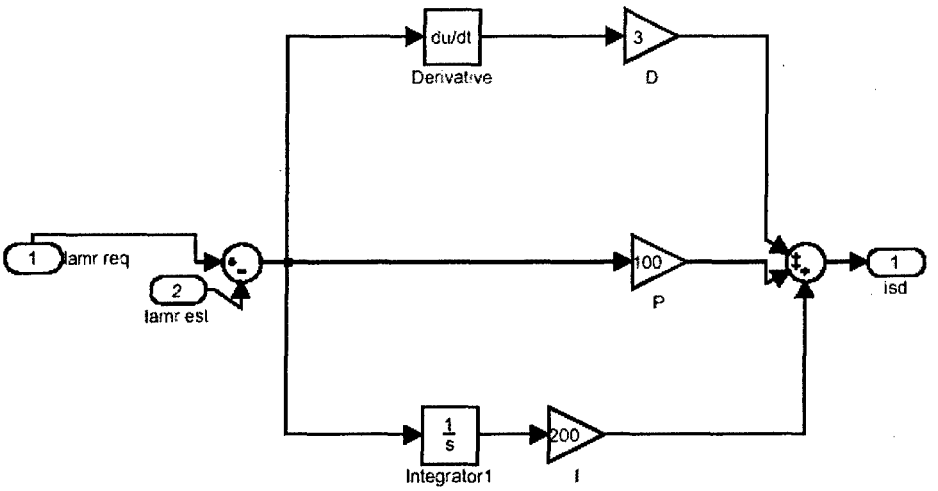
du/dt
Derivative
3
D
1
lamr req
2
lamr est
100
P
1
isd
1
s
Integrator1
200
I

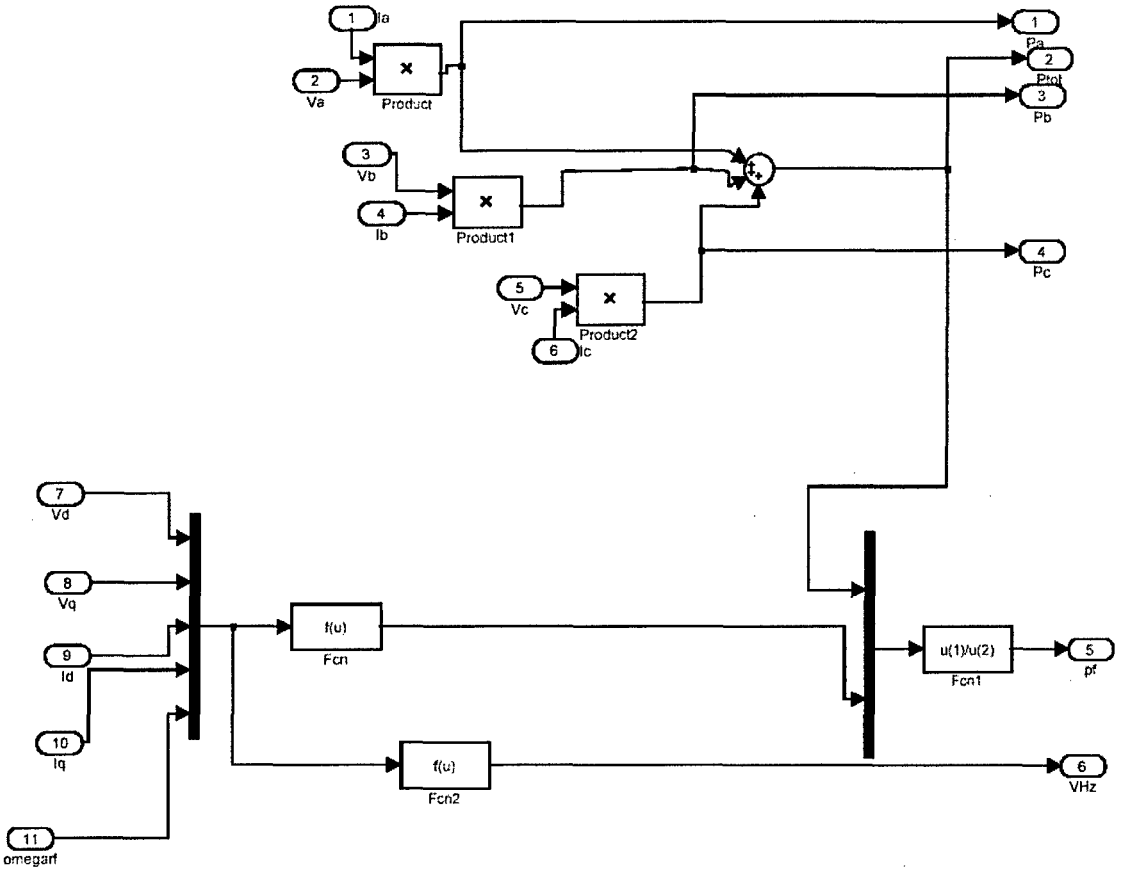
1
Ia
2
Va
Product
1
Pa
2
Ptot
3
Pb
3
Vb
4
Ib
Product1
4
Pc
5
Vc
Product2
6
Ic
7
Vd
8
Vq
9
Id
10
Iq
11
omegarf
f(u)
Fcn
f(u)
Fcn2
u(1)/u(2)
Fcn1
5
pf
6
VHz

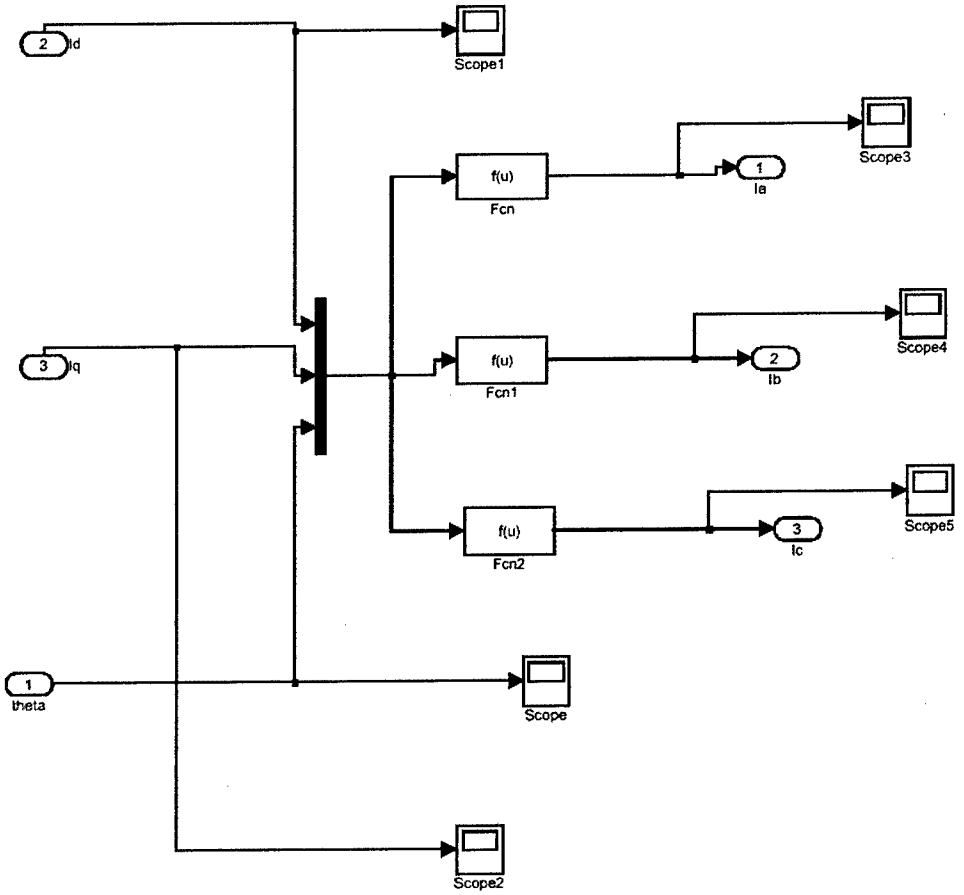
2
Id
Scope1
f(u)
Fcn
1
Ia
Scope3
3
Iq
f(u)
Fcn1
2
Ib
Scope4
f(u)
Fcn2
3
Ic
Scope5
1
theta
Scope
Scope2

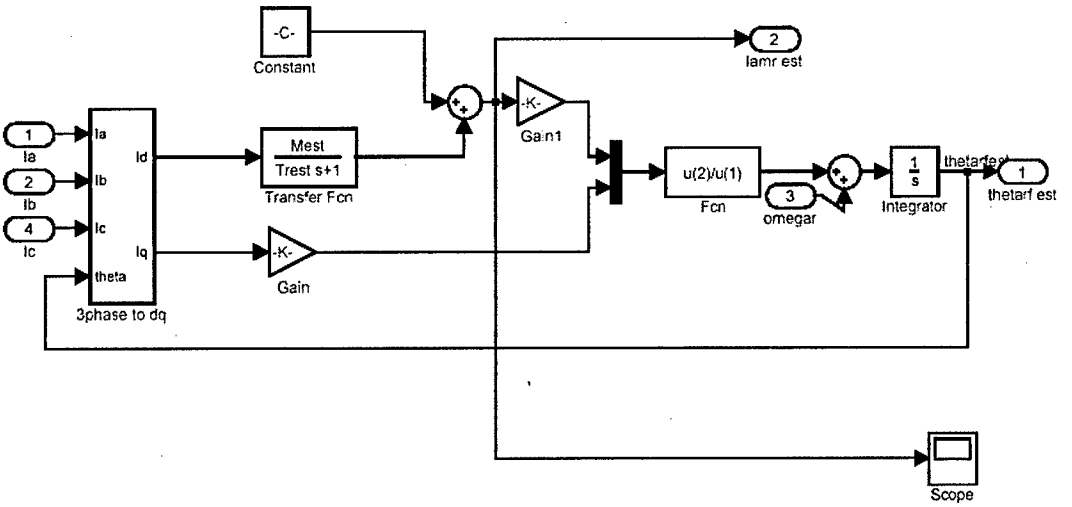
-C-
Constant
2
lamr est
-K-
Gain1
1
Ia
2
Ib
4
Ic
Ia
Ib
Ic
theta
Id
Iq
3phase to dq
Mest
Trest s+1
Transfer Fcn
-K-
Gain
u(2)/u(1)
Fcn
3
omegar
1
s
Integrator
thetarf est
1
thetarf est
Scope

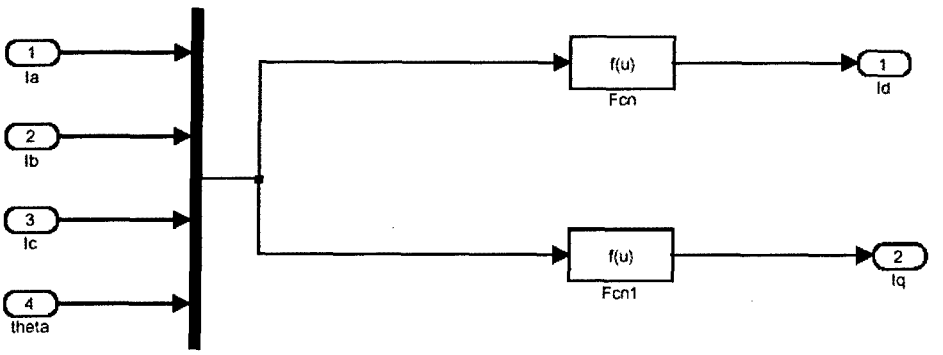
1
Ia
2
Ib
3
Ic
4
theta
f(u)
Fcn
f(u)
Fcn1
1
Id
2
Iq

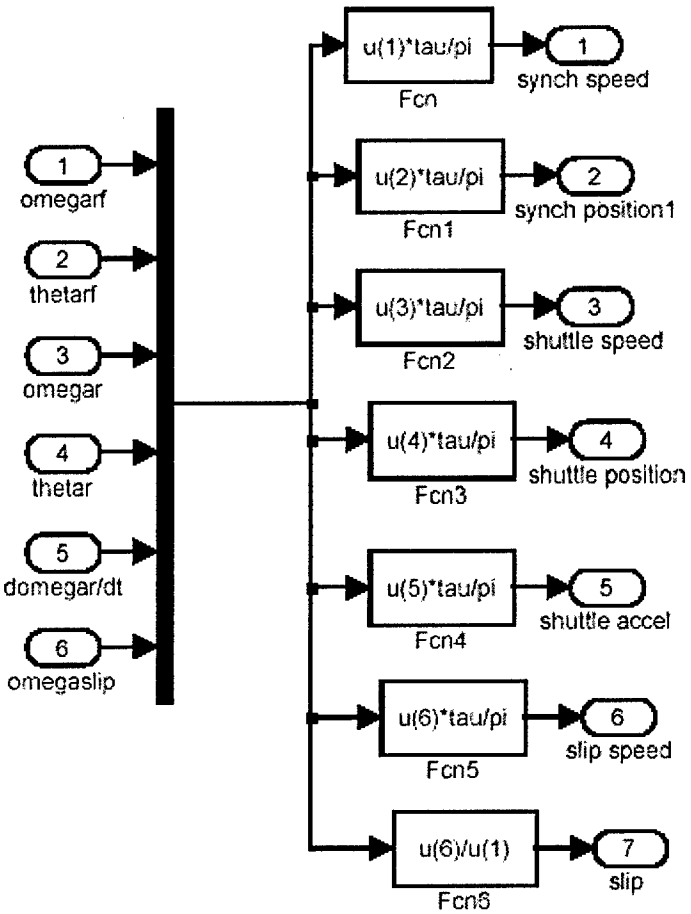
1
omegarf
2
thetarf
3
omegar
4
thetar
5
domegar/dt
6
omegaslip
u(1)*tau/pi
Fcn
1
synch speed
u(2)*tau/pi
Fcn1
2
synch position1
u(3)*tau/pi
Fcn2
3
shuttle speed
u(4)*tau/pi
Fcn3
4
shuttle position
u(5)*tau/pi
Fcn4
5
shuttle accel
u(6)*tau/pi
Fcn5
6
slip speed
u(6)/u(1)
Fcn6
7
slip

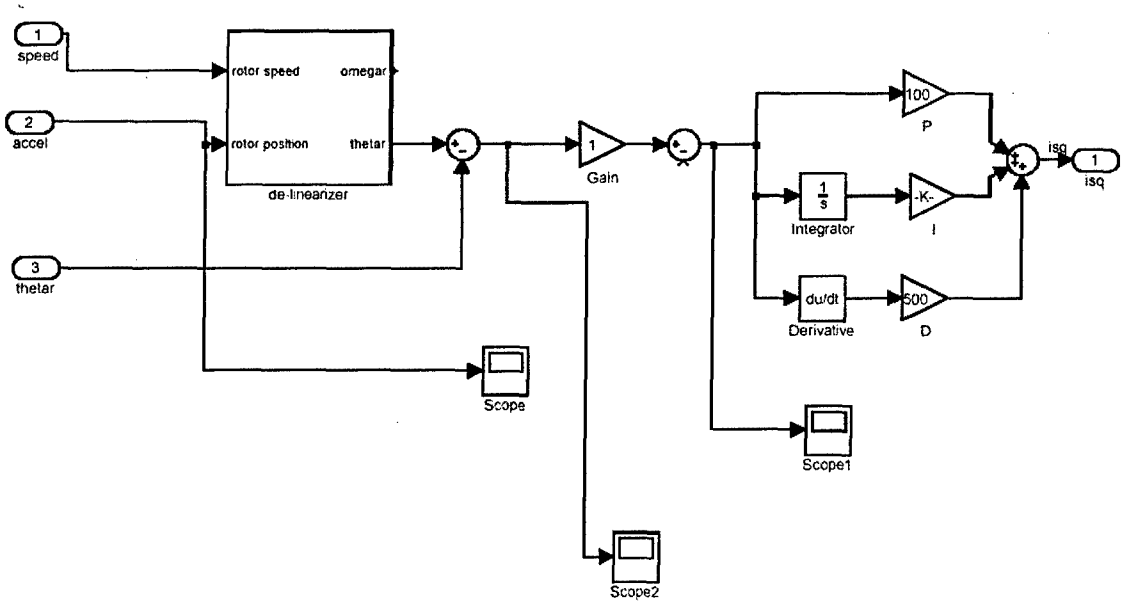
1
speed
2
accel
3
thetar
rotor speed
omegar
rotor position
thetar
de-linearizer
Scope
1
Gain
Scope2
100
P
1
s
Integrator
-K-
I
du/dt
Derivative
500
D
Scope1
isq
1
isq

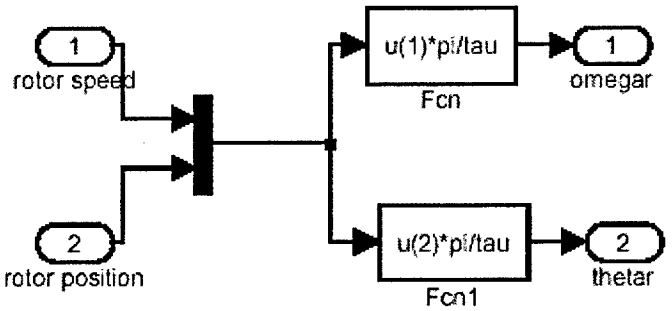
1
rotor speed
2
rotor position
u(1)*pi/tau
Fcn
u(2)*pi/tau
Fcn1
1
omegar
2
thetar

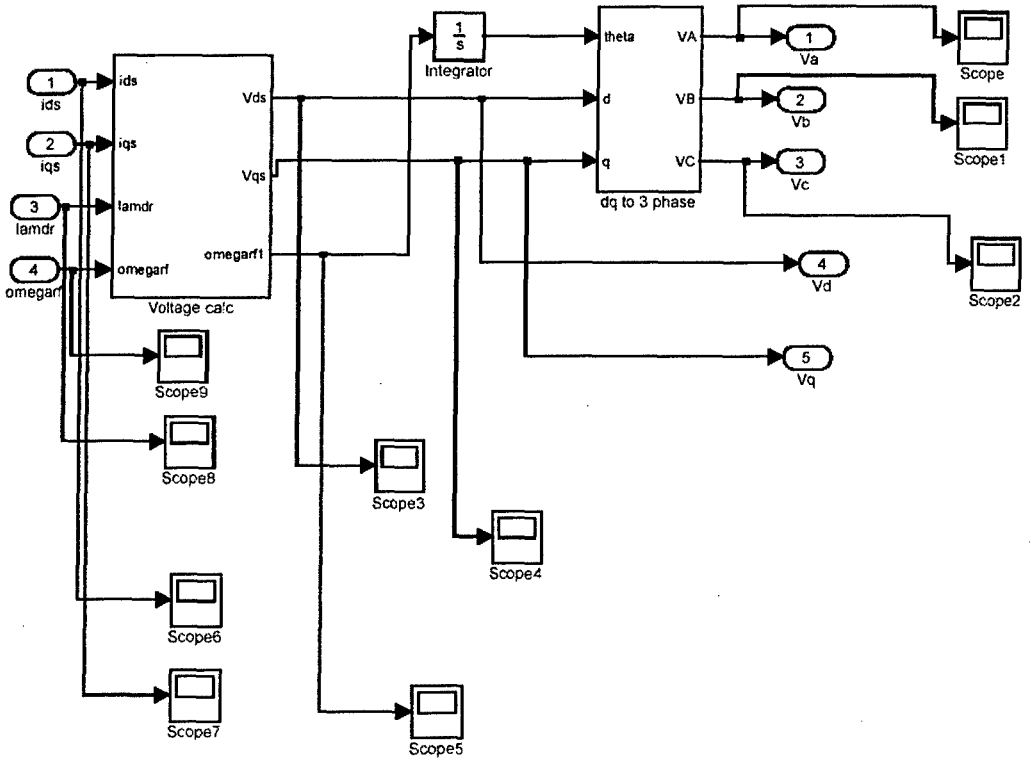
1
ids
2
iqs
3
lamdr
4
omegarf
ids
iqs
lamdr
omegarf
Vds
Vqs
omegarf1
Voltage calc
1
s
Integrator
theta
d
q
VA
VB
VC
dq to 3 phase
1
Va
2
Vb
3
Vc
4
Vd
5
Vq
Scope
Scope1
Scope2
Scope3
Scope4
Scope5
Scope6
Scope7
Scope8
Scope9

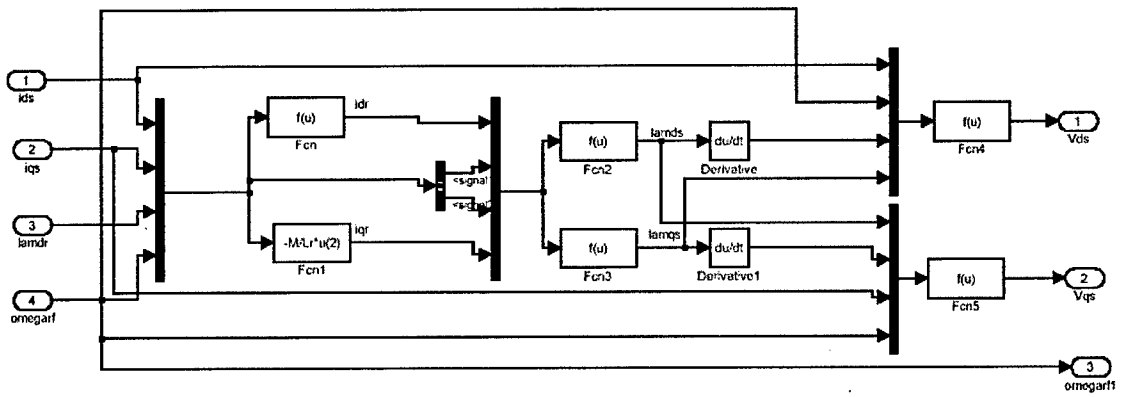
1
ids
2
iqs
3
lamdr
4
omegarf
f(u)
Fcn
idr
-M/Lr*u(2)
Fcn1
iqr
f(u)
Fcn2
lamds
du/dt
Derivative
f(u)
Fcn3
lamqs
du/dt
Derivative1
f(u)
Fcn4
1
Vds
f(u)
Fcn5
2
Vqs
3
omegarf1

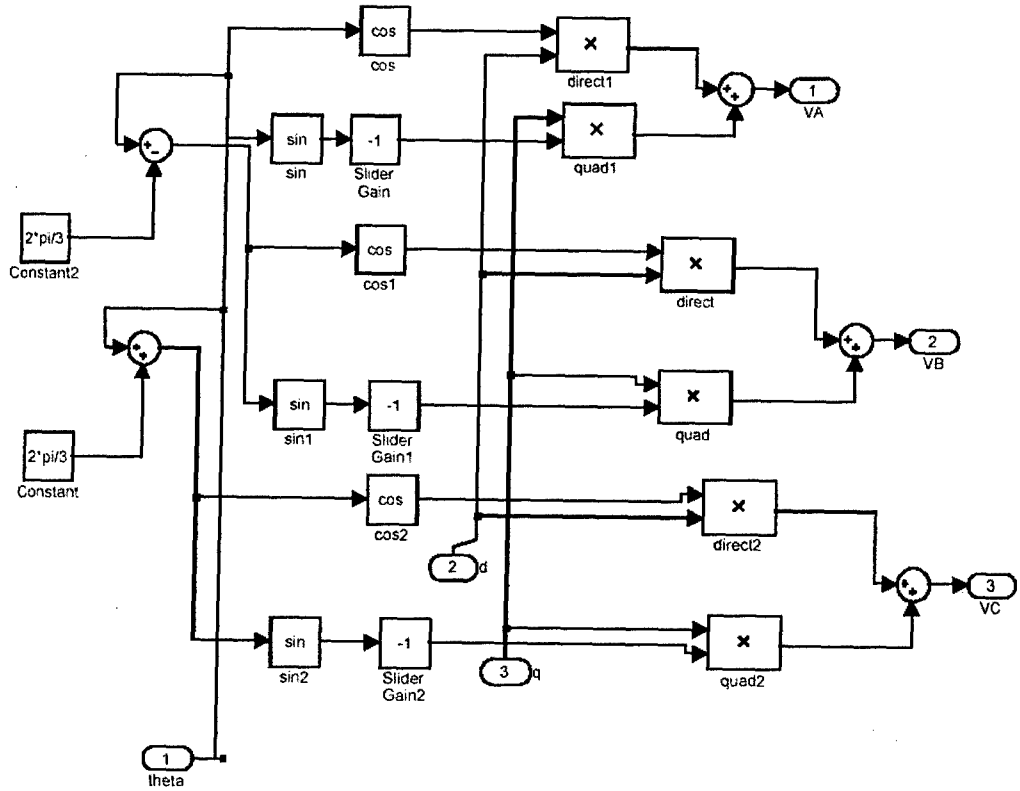
cos
cos
direct1
1
VA
sin
sin
-1
Slider
Gain
quad1
2*pi/3
Constant2
cos
cos1
direct
2
VB
sin
sin1
-1
Slider
Gain1
quad
2*pi/3
Constant
cos
cos2
direct2
2
d
3
VC
sin
sin2
-1
Slider
Gain2
3
q
quad2
1
theta

Appendix G – Motor Sizing

THIS PAGE INTENTIONALLY BLANK

```
clear;

mu=pi*4e-7;
g=9e-2;          %airgap in meters
tau=.385;           %pole pitch in meters
a=10*tau;        %rotor length in m
k=pi/tau;
Ko=190e3;
w=314;          %field frequency
L=1.25;            %depth of primary stack
Vs=(tau/pi)*w;     %field velocity
% V=Vs*.5;             %shuttle velocity
sigmar=2.5e7*2e-2*.5*.7;  %rotor surface conductivity Al 2cm thick, .5 for ↙
symmetry, .70 for transverse edge effect
t=0;

for m=1:100
    slip(m)=m/1000;
    V=(1-slip(m))*Vs;
    alpha=(i*2*mu*(pi/tau)*sigmar*(Vs-V)/g)^.5;
    Co=(i*2*mu*Ko/g)/(i*2*mu*sigmar*(Vs-V)/g-(pi/tau));
    for n=1:1001
        dx=a/1000;
        x(n)=(n-1)*a/1000;
        B1=-i*2*mu*tau/(pi*g)*Ko;
        B2=-i*2*mu*tau/(pi*g)*Ko*exp(i*pi/tau*a);
        C2=(B2+(exp(i*alpha*a)-exp(i*pi/tau*a))*Co-B1*exp(i*alpha*a))/(exp(↙
-i*alpha*a)-exp(i*alpha*a));
        C1=B1-Co-C2;
        Bo(n)=Co*exp(i*(pi/tau)*x(n))+C1*exp(i*alpha*x(n))+C2*exp(-i*alpha*↙
x(n));
        By(n)=Bo(n)*exp(-i*(pi/tau)*(Vs-V)*t);
        Bybackiron(n)=-i*mu*(tau/pi)*(Ko/g)*exp(i*(pi/tau)*(x(n)-(Vs-V)*t))↙
;
        dKr(n)=-By(n)*i*(pi/tau)*sigmar*(Vs-V);
        C3=i*sigmar/a*(Vs-V)*exp(-i*(pi/tau)*(Vs-V)*t)*((1-exp(i*(pi/tau)*a↙
))*(tau/pi)^2*Co+(1-exp(i*alpha*a))*(1/alpha)^2*C1+(1-exp(-i*alpha*a))*(1/a↙
lpha)^2*C2);
        Kr(n)=-i*(pi/tau)*sigmar*(Vs-V)*exp(-i*(pi/tau)*(Vs-V)*t)*(-i*(tau/↙
pi)*Co*exp(i*(pi/tau)*x(n))-i/alpha*C1*exp(i*alpha*x(n))+i/alpha*C2*exp(-i*↙
alpha*x(n)))+C3;
        Bonew(n)=Co*exp(i*(pi/tau)*x(n));
        Bynew(n)=Bonew(n)*exp(-i*(pi/tau)*(Vs-V)*t);
        Krnew(n)=-i*(pi/tau)*sigmar*(Vs-V)*exp(-i*(pi/tau)*(Vs-V)*t)*-i*(ta↙
u/pi)*Co*exp(i*(pi/tau)*x(n));
        if n==1
            sum(m)=.5*real(Kr(n)*conj(By(n)));
          sumnew(m)=.5*real(Krnew(n)*conj(Bynew(n)));
        elseif n==1001
```

```
            sum(m)=sum(m)+.5*real(Kr(n)*conj(By(n)));
            sumnew(m)=sumnew(m)+.5*real(Krnew(n)*conj(Bynew(n)));
        else
            sum(m)=sum(m)+real(Kr(n)*conj(By(n)));
            sumnew(m)=sumnew(m)+real(Krnew(n)*conj(Bynew(n)));
        end

    end
end


sumtot=-2*.5*sum*dx*L;          %with end effect, factor of 2 for both sides
sumtotnew=-2*.5*sumnew*dx*L;    %no end effect
mag=max(sumtotnew);
sumtot=sumtot/mag;          %normalizing
sumtotnew=sumtotnew/mag;

plot(slip,sumtot);
hold;
plot(slip,sumtotnew);

legend('with end effect','without end effect',-1);
title('Force vs. Slip')
ylabel('Normalized Force')
xlabel('Normalized Slip')
% plot(x,abs(Kr));
```

```
function [R2]=secondary(depth,N,thick,tau,a,sigmaei)

R2=12*N^2*(1.2*depth)*a/(sigmaei*tau*thick/2);
```

```
function [L,M,Leak]=inductance(mu,tau,N,depth,active,g)

L=(mu*tau*N^2*depth*active)/g;      %active=# primary active pole pairs,
M=(mu*tau*N^2*depth*(active-1))/g;          %p=# rotor poles
Leak=(L-M);
```

```
function[Effmax,opslip,Itotop,Rr,Leak,Mut,Al,gap]=eff(R1,tau,depth,flux,Vfi↙
nal,N,sigmaei,active)

mu=pi*4e-7;
g=9e-2;
Althick=2e-2;

while (1==1)


[R2]=secondary(depth,N,Althick,tau,active,sigmaei);
[L,M,L1]=inductance(mu,tau,N,depth,active,g);


for n=1:10
    for slip=1:1000

        s(n,slip)=slip/1001;
        omega(n,slip)=(n/10)*Vfinal*(pi/tau)/(1-s(n,slip));
        speed(n,slip)=Vfinal*(1-s(n,slip));
        X1(n,slip)=omega(n,slip)*L1;
        Xm(n,slip)=omega(n,slip)*M;
        f(n,slip)=omega(n,slip)/(2*pi);
        V(n,slip)=flux*f(n,slip);
        par=j*R2*Xm(n,slip)/(R2+j*s(n,slip)*Xm(n,slip));
        Itot(n,slip)=V(n,slip)/(R1+j*X1(n,slip)+par);
        I2(n,slip)=Itot(n,slip)*j*Xm(n,slip)/(R2/s(n,slip)+j*Xm(n,slip));
        F(n,slip)=3*(pi/(tau*omega(n,slip)))*abs(I2(n,slip))^2*R2/s(n,slip)↙
;
        Power(n,slip)=F(n,slip)*speed(n,slip);
        Powerloss1(n,slip)=abs(Itot(n,slip))^2*R1;
        Powerloss2(n,slip)=abs(I2(n,slip))^2*R2;
        Efficiency(n,slip)=Power(n,slip)/(Power(n,slip)+Powerloss1(n,slip)+↙
Powerloss2(n,slip));
        Fraction(n,slip)=abs(I2(n,slip))/abs(Itot(n,slip));
    end

end

maxF=max(F(10,:));
if maxF >= 1.43e6
    break;
end

Althick=Althick+.1e-2;
g=g+.1e-2;

end
```

```
[x]=find(F(10,:)==maxF);

for index=x:-1:1
    if F(10,index)<=1.3e6
        break;
    end
end

Effmax=Efficiency(10,index);
opslip=s(10,index);
Itotop=Itot(10,index);
Rr=R2;
Leak=L1;
Mut=M;
Al=Althick;
gap=g;
```

```
function [temprise, Endiss, Jmaxbelt,Ko]=temp(Iphase,tau,depth,width,active,N)
pf=.4;                                  %packing factor

w=tau/3;
tw=2e-2;
sigmacu=5.7e7;
area=w*tw*pf;

R=(1/sigmacu)*N*2*active*(depth+width)/(area);
Power=Iphase^2*R;
Energy=Iphase^2*R*.6;                   % 2 for RMS
Cumass=8920*10^3*(tau/3)*tw*depth;      %Cu mass in grams
Cuspecheat=.385;                         %J/(C*g)
deltaT=Energy/(Cumass*Cuspecheat);  %in C

temprise=deltaT;
diameter=0;
Endiss=Energy;
Jmaxbelt=Iphase/(area/pf);

Ko=Iphase*N/(tau/3);
```

DSLIM Motor Sizing Worksheet

$depth := .45m$ $\mu_0 := 4\cdot\pi\cdot 10^{-7}\frac{H}{m}$ $t := 2\cdot 10^{-2}m$ $V_{final} := 100\frac{m}{s}$

$\tau := .385m$ $g := 9\cdot 10^{-2}m$ $\lambda := .3$ $rotorlength := 9m$ $overhang := .5m$

$rotorpoles := round\left(\frac{rotorlength}{\tau}, 0\right)$ $a_e := depth\cdot 1.2$ $d := \frac{2\cdot 10^{-2}}{2}m$ $p := 10$ poles per stator section

$slip := .046$ $THD := 10$

$rotorpoles = 23$ $a_e = 0.54m$ $thickness_{rotor} := d\cdot 2$

$height_{rotor} := a_e + overhang$ $length_{section} := p\cdot\tau$ $length_{section} = 3.85m$

$\sigma_{Cu} := 5.7\cdot 10^{7}\frac{siemens}{m}$ $\sigma_{Al} := 2.5\cdot 10^{7}\frac{siemens}{m}$

$width := \frac{\tau}{3.5}$ $N := 3$ $B_{start} := 68volt\cdot s$ $totalsections := round\left(\frac{100m}{\tau\cdot p + .02m}, 0\right)$

$activesections := round\left(\frac{rotorpoles}{p} + 1, 0\right)$ $activesections = 3$ $height_{rotor} = 1.04m$

$totalsections = 26$ $statorpoles := activesections\cdot p$ $statorpoles = 30$

$R_{line} := \left(\frac{100m}{\sigma_{Cu}\cdot\frac{\tau}{3}\cdot t\cdot\lambda}\right)\cdot 1.5$ $R_{line} = 3.418\times 10^{-3}\Omega$ $thickness_{rotor} = 0.02m$

$$M := \frac{\mu_0 \cdot \tau \cdot N^2 \cdot depth \cdot (rotorpoles) \cdot 2}{g} \qquad M = 1.001 \times 10^{-3}\,H$$

$$L_{tot} := M \cdot \frac{statorpoles}{rotorpoles} \cdot 1.2 \qquad L_{tot} = 1.568 \times 10^{-3}\,H$$

$$L1 := L_{tot} - M \qquad \frac{M}{L1} = 1.769 \qquad L1 = 5.661 \times 10^{-4}\,H$$

$$R_1 := \left[\frac{12 \cdot N^2 \cdot (depth + width) \cdot (statorpoles)}{\sigma_{Cu} \cdot \tau \cdot t \cdot \lambda} + \frac{4 \cdot N}{\sigma_{Cu} \cdot t} \cdot statorpoles \right] \cdot 1.5 + R_{line} \qquad R_1 = 0.025\Omega$$

$$c := .5 \cdot (overhang)$$

$$K_{transverse} := 1 - \frac{\tanh\left(.5 \cdot \frac{\pi}{\tau} \cdot depth\right)}{.5 \cdot \frac{\pi}{\tau} \cdot depth \cdot \left(1 + \tanh\left(.5 \cdot \frac{\pi}{\tau} \cdot depth\right) \cdot \tanh\left(\frac{\pi}{\tau} \cdot c\right)\right)} \qquad K_{transverse} = 0.73$$

$$R_2 := \left[\frac{12 \cdot N^2 \cdot (a_e) \cdot rotorpoles}{\sigma_{Al} \cdot \tau \cdot d \cdot K_{transverse}} + \frac{2 \cdot \frac{\tau}{3} \cdot rotorpoles}{\sigma_{Al} \cdot \frac{overhang}{2} \cdot d \cdot K_{transverse}} \right] \cdot 1 \qquad R_2 = 0.019\Omega$$

$$VHz := B_{start} \qquad VHz = 68\,Wb$$

$$f_{max} := \left(\frac{\pi}{\tau}\right)\cdot\frac{V_{final}}{2\cdot\pi\cdot(1-slip)} \qquad f_{max} = 136.132\,Hz$$

$$\omega_{max} := \left(\frac{\pi}{\tau}\right)\cdot\frac{V_{final}}{(1-slip)} \qquad \omega_{max} = 855.344\,\frac{rad}{s}$$

$$Voltage := VHz\, f_{max} \qquad Voltage = 9.257\times 10^{3}\,V \quad RMS$$

$$Voltage_{perturn} := \frac{Voltage}{N\cdot statorpoles}$$

$$X_1 := \omega_{max}\cdot L1 \qquad L1 = 5.661\times 10^{-4}\,H \qquad Voltage_{perturn} = 102.855V \quad RMS$$

$$X_m := \omega_{max}\cdot M \qquad R_1 = 0.025\Omega \qquad X_1 = 0.484\Omega$$

$$parallel := \frac{X_m\cdot\frac{R_2}{slip}\cdot j}{\frac{R_2}{slip} + X_m\cdot j} \qquad parallel = 0.337 + 0.165i\Omega$$

$$I_{tot} := \frac{Voltage}{\left(R_1 + X_1\cdot j + parallel\right)} \qquad I_{tot} = 6.072\times 10^{3} - 1.088i\times 10^{4}\,A$$

$$I_{totabs} := \left(Re\left(I_{tot}\right)^2 + Im\left(I_{tot}\right)^2\right)^{.5} \qquad I_{totabs} = 1.246\times 10^{4}\,A \quad RMS$$

$$Z_{tot} := R_1 + X_1\cdot j + parallel \qquad Z_{tot} = 0.362 + 0.649i\Omega$$

$$pf := \frac{Re\left(Z_{tot}\right)}{\sqrt{\left(Re\left(Z_{tot}\right)^2 + Im\left(Z_{tot}\right)^2\right)}} \qquad current := I_{totabs}$$

$$pf = 0.487$$

$$I_2 := I_{tot}\cdot\frac{X_m\cdot j}{X_m\cdot j + \frac{R_2}{slip}} \qquad I_2 = 9.192\times 10^{3} - 6.399i\times 10^{3}\,A$$

$$I_{2abs} := \left(Re\left(I_2\right)^2 + Im\left(I_2\right)^2\right)^{.5} \qquad I_{2abs} = 1.12\times 10^{4}\,A \quad RMS$$

$$Force := 3\cdot\left(\frac{\pi}{\tau\cdot\omega_{max}}\right)\cdot I_{2abs}{}^{2}\cdot\frac{R_2}{slip}\cdot.95 \qquad Force = 1.425\times 10^{6}\,N$$

$$Stress := \frac{Force}{2\cdot rotorlength\cdot a_e} \qquad Stress = 1.466\times 10^{5}\,Pa$$

$$Powerloss_{harmonic} := 3 \cdot I_{totabs}^{2} \cdot R_1 \cdot \left(\frac{THD}{100}\right) \qquad Powerloss_{harmonic} = 1.144 \times 10^{6}\,W$$

$$Powerloss_{stator} := 3\, I_{totabs}^{2} \cdot R_1 \qquad Powerloss_{stator} = 1.144 \times 10^{7}\,W$$

$$Powerloss_{rotor} := 3\, I_{2abs}^{2} \cdot R_2 \qquad Powerloss_{rotor} = 7.231 \times 10^{6}\,W$$

$$Powerloss_{transmit} := 3 \cdot I_{totabs}^{2} \cdot R_{line} \qquad Powerloss_{transmit} = 1.592 \times 10^{6}\,W$$

$$Power_{developed} := Force \cdot V_{final} \cdot (1 - slip) \qquad Power_{developed} = 1.359 \times 10^{8}\,W$$

$$Weight_{flywheel} := 4tonne$$

$$Weight_{backiron} := 2 \cdot width \cdot depth \cdot 100m \cdot 7560\frac{kg}{m^3} \qquad Weight_{backiron} = 74.844tonne$$

$$P_{radiated} := Power_{developed} \cdot .1 \qquad P_{radiated} = 1.359 \times 10^{7}\,W$$

$$Efficiency := \frac{Power_{developed}}{Power_{developed} + Powerloss_{stator} + Powerloss_{rotor} + P_{radiated} + Powerloss_{harmonic} + Powerloss_{transmit}}$$

$$Weight_{Cu} := 2 \cdot (2 \cdot width \cdot t \cdot 100m + 2 \cdot depth \cdot t \cdot 100m) \cdot 8900\frac{kg}{m^3} \qquad Efficiency = 0.795$$

$$Weight_{margin} := 20tonne$$

$$Weight_{total} := Weight_{flywheel} + Weight_{backiron} + Weight_{Cu} + Weight_{margin} \qquad Weight_{total} = 138.716tonne$$

$$time_{hotsection} := \left(\frac{rotorlength \cdot 2}{25\frac{m}{s^2}}\right)^{.5} \qquad time_{hotsection} = 0.849s$$

$$Energy_{hotsection} := \frac{2 \cdot (width + depth)}{\left(\frac{\tau}{3}\right) \cdot t \cdot \sigma_{Cu} \cdot \lambda} 3 \cdot I_{totabs}^{2} \cdot time_{hotsection} \qquad Energy_{hotsection} = 1.009 \times 10^{4}\,J$$

$$Cu_{mass} := 8920\frac{kg}{m^3} \cdot 3 \cdot \frac{\tau}{3} \cdot t \cdot \lambda \cdot 2 \cdot (width + depth) \qquad Cu_{mass} = 23.078kg$$

$$\Delta T_{hotsection} := \frac{Energy_{hotsection}}{\left(Cu_{mass} \cdot .385\frac{J}{gm \cdot C}\right)} \qquad \Delta T_{hotsection} = 1.135C$$

$time_{shuttle} := 2s$

$Energy_{shuttle} := 3 \cdot I_{2abs}^{2} \cdot R_2 \cdot time_{shuttle}$ $\quad Energy_{shuttle} = 1.446 \times 10^{7} J$

$mass_{shuttle} := 2700\frac{kg}{m^3} \cdot d \cdot rotorlength \cdot height_{rotor}$ $\quad mass_{shuttle} = 252.72kg$

$\Delta T_{shuttle} := \frac{Energy_{shuttle}}{mass_{shuttle} \cdot .902\frac{J}{gm \cdot C}}$ $\quad \Delta T_{shuttle} = 63.44C$

$K_o := \frac{I_{totabs} \cdot N}{\left(\frac{\tau}{3}\right)}$ $\quad K_o = 2.913 \times 10^{5}\frac{A}{m}$ RMS

$J_{belt} := \frac{K_o}{t}$ $\quad J_{belt} = 1.456 \times 10^{7}\frac{A}{m^2}$ RMS

$B_{airgappeak} := \mu_0 \cdot \frac{K_o}{\frac{g}{2}} \cdot \frac{\tau}{\pi}$ $\quad B_{airgappeak} = 0.997T$

$B_{backironpeak} := B_{airgappeak} \cdot \frac{\frac{\tau}{2}}{width}$ $\quad B_{backironpeak} = 1.744T$

$flux_{rotor} := B_{airgappeak} \cdot \tau \cdot a_e \cdot rotorpoles$ $\quad flux_{rotor} = 4.767Wb$

$distance_{stop} := 3m$

$F_{stop} := \frac{-V_{final}^{2}}{2 \cdot distance_{stop}} \cdot mass_{shuttle}$ $\quad F_{stop} = -4.212 \times 10^{5} N$

$slip_{plot} := .001, .002 .. .999$

$Energy_{shuttle} := \frac{1}{2} \cdot mass_{shuttle} \cdot V_{final}^{2}$

$I_{totplot}(slip_{plot}) := \frac{Voltage}{\left(R_1 + X_1 \cdot j + \frac{X_m \cdot \frac{R_2}{slip_{plot}} \cdot j}{\frac{R_2}{slip_{plot}} + X_m \cdot j}\right)}$ $\quad Energy_{shuttle} = 1.264 \times 10^{6} J$

$I_{totabsplot}(slip_{plot}) := \sqrt{Re(I_{totplot}(slip_{plot}))^2 + Im(I_{totplot}(slip_{plot}))^2}$

$$I_{2plot}(slip_{plot}) := I_{totplot}(slip_{plot}) \cdot \frac{X_m \cdot j}{X_m \cdot j + \frac{R_2}{slip_{plot}}}$$

$$I_{2absplot}(slip_{plot}) := \sqrt{Re(I_{2plot}(slip_{plot}))^2 + Im(I_{2plot}(slip_{plot}))^2}$$

$$V_{synch} := \frac{V_{final}}{1 - slip} \qquad V_{synch} = 104.822 \frac{m}{s}$$

$$F_{plot}(slip_{plot}) := 3 \cdot \left(\frac{\pi}{\tau \cdot \omega_{max}}\right) \cdot I_{2absplot}(slip_{plot})^2 \cdot \frac{R_2}{slip_{plot}}$$

$$speed(slip_{plot}) := V_{synch} \cdot (1 - slip_{plot})$$

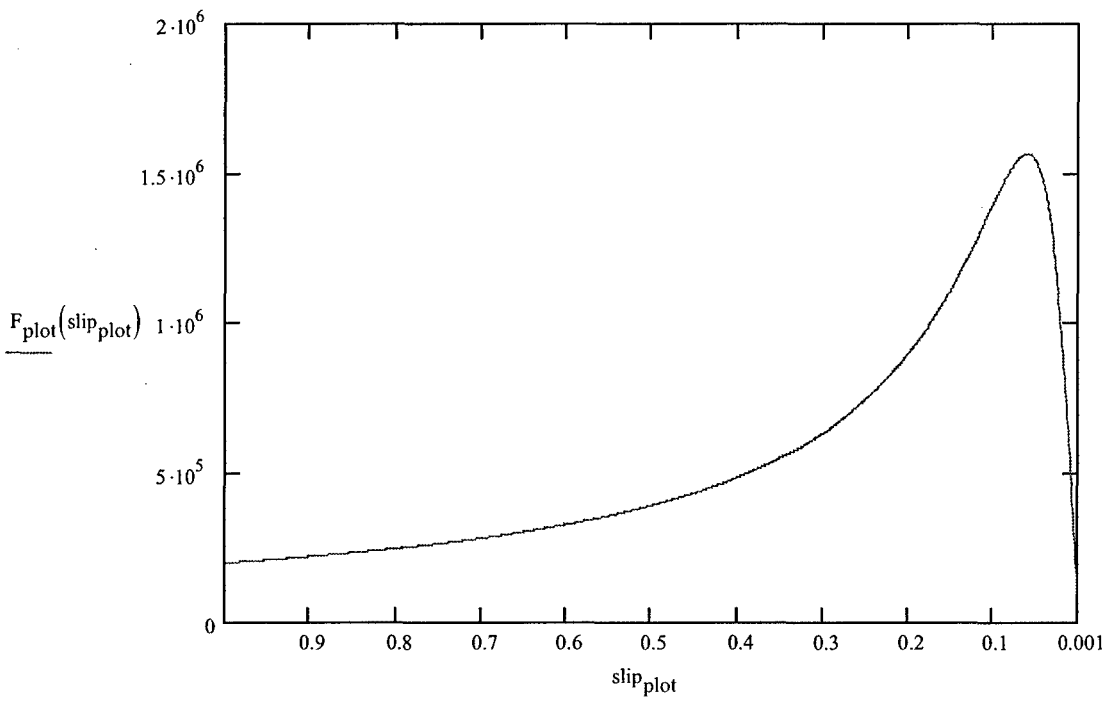

$$K_{oplot}(slip_{plot}) := \frac{I_{totabsplot}(slip_{plot}) \cdot N}{\left(\frac{\tau}{3}\right)} \qquad B_{plot}(slip_{plot}) := \mu_0 \cdot \frac{K_{oplot}(slip_{plot})}{\frac{g}{2}} \cdot \frac{\tau}{\pi}$$

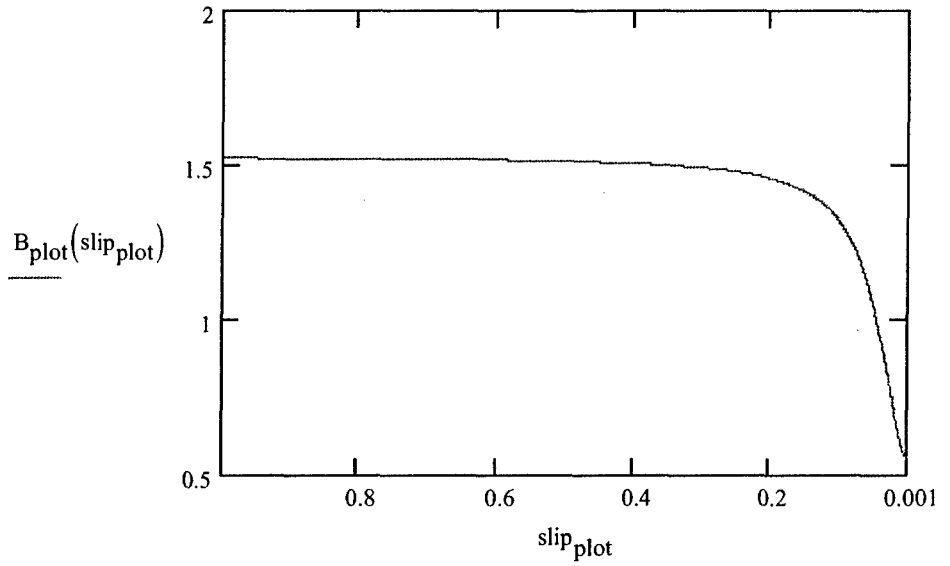

$$Power_{plot}(slip_{plot}) := F_{plot}(slip_{plot}) \cdot speed(slip_{plot})$$

$$Power_{loss1plot}(slip_{plot}) := 3\left(I_{totabsplot}(slip_{plot})\right)^2 \cdot R_1$$

$$Power_{loss2plot}(slip_{plot}) := 3 \cdot I_{2absplot}(slip_{plot})^2 \cdot R_2$$

$$Efficiency_{plot}(slip_{plot}) := \frac{Power_{plot}(slip_{plot})}{Power_{plot}(slip_{plot}) + Power_{loss1plot}(slip_{plot}) + Power_{loss2plot}(slip_{plot})}$$

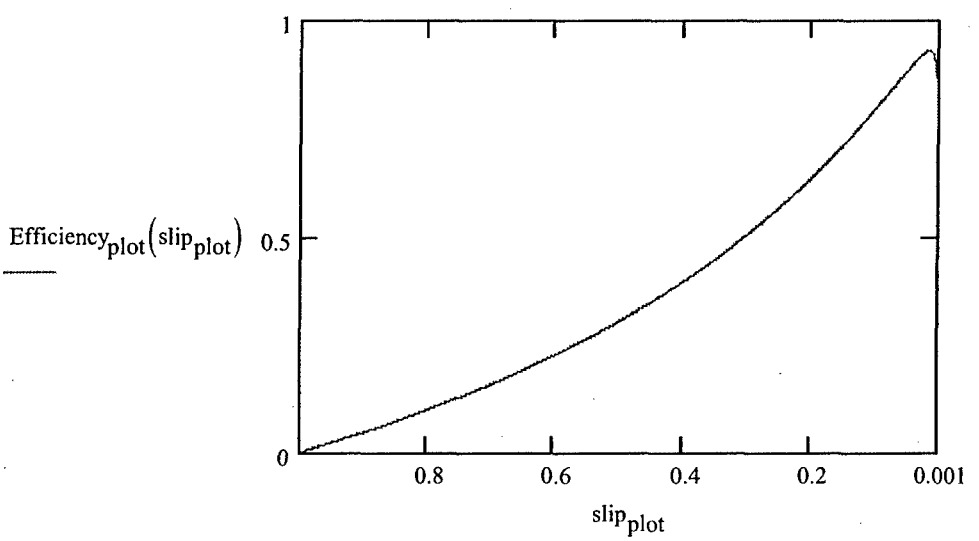

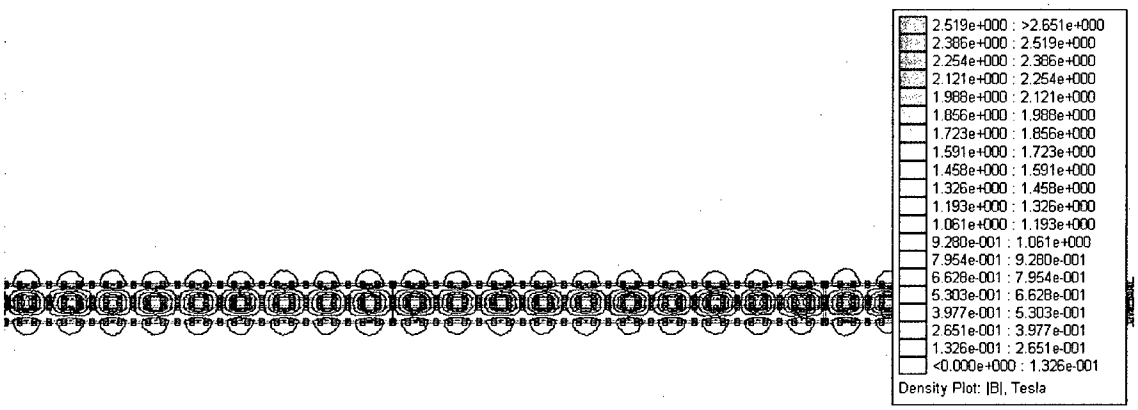

$$\text{Result} := 589450\frac{H \cdot A^2}{m}$$

$$L_{femm} := \frac{\text{Result} \cdot \text{depth}}{(\text{current})^2}$$

$$L_{femm} = 1.708 \times 10^{-3} H$$

$$L_1 := L_{femm} - M$$

$$L_1 = 7.069 \times 10^{-4} H$$

Design Summary

$R_1 = 0.025\Omega$

$R_2 = 0.019\Omega$

$L_1 = 7.069\times 10^{-4}\,H$

$M = 1.001\times 10^{-3}\,H$

$Stress = 1.466\times 10^{5}\,Pa$

$depth = 0.45m$

$width = 0.11m$

$thickness_{rotor} = 0.02m$

$Voltage = 9.257\times 10^{3}\,V$

$current = 1.246\times 10^{4}\,A$

$flux_{rotor} = 4.767Wb$

$Efficiency = 0.795$

$B_{airgappeak} = 0.997T$

$B_{backironpeak} = 1.744T$

$rotorlength = 9m$

$height_{rotor} = 1.04m$

Transient Model for EMALS DSLIM

$L_{stator} := L_1 + M$ $\quad L_{stator} = 1.708 \times 10^{-3} H$

$L_{rotor} := M$ $\quad L_{rotor} = 1.001 \times 10^{-3} H$

$R_s := R_1$ $\quad R_s = 0.025\Omega$

$R_r := R_2$ $\quad R_r = 0.019\Omega$

$flux_{rotor} = 4.767Wb$ $\quad mass := 24000kg$

$\tau = 0.385m$ $\quad acceleration := 53\frac{m}{s^2}$

$C_{drag} := .043$

THIS PAGE INTENTIONALLY BLANK

Appendix H – List of Variables and Acronyms

THIS PAGE INTENTIONALLY BLANK

List of Variables

a = shuttle length
t = shuttle thickness
g = magnetic airgap
L = primary stack height
w = primary stack width
λ = wavelength
k = wavenumber
w = angular frequency (rad/sec)
ω_{slip} = angular slip frequency (rad/sec)
ω_{rotor} = rotor angular frequency (rad/sec)
ω_{stator} = stator electrical frequency (rad/sec)
T_e = Electromagnetic Thrust
f = frequency (Hz)
θ_{rotor} = rotor angular position
V = shuttle velocity (m/s)
V_s = synchronous velocity (m/s)
V_{slip} = slip velocity (m/s)
s = slip
K = linear current density (A/m)
K_o = primary linear current density (A/m)
K_r = shuttle linear current density
B = flux density
B_o = complex amplitude of flux density
E = electric field
μ = permeability
σ_r = surface conductivity
i_{ds} = stator direct axis current
i_{qs} = stator quadrature axis current
i_{dr} = rotor direct axis current
i_{qr} = rotor quadrature axis current
V_d = primary direct axis voltage
V_q = primary quadrature axis voltage

λ_{ds} = stator direct axis flux

λ_{qs} = stator quadrature axis flux

λ_{dr} = rotor direct axis flux

λ_{qr} = rotor quadrature axis flux

I_r = rotor current

I_s = stator current

I_m = magnetizing current

R_s = stator resistance

R_r = rotor resistance

T_r = rotor time constant

L_r = rotor inductance

L_s = stator inductance

L_m = mutual inductance

M = mutual inductance

R_2 = virtual rotor resistance

List of Acronyms

AC	Alternating Current
CVN	Nuclear Fixed-Wing Aircraft Carrier
DC	Direct Current
DSLIM	Double-Sided Linear Induction Motor
EMALS	Electromagnetic Aircraft Launch System
F/A	Fighter Attack
FFT	Fast Fourier Transform
HMS	Her Majesty's Ship
LIM	Linear Induction Motor
LPMM	Linear Permanent Magnet Motor
MMF	Magneto-Motive Force
THD	Total Harmonic Distortion
USS	United States' Ship
WOD	Wind Over Deck